Thermally Activated Charge Fluctuations in GaAs Double Quantum Dots

Inauguraldissertation

zur

Erlangung der Würde eines Doktors der Philosophie

vorgelegt der

Philosophisch-Naturwissenschaftlichen Fakultät

der Universität Basel

von

Daniel Erich Fridolin Biesinger

aus Tübingen, Deutschland

Basel, 2014

Genehmigt von der Philosophisch-Naturwissenschaftlichen Fakultät
auf Antrag von

Prof. Dr. D. M. Zumbühl
Dr. B. Braunecker
Prof. Dr. H. Bluhm

Basel, den 22. April 2014

Prof. Dr. Jörg Schibler
(Dekan)

"The world is full of magical things patiently waiting for our wits to grow sharper."

Bertrand Russell (1872-1970)

Abstract

In this thesis, laterally defined GaAs quantum dots and double quantum dots are investigated by means of real-time charge sensing. A quantum dot charge sensor, adjacent to the investigated double dot system, detects single electron tunneling with sensitivities exceeding that of QPC-based charge sensing systems by far. The experimental setup is characterized in detail and optimized with respect to bandwidth and signal-to-noise ratio. Software tools required for data analysis are developed in combination with a simulation program, capable of creating artificial real-time data for test and characterization purposes.

The experiments described in this work led to the discovery of an intrinsic effect in double quantum dots - thermally activated, meastable charge state switching. A new feature arises in the charge stability diagram of a double quantum dot due to tunneling processes between double dot system and leads. These processes occur in the region between two associated triple points of the charge stability diagram, where originally stable charge configurations are expected. This effect is characterized in detail with respect to coupling to electron reservoirs, as well as inter-dot coupling and temperature dependence. An extension of the orthodox model of double quantum dots is developed, capturing nearly all experimentally observed features. A concrete prediction of this model is the presence of four different charge states that participate in the process of metastable charge state switching. The experimental observation of switching between four different charge configurations is presented and the implications and possible influences of this effect (e.g. loss of coherence) on other experiments are discussed.

Furthermore, this work treats the implementation of spin relaxation time measurements on single electrons, similar to previously performed experiments. This work is motivated by the expected anisotropy of spin relaxation with respect to an external magnetic field. In addition, these experiments are motivated by the previously observed effect of spin-dependent tunneling into a empty quantum dot, where tunneling into the excited spin state is suppressed considerably. These experiments involve gate pulsing techniques, which are required to load and unload electrons from a quantum

dot on a millisecond timescale. The realization of such pulsing sequences is demonstrated in several experiments. The Zeeman splitting of the quantum dot ground state is resolved over a wide range of magnetic fields, which is an important ingredient for spin relaxation time measurements and allows for extracting the electron g-factor in GaAs, as well as investigating the effect of spin-dependent tunneling. Finally, first spin relaxation time measurements are presented, demonstrating the successful execution of this experiments and paving the way for further experiments to study the anisotropy of spin relaxation in GaAs quantum dots.

Contents

Abstract i

1. Introduction 1

2. Physical Background 7
2.1. The Two-Dimensional Electron Gas 7
2.2. Lateral Quantum Dots 10
2.3. Electron Transport Through a Quantum Dot 15
2.4. Quantum Dots in the Presence of Magnetic Fields 20
2.5. Lateral Double Quantum Dots 24

3. Real-Time Measurements 33
3.1. Charge Sensing with QPCs and Quantum Dots 33
3.2. Real-Time Charge Sensing 39
3.3. Bandwidth and Noise 42

4. Investigating Tunneling Processes 49
4.1. Tunneling On and Off a Quantum Dot 50
4.2. Measuring Tunneling Rates 56
4.3. Active Drift Compensation 61
4.4. Tunneling in the Presence of a Magnetic Field 66

5. Thermally Activated Charge Fluctuations 73
5.1. Motivation 74
5.2. Experimental Observations 74
5.3. Device Fabrication 74
5.4. Metastable Region in the Charge-Stability-Diagram 76
5.5. Real-Time Data 77
5.6. Time Resolved Four-Level System in the Metastable Region 78

5.7. Extension of the Orthodox Theory for Transport in DQDs 80
5.8. Summary 82

6. Thermally Activated Charge Fluctuations - Addendum 83
6.1. The Influence of Tunnel Coupling 84
6.2. Visibility at Different Transitions 85
6.3. Temperature Dependence 88
6.4. Bias Dependence 90

7. Spin Relaxation in GaAs quantum dots 95
7.1. Overview and Motivation 95
7.2. Spin Relaxation in GaAs Quantum Dots 98
7.3. Spin Relaxation Time Measurements 101
7.4. Discussion and Outlook 107

8. Summary and Outlook 109

A. Sample Fabrication 113

B. Experimental Methods 119
B.1. Background Subtraction 120
B.2. Charge Sensor - Linear Feedback Mechanism 122
B.3. Lever Arm - and Temperature Determination 124
B.4. Pulsing setup 126
B.5. Device Simulations 128

Bibliography 131

List of Figures 143

Acknowledgments 144

Curriculum Vitae and Publications 146

Chapter 1

Introduction

Modern Solid State Physics is a very vast field of contemporary physical research. It is subdivided in many different branches, such as material science, metal physics, semiconductor physics and the physics of biological matter, to name only a few. It comprises a multitude of phenomena including magnetism, superconductivity, optical- , mechanical- and electrical properties of solids alongside fundamental effects like the Quantum-Hall effect and the Kondo effect [1, 2].

Some of these branches are directly connected to technical and industrial applications with semiconductor physics being the most prominent example. The development of transistors and the architecture of modern integrated circuits is not only a direct consequence of the research done in semiconductor physics but is indeed inspiring new developments itself. The necessity of miniaturizing transistors in order to increase the power of modern computers has directed the focus of interest in semiconductor physics towards small structures and thereby the field of semiconductor nanotstructures emerged [3, 4].

One object, which has drawn a lot of attention in research on semiconductor nanostructures, are quantum dots [4–8]. A quantum dot is a small, isolated accumulation of charge carriers. Those charge carriers can only enter or leave this isolated accumulation through tunneling barriers, which couple the quantum dot to electron reservoirs. The charge carriers are confined to such a small space, that a quantum mechanical treatment becomes inevitable. Therefore quantum dots are a gateway to study fundamental quantum physics.

There is a variety of different ways to realize the concept of a quantum dot, therefore one has to distinguish between different types like vertical quantum dots [9], lateral quantum dots [10], self-assembled quantum dots [11], gate-defined quantum dots on semiconductor heterostructures [4, 10], quantum dots on carbon nanotubes [12] and nanowires [13]. The materials used to fabricate quantum dots vary from compound

semiconductors like Gallium Arsenide and Indium Arsenide over semiconductor heterostructures like AlGaAs/GaAs and Si/SiGe [14] to carbon based systems like carbon nanotubes and graphene [15].

In this thesis the focus lies on lateral, gate-defined quantum dots on AlGaAs/GaAs heterostructures. These AlGaAs/GaAs heterostructures are the subject of research for more than three decades and by now are a well established system for the fabrication of gate-defined quantum dots. The layout of the utilized materials leads to the formation of a special bandstructure at the interface between AlGaAs and GaAs. The result is a so called two-dimensional electron gas, because the electrons no longer can move in the direction perpendicular to the interface - they are confined to a plane [3].

By pattering metallic gate-structures on top of such heterostructures and applying negative voltages to them, it is possible to shape the two-dimensional electron gas beneath the surface almost arbitrarily. As a matter of fact this extraordinary high, fully reversible moldability is the main advantage of gate-defined quantum dots compared to other realization methods, such as self-assembled quantum dots. This method is used in the experiments described here, in order to form quantum dots in the samples with a well-defined and fully tuneable number of electrons residing on them. The subject of these experiments is the investigation of electron tunneling processes from the quantum dots to adjacent electron reservoirs.

The reason for the growing interest in quantum dots during the last couple of years, is the prospect of quantum computation [16]. Quantum dots provide different possibilities to realize a quantum mechanical two-level system. Such a two-level system can serve as a quantum bit (qubit) - the building block of a quantum computer. Qubits can not only be realized with quantum dots in semiconductors. Recent experiments demonstrated the feasibility to realize so called phase qubits in superconducting system [17], qubits based on nitrogen-vacancy centers in diamond [18] and qubits based on photon-states in quantum optics [19]. However, only the qubits based on quantum dots in semiconductors have the advantage of exploiting the same fabrication techniques that are already used in semiconductor industries today. Therefore, the threshold to realize applications on an industrial scale seems to be much smaller than for more exotic systems. On the other side there are other obstacles like the necessity of low temperatures, which can only be obtained by using cryogenic liquids like liquid nitrogen and liquid helium.

But not only practical reasons speak for quantum computing based on semiconductor quantum dots, there are physical reasons as well. The prime example for a two-level system is the quantum mechanical degree of freedom called spin. In systems consisting of e.g. two electrons, the spin will lead to the formation of singlet and triplet states. Such a singlet-triplet system can be realized in double quantum dots and is known

as spin-qubit or singlet-triplet qubit [20–22]. A number of recent experiment on such spin-qubits has lead to considerable progress towards the implementation of quantum computation. Petta *et al.* demonstrated the coherent manipulation of electron spins in double quantum dots [23]. In their experiments they measured dephasing times of up to 10 ns and they identified the hyperfine interaction with the nuclear spins of the host material as limiting factor. The issue of reading out the spin-state of an electron in a quantum dot was addressed by Elzerman *et al.* [24], where the so-called spin-to-charge conversion scheme [16, 25] was implemented, which has become a very important tool for experiments on spin-qubits. Hanson *et al.* addressed the same issue and refined the spin-to-charge conversion scheme by introducing tunnel-rate selective read out [26].

In the subsequent period of time, a lot of effort was put into further investigation of interactions between spin-qubits and environment. The spin dynamics, which is influenced by these interactions, is characterized by two time scales. The first important time scale is the spin relaxation-time T_1, that describes the time scale on which an electron in an excited spin-state relaxes to the ground state. Spin-relaxation times of single electrons were measured in a couple of experiments, performed by Amasha *et al.* [27, 28], Hanson *et al.* [26, 29] and others [30, 31]. According to their experiments spin-orbit interaction, which is mediated via piezoeletric phonons, is the dominant relaxation mechanism. This issue was also addressed theoretically, in particular by Golovach *et al.* [32]. Theory and experiments are in good agreement within the experimental accessible range of magnetic fields. What remains is to measure spin-relaxation times for high magnetic field above 9 T and for small magnetic fields below 1 T, which requires low electron-temperatures. Further, it is of great interest to investigate spin-relaxation as a function of the orientation of an external magnetic field with respect to the crystal axis of the wafer material. Since spin-orbit interaction provides the dominant spin-relaxation mechanism, spin-orbit coupling gives rise to an angle dependent spin-relaxation.

The spin-relaxation of the singlet-triplet system in a double quantum dot was measured by Johnson *et al.* [33, 34]. In their experiments, the observed spin-flips were dominated by hyperfine interaction with the nuclei.

The second characteristic time scale of spin dynamics in solid-state systems is the coherence time T_2, which is the time scale on which the phase information of the investigated electron spin is carried away into the environment. The influence of the nuclear spins was observed in various experiments [33, 35], but the probably most important work was done by Koppens *et al.* [36], demonstrating singlet-triplet mixing by random nuclear fields. In their experiment they measure coherence times of 25 ns[1].

[1]Actually, they measured ensembel coherence times T_2^*, which means they averaged over many different measurements with different electrons instead on performing single-shot measurements on

Subsequent works utilized experimental techniques, which were originally developed for NMR experiments, in order to mitigate the influence of nuclear spins and thereby increasing the coherence times of spin-qubits. Those techniques incorporate multi-step pulsing sequences, also known as dynamical decoupling sequences, because they are used to decouple nuclear spins and electron spins [37, 38]. Bluhm *et al.* [39] showed, that with dynamical decoupling it is possible to achieve coherence times as long as 200 µs in GaAs devices.

After the influence of the nuclear spins has been mitigated, the remaining sources of decoherence have been identified as charge noise [40, 41]. Charge noise leads to fluctuating electric fields at the location of the investigated qubit, which can lead to dephasing as-well. The precise nature of this charge noise is researched in current experiments [42].

Further understanding of the limiting factors of both, the spin-relaxation time T_1 and the coherence time T_2 is required, if any sophisticated attempt to implement computing operations with spin-qubits is to be made.

Almost all of the experiments mentioned above harness charge sensing techniques, as they were developed by Field *et al.* and Ashoori *et al.* [43, 44]. In this technique another system like a quantum point contact [43, 45, 46], or another quantum dot [47] is positioned adjacent to the investigated quantum dot/double quantum dot. Because of a capacitive coupling between both systems, a change in the potential landscape of the investigated system will lead to changes in the sensor system as well. Therefore, the sensor system can be used to probe the investigated quantum dot i.e. the number of charges residing on the dot. Invasive transport measurements through the quantum dot become unnecessary, which is an advantage especially in the regime of low tunnel coupling between quantum dot and leads.

In this thesis quantum dots and double quantum dots are investigated by means of real-time charge sensing. This thesis is organized as follows. In chapter 2 the basic physics of laterally defined quantum dots is discussed. The subsequent chapter 3 treats real-time charge sensing in detail, alongside its technical requirements. In chapter 4 it is explained, how charge sensing is used to investigate tunneling processes of single electrons. Finally, chapter 5 and 6 capture the experimental results. The data there is interpreted as the observation of thermally activated tunneling, which leads to a newly observed feature in the charge stability diagram of a double quantum dot. An extension of the orthodox model of a double quantum dot is presented, which is able to capture most of the observations. Chapter 7 treats the physics of spin-relaxation time measurements and their experimental implementation. Experimental data is pre-

one single electron.

sented, leading towards investigating the angle dependence of spin-relaxation times in GaAs quantum dots.

Chapter 2

Physical Background

This chapter treats the physics of single- and double quantum dots (QD and DQD). Since all experiments presented in this thesis were performed with lateral quantum dots on AlGaAs/GaAs heterostructures, the focus lies on this system. The first section of this chapter covers the heterostructure which was used to fabricate the investigated devices. The subsequent two sections introduce the basic physics of lateral quantum dots. The fourth section examines the effects of an external magnetic field on a quantum dot. Finally, in the last section of this chapter, double quantum dots are discussed. All of these topics are covered in much more detail in the references [3, 4, 8, 20, 48].

2.1. The Two-Dimensional Electron Gas

Some elements in group IV of the periodic table are semiconductors, such as silicon and germanium. They are the basic materials for semiconductor industries. In the adjacent groups of the periodic table, i.e. group III and V, there are elements which are no semiconductors, but together they form binary compounds like gallium arsenide or indium arsenide, so-called compound semiconductors. Another example for a compound semiconductor is the alloy $Al_xGa_{1-x}As$. Here x is the part of aluminum in the compound. This quantity can be used to adjust the band gap, since the resulting band gap can be approximated by *Vegard's law* [3, 49].

$$x \cdot a_{AlAs} + (1 - x) \cdot a_{GaAs} \tag{2.1}$$

In this equation, a is the band gap of the respective material. The lattice constant of the alloy varies only by approximately 0.15% as a function of x. Therefore, it is possible to grow AlGaAs on top of GaAs without inducing strain[1]. Materials, which

[1] This is important, because strain will lead to changes in the band structure and therefore might have negative influence on the properties of the resulting compound semiconductor.

consist of different layers of such compound semiconductors are called heteostructures. The devices used in this work were fabricated on AlGaAs/GaAs heterostructures[2]. The exact layout of the wafer is subject of Figure 2.1. It consists of a 50 nm GaAs

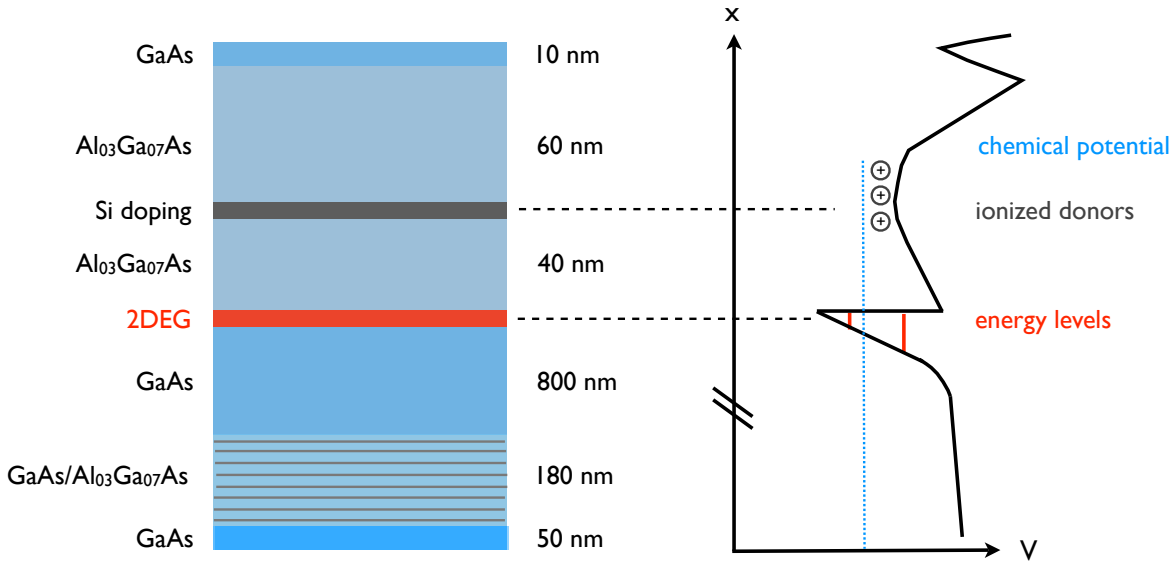

Figure 2.1.: Schematic representation of the AlGaAs/GaAs heterostructure used in the experiments presented here. The right side illustrates the resulting band structure schematically.

bottom layer with a 180 nm GaAs/$Al_{0.3}Ga_{0.7}As$ superlattice on top. The superlattice is followed by a a 800 nm high layer of GaAs and a 100 nm high layer of $Al_{0.3}Ga_{0.7}As$. A silicon δ-doping layer separates the $Al_{0.3}Ga_{0.7}As$ layer into two parts. This δ-doping layer is less than 1 nm high and the doping concentration is $6 \cdot 10^{-12}\,\mathrm{cm}^{-2}$. Finally, on top of the wafer there is a 10 nm high GaAs cap layer.

The right side of Figure 2.1 schematically shows the band structure of such a AlGaAs/GaAs heterostructure. The most relevant part of this band structure is the interface between AlGaAs and GaAs, which is about 110 nm below the surface. Since there is an offset between the band gaps of both materials, electrons can be trapped on the GaAs side of the interface. The electric field of the ionized donors is not able to move the electrons back on the AlGaAs side of the interface. Hence, a triangular quantum well is formed, which is populated by electrons originating from the donor atoms. At temperatures below approximately 100 K only the lowest subband of the triangular well is occupied with electrons [3]. These electrons are no longer able to move in the direction perpendicular to the interface, i.e. they are confined to a plane. Therefore, one speaks of a two-dimensional electron gas (2DEG). The 2DEG of the wafer describe here, has a electron density of $n = 2.6 \cdot 10^{11}\,\mathrm{cm}^{-2}$ and a mobility of

[2]I gratefully would like to acknowledge, that our wafers were grown by Jeramy Zimmermann from A. C. Gossards group at the University of California in Santa Barbara.

$\mu = 4 \cdot 10^5\,\mathrm{cm}^2/\mathrm{Vs}$.

By means of optical- and electron beam lithography, a nanostructure, consisting of titanium/gold gate electrodes, is fabricated on top of the wafer. Applying negative voltages to those gate electrodes leads to the depletion of the 2DEG beneath. Figure 2.2 shows a SEM picture of a device nominally identical to the one used for all the experiments described in this thesis. The layout of the gates is similar to the one used by Barthel *et al.* [47]. Either a single- or a double quantum dot can be formed

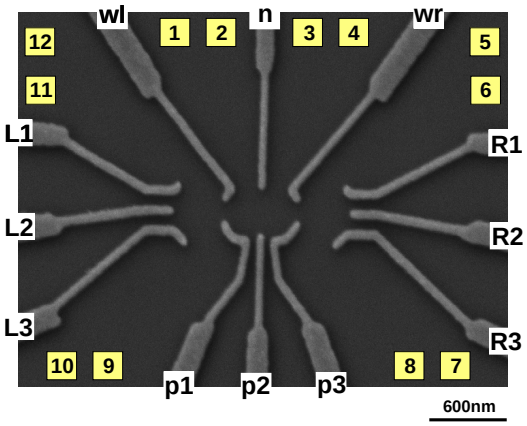

Figure 2.2.: SEM picture of a device, showing the layout of the depletion gates (light gray). The gates p1 through p3, wl, wr and n are used to either form a single or a double quantum dot. L1-L3 and R1-R3 are used to form additional quantum dots, that allow for charge sensing. The yellow labels indicate the positions of ohmic contacts, which are required to contact the 2DEG beneath in order to enable electrical measurements.

in the center of this structure, while three additional gates on each side form sensor quantum dots, suitable for charge sensing. The yellow labels in Figure 2.2 refer to ohmic contacts, required for electrical contacting of the 2DEG. Their layout is chosen such that four-point measurements are possible for the structure in the center as well as for the two charge sensors.

The depletion gates shown in Figure 2.2 introduce an additional confinement, hence locally reducing the 2DEG to a zero-dimensional system, known as quantum dot. In a zero-dimensional system, electrons are no longer able to move in any of the three dimensions of space, and consequently their energy spectrum becomes discrete. This effect is very well known from basic quantum mechanics and resembles the physical situation of electrons orbiting the nucleus of an atom. That is why sometimes a quantum dot is called artificial atom.

Electrons confined to two or less dimensions have different physical properties than electrons, which are free to move in all three directions of space. The physical quantity in which they differ is the density of states [1–3], one of the fundamental quantities in

solid state physics. The density of states (DOS) is defined as the number of accessible states in the energy interval $[\varepsilon, \varepsilon + d\varepsilon]$. The DOS is given by:

$$g(\varepsilon) = g_s g_v \frac{d}{d\varepsilon}\left(\frac{N(\varepsilon)}{V}\right), \tag{2.2}$$

where V is the volume of the solid, $N(\varepsilon)$ the number of states with energy ε and g_s, g_v are multiplicative factors, which take into account the possibility of spin- and valley degeneracy. For gallium arsenide there is no valley degeneracy, therefore $g_v = 1$ but as long as there is no external magnetic field applied, there is spin-degeneracy, hence $g_s = 2$. The DOS can be calculated according to:

$$\begin{aligned} g_{3D} &= \frac{1}{2\pi^2}\left(\frac{2m}{\hbar^2}\right)^{\frac{3}{2}} \cdot \varepsilon^{\frac{1}{2}} \\ g_{2D} &= \frac{m}{\pi\hbar^2}\sum_n \Theta\left(\varepsilon - \varepsilon_n\right) \\ g_{0D} &= 2\sum_n \delta\left(\varepsilon - \varepsilon_n\right), \end{aligned} \tag{2.3}$$

where $\varepsilon = \hbar^2 k^2/2m$ is the dispersion relation of a free particle. From Equation 2.3 one can see, that the DOS of a three-dimensional electron gas scales with the square root of ε, while for a 2DEG it is a constant function. Finally, for a zero-dimensional system the DOS is a sum of delta-functions, representing the discrete energy levels of a quantum dot. Since semiconductor physics does not treat free electrons, but electrons moving in the potential landscape of a solid, the electron mass has to be replaced with the effective mass m^* [1, 2, 4]. The effective mass is a measure for the curvature of the band structure of the respective semiconductor. For example in GaAs $m^* = 0.067 m_e$, which is considerably smaller than the mass of a free electron. Close to the band gap of a semiconductor the band structure can usually be approximated by a parabola, therefore the above dispersion relation of a free particle is still valid if the effective electron mass is taken into account.

2.2. Lateral Quantum Dots

The discrete energy levels of a quantum dot lead to a number of fascinating physical effects. In order to understand these effects, one has to distinguish different regimes in a quantum dot, characterized by the ratio of the relevant energy scales. The most important energy scales of a quantum dot are the confinement energy E_{tot}, the coulomb energy E_C, the coupling to the electron reservoirs and the electron-temperature in those reservoirs.

A quantum dot is coupled to electron reservoirs, which are called source and drain. This coupling is quantum mechanical in the sense that electrons can only enter or leave the quantum dot by means of quantum mechanical tunneling. The coupling to source and drain should be such that the quantization of charge becomes relevant i.e. single electrons can be observed. One can start by considering *Heisenberg's uncertainty relation*

$$\Delta E \cdot \Delta t > h \tag{2.4}$$

and assume a purely classical electrostatic charging energy of $\Delta E = e^2/C_{tot}$, as for a capacitor. One can estimate the time it takes for an electron to tunnel onto the dot by $\Delta t = R_t C_{tot}$, where R_t is the tunneling resistance. In both relations C_{tot} represents the total capacitance of the system, consisting of the capacitance between QD and reservoirs, as well as the capacitance between QD and gate electrodes:

$$C_{tot} = C_s + C_d + C_g \tag{2.5}$$

R_t can then be calculated as follows:

$$R_t > \frac{h}{e^2} \tag{2.6}$$

This equation puts the tunneling resistance in relation to the resistance quantum h/e^2. Only if the tunneling resistance is comparable or larger than the resistance quantum, charge quantization can be observed. All considerations made above are only true if the thermal excitation of electrons is small compared to the charging energy, therefore

$$\frac{e^2}{C_{tot}} \gg k_B T_e \tag{2.7}$$

has to be fulfilled as well. In this context T_e is the electron temperature of the system. Obviously this condition requires either small electron temperatures or a very small capacitance. Since the capacitance depends on the geometry of the QD and in particular on its size, a small capactiance requires a sufficiently small QD[3].

The temperature of the system is also relevant for another energy scale of quantum dots. Only if the thermal energy of the electrons is small compared to the single particle energy spacing Δ, the quantized energy states of a quantum dot can be observed, i.e.

$$k_B T_e < \Delta. \tag{2.8}$$

[3]Assuming a QD in the shape of a disk, the capacitance is given by $C = 8\varepsilon\varepsilon_0 r$ [50]. For $r = 100\,\mathrm{nm}$ the resulting capacitance is approximately $C = 90\,\mathrm{aF}$

The energy level spacing Δ is the manifestation of the confinement energy E_{tot} of the QD. From Equation 2.3 and the definition of the density of states it is clear, that the number of electrons residing on a QD can be written as follows:

$$N = \pi r^2 E_F \frac{m^*}{\pi \hbar^2} \tag{2.9}$$

Here, the Fermi energy E_F is multiplied with the expression for the two-dimensional density of states and the area πr^2 of the QD. The total energy E_{tot} of a QD follows from integrating this expression:

$$E_{tot} = \int_0^{E_F} \pi r^2 E \frac{m^*}{\pi \hbar^2} \, dE = \pi r^2 E_F^2 \frac{m^*}{2\pi \hbar^2} = \frac{\hbar^2}{2m^* r^2} N^2 \tag{2.10}$$

This term defines the total energy of the system for a QD occupied by N electrons. However, this result is only valid for a parabolic dispersion relation, since the latter is used to calculate the DOS. Furthermore, it has to be pointed out, that here the 2D DOS is used to calculate the total energy of a 0D system, while the discrete energy levels of the QD are neglected. If there are already N electrons residing on a QD, adding another electron requires the energy

$$\epsilon(N+1) = E_{tot}(N+1) - E_{tot}(N), \tag{2.11}$$

otherwise the electron will not be able to tunnel on. The separation of successive energy levels can than be calculated from

$$\Delta = \epsilon(N+1) - \epsilon(N), \tag{2.12}$$

which is the aforementioned single-particle energy spacing. Again, this result is based on a 2D DOS and hence gives a good estimate for larger QDs containing many electrons. For few electron dots this relation is insufficient, because it only gives an average level spacing and is not based on a quantum mechanical calculation of the QD spectrum. Another approach, which is better suited for few electron dots, is to model the QD as a quantum mechanical harmonic oscillator. From basic quantum mechanics one knows the oscillator length to be $2r = \sqrt{\hbar/m^*\omega_0}$. Here, ω_0 is the frequency of the harmonic oscillator and the energy spacing is given by $\Delta = \hbar\omega_0$. Combining both expressions gives $\Delta = \hbar^2/(4m^* r^2)$. In general, the confining potential of a quantum dot will not be parabolic, as the potential of a harmonic oscillator. Hence, the single-particle energy spacing Δ is not necessarily constant. However, modeling a QD with a harmonic oscillator is very useful for doing quick calculations and estimates for Δ and other quantities such as the size of the dot. The results of both models are usually in

good agreement.

The preceding considerations do not take into account the electrostatic interaction between different electrons. For electrons in the confinement potential of a QD the electrostatic interaction, or Coulomb energy, can be estimated by assuming a two-dimensional electron gas. Additionally, one can regard the QD as a disk of radius r, with N elementary charges, that is surrounded by a material with a dielectric constant[4] ε. In this case, the capacitance of the system is given by $C_{tot} = 8\varepsilon\varepsilon_0 r$ [50]. The electrostatic energy of such a system is given by

$$E_{el}(N) = \frac{e^2N^2}{2C_{tot}} = \frac{e^2N^2}{16\varepsilon\varepsilon_0 r}, \tag{2.13}$$

and depends on the number N of electrons residing on the QD. Adding another electron to the system, requires the energy

$$E_C(N+1) = E_{el}(N+1) - E_{el}(N) = \frac{e^2}{C_{tot}}\left(N + \frac{1}{2}\right) \approx \frac{e^2N}{8\varepsilon\varepsilon_0 r}. \tag{2.14}$$

The last step of this equation is only true in case $N \gg 1$ and if the QD is still regarded as a capacitor with the shape of a disk. The charging energy of a quantum dot is then defined as follows:

$$\Delta E_C = E_C(N+1) - E_C(N) = \frac{e^2}{C_{tot}} = \frac{e^2}{8\varepsilon\varepsilon_0 r} \tag{2.15}$$

Again, the last step describes the result for a disk-like quantum dot. The charging energy usually is a few meV and is a very characteristic energy scale[5]. All the considerations made in this section are only valid in the framework of the so-called constant interaction model [8]. The constant interaction model is based on two assumptions: First, the interaction of an electron residing on the quantum dot with all electrons (or all other charges) inside and outside the quantum dot can be expressed by a single parameter, the capacitance C_{tot}. This capacitance C_{tot} is identical to the capacitance, that was already introduced above and is assumed to be a constant. Second, the single-particle energy spacing Δ is calculated for non-interacting electrons and it is assumed, that electron-electron interactions do not affect the single-particle energy spacing[6].

In order to compare E_C and Δ, the size of the respective quantum dot has to be

[4] In case of a quantum dot embedded in a GaAs environment, the dielectric constant actually would be $\varepsilon = 13$.

[5] This energy corresponds to a temperature of few K, which is quite a lot, compared to e.g. electron temperatures in the range of 100 mK, as they are obtained in contemporary dilution-refrigerators.

[6] For a known confinement potential of the QD, the single-particle energy spacing can be calculated by solving the *Schrödinger equation*. In the approximation used here, terms representing electron-electron interactions are neglected in the *Schrödinger equation*.

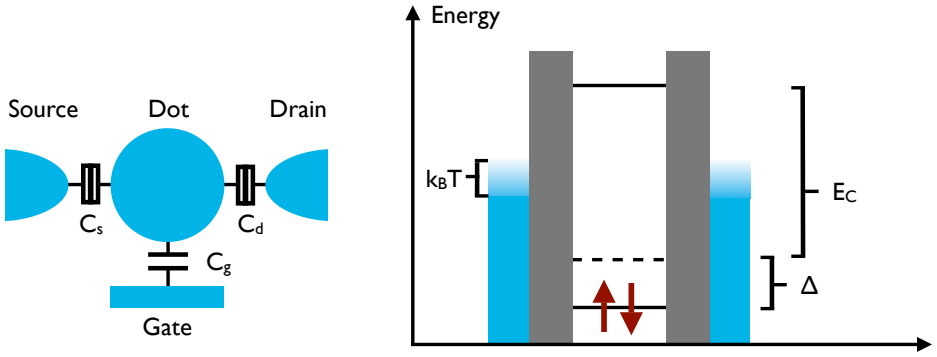

Figure 2.3.: The left hand side of this graphic displays the arrangement of the capacitance between the QD and the surrounding structures. The right hand graphic displays the relation of different energy scales that are relevant for a QD. The depicted situation is the same as discussed in the text, where the charging energy E_C is dominating over the single-particle level spacing Δ and both are larger than the thermal energy k_BT_e.

known. While E_C usually scales with $1/r$ (depending on C_{tot}, i.e geometry of the dot), Δ scales with $1/r^2$ (depending on the model used to calculate the energy spectrum, e.g. oscillator model). Since a precises estimate for the dot size is difficult to obtain (see e.g. Brandes *et al.* [51]), it is hard to make a reliable analysis, especially since the dot size of laterally defined QDs changes as a function of gate voltage. However, it is possible to make a general statement. For laterally defined quantum dots, as they are investigated in this thesis, the charging energy will dominate over the single-particle energy spacing. For example in self-assembled quantum dots in InAs the situation is different, here the single-particle energy spacing will dominate over the charging energy. This is due to the differences in effective mass and dielectric constant between both materials.

After treating the different quantities and energy scales, which are relevant for a quantum dot, one can make the following conclusion: For quantum dots, which are fabricated by laterally confining a two-dimensional electron gas in AlGaAs/GaAs heterostructure, the regime of interest is defined by:

$$k_BT_e < \Delta,\ k_BT_e < \Delta E_C \text{ and } R_t > \frac{h}{e^2} \tag{2.16}$$

Only if these conditions are fulfilled, the quantization of charge and the discrete energy spectrum of a quantum dot will be observable. Additionally, one has to distinguish two different regimes, which are known as tunneling broadened- and thermally broadened regime. Tunneling process can be quantified by the tunneling rate Γ, which can be transformed into an equivalent energy through multiplication with $\hbar$. If $\hbar\Gamma \gg k_BT_e$, the dot is in the tunneling broadened regime, while for $\hbar\Gamma \ll k_BT_e$ the QD is in the

thermally broadened regime. The quantum dots/double quantum dots investigated in this thesis are operated in the thermally broadened regime, with rather small tunneling rates in the range of a few Hz up to 10 kHz. The adjacent sensor quantum dots can be operated in both regimes. Further explanations of this topic require the discussion of transport experiments on quantum dots, which will be treated in the succeeding section.

2.3. Electron Transport Through a Quantum Dot

In the preceding section the different relevant energy scales of a quantum dot were discussed. Adding another electron to a QD requires the addition energy E_{add}, which consists of the charging energy E_C and the single-particle level spacing Δ and is a function of the number of electrons already residing on the dot. In such a system with variable energy and number of particles N, one can define a chemical potential $\mu(N)$, which quantifies the energy required to add another electron to the system [8, 10]:

$$E_{add} = E_C + \Delta = \frac{e^2}{C_{tot}} + \Delta = \mu(N+1) - \mu(N) \tag{2.17}$$

Since every orbital state can be occupied with two electrons, the energy Δ only is required in case all lower lying orbitals already are full. The energy levels in a QD, or respectively the chemical potential, can be shifted by applying a negative voltage to a capacitively coupled nearby gate electrode (see Figure 2.3). Thereby it is possible to control the number of electrons on the dot precisely. For sufficiently negative gate voltage, the quantum dot can be emptied completely. By continuously increasing the applied gate voltage, the different states of the quantum dot will be successively filled with electrons.

Probing a quantum dot by means of transport measurements reveals information about the addition energy of the system. For such transport measurements, a small AC source-drain voltage V_{SD} is applied across the quantum dot. This excitation is usually in the order of a few µV (in order to prevent heating effects) and allows to measure the differential conductance dI/dV_{sd} of the system, with standard lock-in techniques (see Figure 2.4). The lock-in amplifier, which provides the AC signal on the source side, is used to probe the response of the system on the drain side. The amplitude of the applied AC signal, together with the amplitude of the measured oscillating current, allows to determine the differential conductance. All measurements of the differential conductance shown in this thesis are expressed in units of the conductance quantum $e^2/h \approx (25813\,\Omega)^{-1}$. In the following, the term conductance is use as a synonym for differential conductance unless explicitly stated different.

If the gate voltage V_g of the QD is varied, the measured conductance shows a series of pronounced peaks. These peaks are known as Coulomb peaks (CB peak) and are the manifestation of the Coulomb blockade effect. As a function of gate voltage, the energy levels in the QD are shifted. Whenever an unoccupied state is aligned with the chemical potential in the source, electrons can tunnel resonantly between QD and source. If no additional DC-bias is applied, the chemical potential in the source- and drain reservoirs are the same. Therefore, an electron which tunnels in from the source

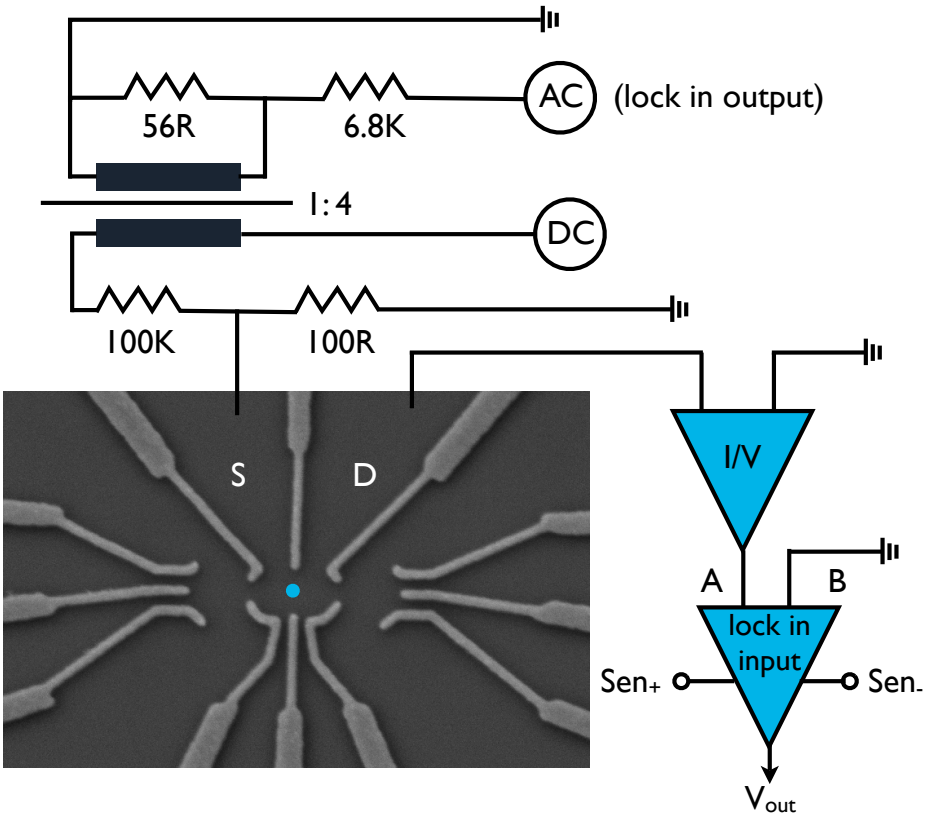

Figure 2.4.: This graphic depicts the standard setup for transport measurements on a QD. An AC source-drain bias V_{SD} is applied across the QD. The exciting AC signal is applied on the source electrode, while the drain electrode is grounded through the I-V converter to measure the resulting current. This setup additionally provides the possibility to add a DC signal to the AC excitation by inductively coupling both components.

can tunnel off to the drain electrode, which is equivalent to electron transport through the QD. In this case the measured conductance will show a Coulomb peak. The applied gate voltage also can lead to a configuration, where all occupied energy levels are below the chemical potential in the reservoirs, while the next unoccupied energy levels lies higher in energy than the chemical potential. Now electron transport through the QD is not possible, the system is in Coulomb blockade. Both situations are depicted in Figure 2.5, while measured data is shown in Figure 2.6. The distance between succeeding Coulomb peaks contains information about the addition energy E_{add}, while

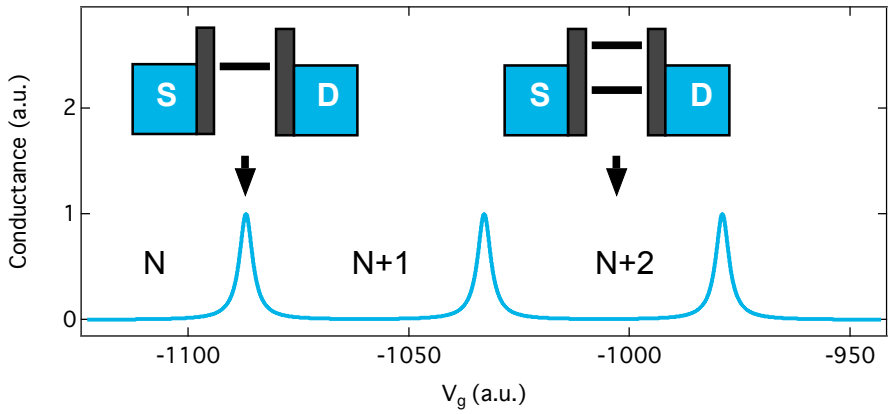

Figure 2.5.: Schematic illustration of the Coulomb blockade effect. The blue line shows the conductance as a function of gate voltage V_g. When an unoccupied energy level in the dot is aligned with the chemical potential in the leads, electron transport through the QD is allowed (left hand inset). In this case the measurement shows a distinct Coulomb peak. If the lowest unoccupied energy level is not accessible for the electrons in the source, the system is blocked and electron transport is not possible (right hand inset). This configuration is called Coulomb blockade.

the line shape depends on the ratio of thermal energy $k_B T_e$ and the tunnel coupling to source and drain, $\hbar\Gamma_{S,D}$. In the regime $\hbar\Gamma_{S,D} \gg k_B T_e$ the width of Coulomb peaks is dominated by lifetime broadening [52–54]:

$$G = \frac{2e^2}{h}\frac{\Gamma_S\Gamma_D}{\Gamma_S+\Gamma_D}\left(\frac{\Gamma_t}{\left(\frac{\Gamma_t}{2}\right)^2+\left(\frac{e\alpha_g}{\hbar}\Delta V_g\right)^2}\right);\ \Gamma_t = \Gamma_S+\Gamma_D \tag{2.18}$$

This is a Lorentzian, where Γ_S and Γ_D are the tunneling rates to source and drain and α_g is the lever arm, defined as the ratio C_g/C_{tot}, where C_g is the gate capacitance and C_{tot} the total capacitance of the QD. The lever arm α_g is a conversion factor, which is required to convert between gate voltage and energy, $\Delta E = -e\alpha_g \Delta V_G$. Reducing tunneling to source and drain, i.e. for smaller $\Gamma_{S,D}$, an intermediate regime is entered. Here, lifetime broadening and thermal broadening both contribute to the peak width. Further reducing the tunneling rates will bring the system into the thermally broadened regime, characterized by the condition $k_B T_e \gg \Gamma_{S,D}$. In the thermally broadened regime, the line width is given by

$$G = \frac{2e^2}{h}\frac{\Gamma_S\Gamma_D}{\Gamma_S+\Gamma_D}\frac{h}{4k_B T_e}cosh^{-2}\left(\frac{e\alpha_g\Delta V_g}{2k_B T_e}\right). \tag{2.19}$$

The above equation is proportional to the derivative of a Fermi function [53]. In this regime the width of CB peaks only depends on the electron temperature in the source- and drain electrodes.

Knowing the conversion factor between gate voltage and energy is essential, if any

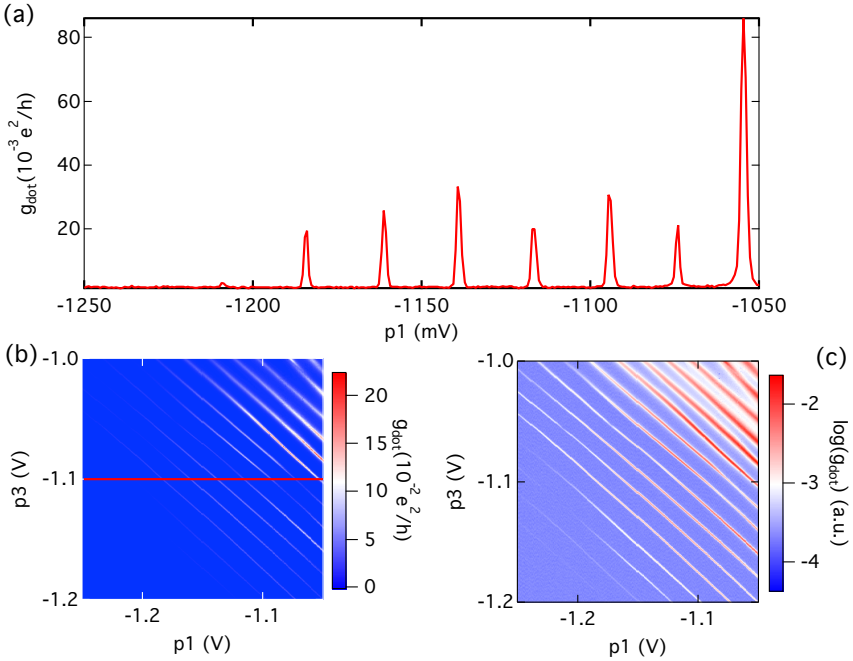

Figure 2.6.: (a) Coulomb peaks measured as a function of gate voltage p_1 (see Figure 2.2). This trace corresponds to a cut trough of graphic (b) at the red line. (b) Wall-Wall scan of a device similar to the one shown in Figure 2.2. Here the conductance is measured as a function of p_1 and p_3, revealing diagonal lines which correspond to Coulomb peaks. (c) Same data set as in (b) but plotted on a logarithmic scale.

conclusion about the energy spectrum of a quantum dot is to be drawn. Therefore, determining the lever arm α_g as precisely as possible if of great importance. Usually, α_g is extracted by measuring Coulomb diamonds, which can be observed in the conductance as a function of gate voltage and DC bias. Adding a DC component to the bias will shift the chemical potential of the source electrode with respect to the chemical potential on the drain side[7]. The difference in energy between the chemical potentials μ_S on the source side and μ_D on the drain side is equivalent to the formation of a so-called bias window. As a result, electron transport through the quantum dot is possible whenever an energy level lies within the bias window. Varying the voltage applied to the gate which is used to control the quantum dot, will shift the energy levels in the dot and drive them through the bias window. As a function of the applied DC bias, the Coulomb peaks in conductance will open into areas where electron transport is allowed. Simultaneously, the areas of Coulomb blockade shrink as function of DC bias, because of the growing bias window. This situation is illustrated in Figure 2.7. The upper panel of this graph also illustrates how to extract the lever arm α_g from such a measurement. For a given bias V_{SD}, there is a finite gate voltage rage $|\Delta V_g|$,

[7]Since the drain electrode is connectd to a I-V converter in the measurement described here, it lies on ground and therefore remains unaffected by the DC bias.

where electron transport is allowed. Both quantities, V_{SD} and $|\Delta V_g|$, are connected via a constant of proportionality, which is the inverse of the lever arm, i.e

$$|\Delta V_g| = \frac{V_{SD}}{\alpha_g}. \tag{2.20}$$

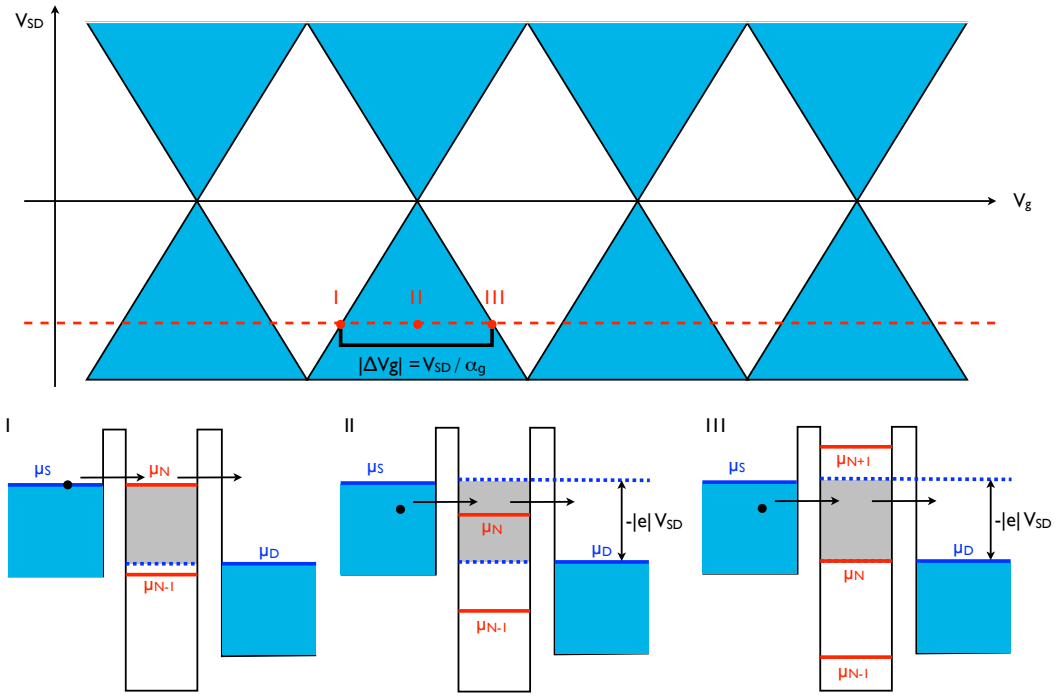

Figure 2.7.: Upper panel: Illustration of Coulomb diamonds, where the blue areas represent a non-zero differential conductance. Additionally, the black bar indicates the relation between source-drain bias and gate voltage, which can be used to extract the lever arm of the corresponding gate. Lower panel: Representation of the situations I, II and III in the upper panel. In I the level labeled μ_N enters the bias window $-|e|V_{SD}$ and electron transport through this level becomes possible. By continuously increasing the gate voltage V_g, this level will be driven through the bias window (II) and finally will leave it again (III). Now there are no further accessible levels in the bias window, therefore the system is in Coulomb blockade.

Consequently, the lever arm α_g can be read directly from a Coulomb diamond measurement. However, the lever arm extracted in this way is only valid for the individual gate, used for this specific measurement. For devices consisting of multiple gates, as they are discussed in this thesis, every single gate as a lever arm of its own. Therefore, one has to determine the lever arm for every gate separately, or at least for those gates used in further experiments. Additionally, the lever arm of a single gate depends on the configuration of the adjacent gates, i.e the voltage applied to those gates. Consequently, different configurations of gate voltages can lead to different lever arms for the very same gate.

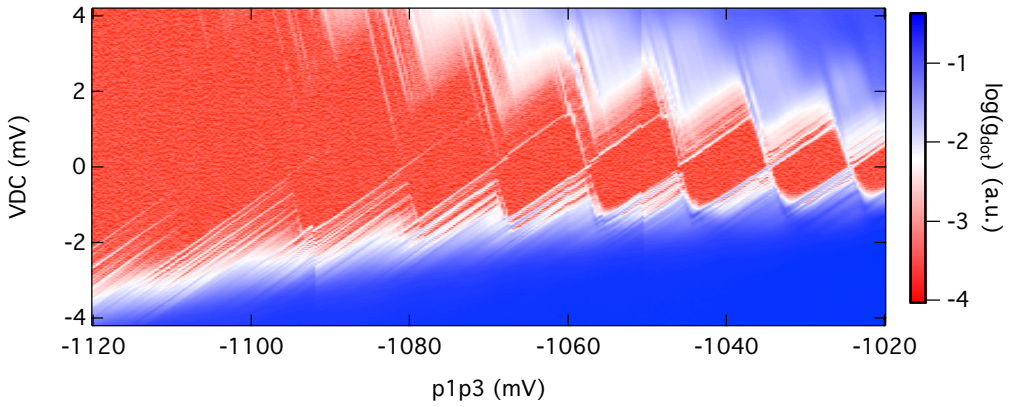

Figure 2.8.: Measured Coulomb diamond as a function of source-drain bias V_{SD} and gate voltage p1 (see Figure 2.2). The data in this graph is displayed on a logarithmic scale, where the blue shaded areas indicate the regions where electron transport through the dot is possible. The red shaded areas represent the actual Coulomb diamonds, i.e. where the system is in blockade.

Figure 2.8 shows measured data of Coulomb diamonds. In Addition, one can distinguish additional lines, that run parallel to the borders of the Coulomb diamonds but lie outside the borders. Those additional lines can be excited states of the quantum dot. Whenever an excited state enters the bias window, while the ground state still lies within the bias window as-well, both states contribute to electron transport. As as consequence, the differential conductance increases whenever an excited state enters the bias window. Therefore, Coulomb diamond measurements also are a tool to do excited state spectroscopy. It is even possible to extract the single particle energy spacing Δ (see Equation 2.12) and thereby gain additional insight into the energy spectrum of the respective quantum dot [4].

2.4. Quantum Dots in the Presence of Magnetic Fields

Applying an external magnetic field to a quantum dot system has considerable influence on the QD energy spectrum and can induce a multitude of different effects. Furthermore, the electron spin can no longer be neglected. Due to the complexity of this topic, the focus of this section lies on the two configurations, which are of importance for this work. In the first configuration, the homogeneous external magnetic field B is applied perpendicular to the 2DEG. If there are multiple electrons on the QD, an external, perpendicular magnetic field B leads to exchange interactions between the different electron-spins [55–58]. The most prominent manifestation of these exchange effects, is the resulting spatial distribution of different spin states, i.e. shell filling effects as they are known from atomic physics [8, 55, 58].

But not only the QD itself is influenced by the perpendicular magnetic field. The

electrons in the leads are also subject to quantization effects, the so-called Landau quantization. The formation of Landau levels in the leads effects electron transport through the QD [59]. In addition to the aforementioned influences, perpendicular magnetic fields will also effect the confinement potential of the system. The confinement will be increased, i.e. the size of the quantum dot will decrease and therefore its energy spectrum differs from the zero field configuration.

The effects caused by the exchange interaction, the Landau quantization and the change of the confinement potential are unfavorable for those experiments discussed in this thesis, which investigate spin effects. Consequently, the magnetic field is applied parallel to the 2DEG in the sample. The parallel B-field configuration is the second case, that will be discussed in this section. A magnetic field parallel to the 2DEG will couple to the spin of the electrons in the quantum dot, just like the perpendicular field component does. Now, orbital effects are small and the interaction between magnetic field and spin can be described by adding a Zeeman term to the Hamiltonian of the system, which is given by

$$\mathbf{H}_Z = \frac{g\mu_B}{\hbar}\ \vec{S}\cdot\vec{B}. \tag{2.21}$$

In this equation $\mathbf{B}$ represents the external magnetic field and $\mathbf{S} = \frac{\hbar}{2}\boldsymbol{\sigma}$ the spin operator with the Pauli matrices $\boldsymbol{\sigma}$. Further, $\mu_B = \frac{e\hbar}{2m_e}$ is the Bohr magneton, which is approximately $5.8 \cdot 10^{-5}\,\mathrm{eV\ T^{-1}}$ and g represents the g-factor, which is given by $g = -0.44$ for electrons in bulk GaAs [60]. The difference between the g-factor of a free electron an electrons in the conduction band of GaAs is due to the effects of band structure, which in case of GaAs is also influenced by the spin-orbit interaction [61]. The effect of this Zeeman term on the energy spectrum of a quantum dot, is to lift spin degeneracy and induce an energy gap of $E_Z = |g|\mu_B B$ between spin-up and spin-down states. This energy gap between the different spin states is referred to as Zeeman splitting. Because of the negative g-factor in GaAs, the excited state is the spin-down state and the spin-up state is the ground state, while for free electrons the spin-down state is the ground state. The reason for this, is that for free electrons the magnetic moment $\vec{\mu}_e$ points in the opposite direction of the spin [62]. The negative g-factor for electrons in GaAs reverses this situation, now spin and magnetic moment point in the same direction.

There are different ways to observe the Zeeman splitting in experiments on quantum dots. The presence of an excited spin-state can be observed e.g. in transport measurements, as they where discussed in the previous section. Measuring the differential conductance dI/dV_{SD} will reveal additional resonances [54], which are not observed in the absence of an external magnetic field. However, this method has a number of disadvantages. First, it requires the knowledge of the lever arm α_g in order to be able to convert gate voltage into energy. Any uncertainty in α_g will lead to uncertainties

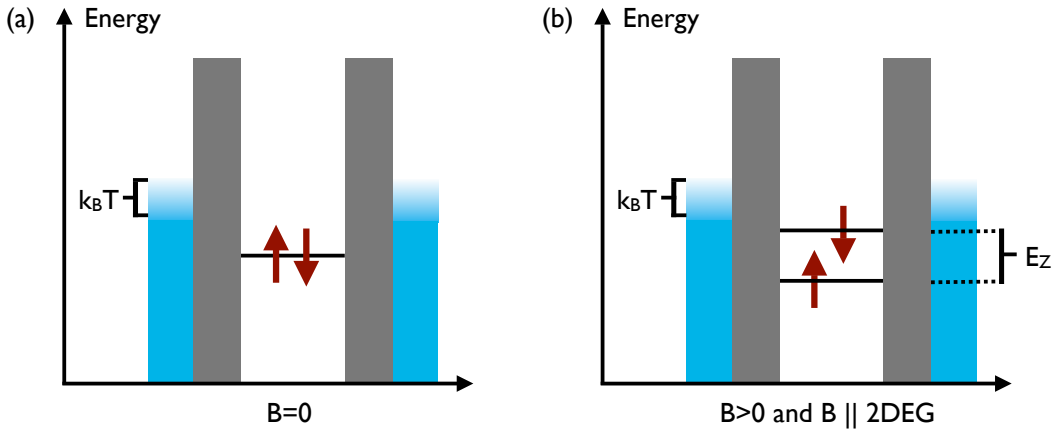

Figure 2.9.: (a) Generic situation of a quantum dot without external magnetic field. Both spin states are degenerate. (b) Applying an external magnetic field B parallel to the 2DEG, will induce a Zeeman splitting $E_Z = |g|\mu_B B$ between spin-up and spin-down states.

in determining the Zeeman splitting as well. Second, charge fluctuations in the wafer material will shift the energy levels in the QD as a function of time because of the electrostatic coupling between them [63]. Therefore, the positions of the observed resonances fluctuates and introduce an additional uncertainty.

Another method to observe the Zeeman splitting of the energy levels in a quantum dot is inelastic spin-flip cotunneling spectroscopy [64]. Consider a QD in the multi-electron regime, with N electrons in the system. If N is an odd number, the QD will have a net spin. Additionally, if the system is in Coulomb blockade, the N+1-electron cannot tunnel onto the dot, therefore electron transport through the system is blocked. But due to the *Uncertainty Principle*, there is still the possibility of virtual tunneling processes. An electron can virtually tunnel onto the QD on the timescale $\hbar/E_{add}$, if afterwards another electron tunnels of the QD, such that energy is conserved. This so-called cotunneling process is elastic if the condition $|eV_{SD}| < E_Z$ is fulfilled, otherwise the process also can be inelastic and consequently the dot can end up in the excited spin-state after such a cotunneling process has occurred [65, 66]. The measured differential conductance as a function of V_{SD} increases in the regime where cotunneling processes are possible. Therefore, one can observe a characteristic cotunneling gap and from the line shape of this gap, it is possible to extract the Zeeman splitting [54, 64].

Finally, one can observe the Zeeman splitting by determining the tunneling rates onto an empty quantum dot[8]. For this method it is essential, that one can ionize the QD completely, i.e. there are no electrons remaining on it. This condition can only be fulfilled if the investigated QD is small enough such that reasonably small gate voltages

[8]Actually, the same procedure can be used to determine the Zeeman splitting for higher electron numbers, but here the focus lies on the last electron due to the intended spin-relaxation time measurements.

are sufficient to empty the QD. In this context reasonable small gate voltage means that the device is not damaged by those gate voltages and if necessary, transport measurements are still practicable. These kind of measurements are based on a two-step pulsing scheme, consisting of voltage pulses, which are applied to one of the gates that is used to control the number of electrons in the QD. At first, the system is completely ionized, there are no electrons left on the QD. Afterwards a voltage pulse shifts the energy levels in the QD such that e.g. the ground state lies below the chemical potential in the leads and an electron can tunnel onto the system (see. Figure 2.10). By varying

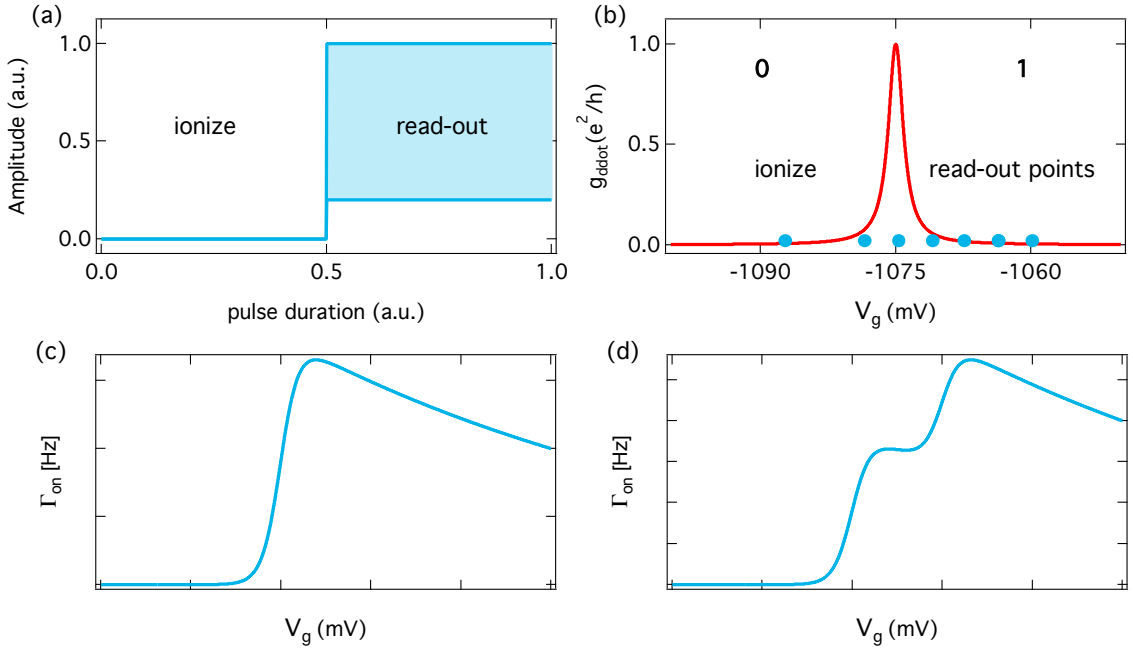

Figure 2.10.: (a) Two-step pulsing scheme, as described in the text. The amplitude of the second step is lowered successively (blue shaded area). (b) The applied pulse drives the system across the 0 - 1 transition of the QD. By decreasing the pulse amplitude, it is possible to scan over the resonance (blue dots) and detect the resulting tunneling processes. (c) In absence of magnetic fields, the tunneling rate Γ_{on} onto the quantum dot follows a Fermi function. (d) An external magnetic field splits the Fermi step into two steps, corresponding to the two spin-states, that are no longer degenerate. Both graphs, (c) and (d), show theoretical predictions that take into account the energy dependence of the tunneling barrier, giving rise to an exponential decay of the Fermi function.

the pulse height, it is possible to scan over the lowest lying resonances and to extract the tunneling rate onto the QD. For practical reasons, those tunneling processes have to be fast, i.e. in the order of a few 100 Hz − 10 kHz, and therefore require real-time measurement electronics. Otherwise, taking large amounts of data, which is necessary in order to have sufficient statistics for the evaluation, takes very long amounts of time. In absence of magnetic fields, and in case the pulse height is tuned such that the measurement only scans across the ground state of the QD, the resulting tunneling rate

Γ_{on} is given by a Fermi function. In presence of a magnetic field, the ground state will be Zeeman split into the different spin-levels and consequently the resulting Γ_{on} shows two Fermi steps, separated by the Zeeman energy E_Z (Figure 2.10 c) and d)). Since the width of the Fermi function is given by the thermal energy $k_B T_e$, this method only is practicable if the Zeeman energy is significantly larger than the thermal energy, $E_Z \gg k_B T_e$.

In this thesis, the last of the three methods is used to extract the Zeeman splitting. All experiments presented here were performed in the few-electron regime. In combination with small tunneling rates, transport measurements are often not possible, due to the resulting small currents. Instead, real-time charge sensing was used to read out charge configurations and detect tunneling events (see. chapter 3). Besides, real-time detection of tunneling is a necessary step towards experiments that aim at investigating single-electrons properties, such as the single-electron relaxation time T_1. Therefore, determining the tunneling rate onto a QD is a very important experiment in this thesis an will be discussed in more detail in chapter 4.

2.5. Lateral Double Quantum Dots

There is the possibility to coupled individual quantum dots to different kinds of arrays. In order to do this, one has do make the spatial separation between the individual quantum dots very small. The most common and most investigated type of array is the so-called double quantum dot (DQD), which consist of two quantum dots [48]. In this work, the focus lies on serial double quantum dots, which means that electron transport is only possible by sequentially passing through both QDs. Additionally, the number of electron residing on each dot is assumed to be controlled separately by different gate electrodes. Further one has to distinguish two different types of coupling between the two QDs. The electrostatic interaction between both subsystems leads to an electrostatic coupling, which changes the energy spectrum of the quantum dots. If the QDs are close enough, an additional tunneling coupling is introduced. This second kind of interaction changes the energy spectrum of the system as well by inducing anti-crossings between different energy levels, that would otherwise be degenerate at one point.

In order to obtain further insight into the physics of double quantum dots, one models the system as is shown in Figure 2.11. Here, the individual quantum dots are connected with each other an with the source- and drain electrode via tunneling contacts. The symbol used to represent such a tunneling coupling in Figure 2.11, has to be interpreted as a parallel connection of a capacitor and a resistor. Each dot is additionally capacitively coupled to a gate-electrode or plunger gate. This model can be used to obtain

a purely classical description of a DQD, which only includes electrostatic interactions, while discrete energy states in the QDs and the influence of quantum mechanical tunneling are neglected for now. The number of electrons residing on each individual QD is expressed by $N_i, i = 1, 2$. $V_{gi},\ i = 1, 2$ is the gate voltage applied to gate i and the capacitive coupling between dot i and gate i is described by the capacitance C_{gi}. The

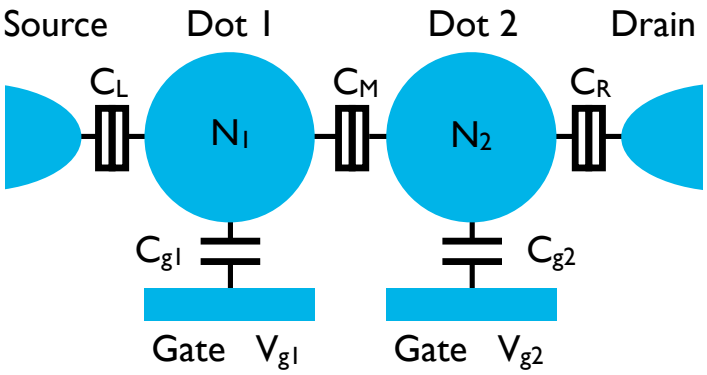

Figure 2.11.: Schematic representation of a serial double quantum dot, where the individual dots are connected with each other and with source and drain via tunneling couplings. Each dot is capacitively coupled to gate electrode/plunger gate, which can be used to control the number $N_i,\ i = 1, 2$ of electrons on each dot individually. In this model, a DQD is a network of classical resistors and capacitors, which is controlled by the gate voltages $V_{gi},\ i = 1, 2$ and the source-drain bias V_{SD}.

coupling between the quantum dots is expressed by the capacitance C_m, while coupling to source and drain is expressed by C_L and C_R. Additionally, this model incorporates a source-drain bias V_{SD}, which is applied to the source electrode while the drain electrode is left grounded. This configurations is called asymmetric bias and represents the common experimental realization of transport measurements through such a system. One further assumes that other voltages and cross capacitances between different parts of the DQD system can be neglected, which, of course, is an idealization. In this case, and under all the aforementioned assumptions and idealizations, the electrostatic energy of a double quantum dot can be written as [48]:

$$U(N_1, N_2) = \frac{1}{2}E_{C1}N_1^2 + \frac{1}{2}E_{C2}N_2^2 + N_1N_2E_{Cm} + f(V_{g1}, V_{g2}) \tag{2.22}$$

In this equation, E_{Ci} are the charging energies of the individual dots and E_{Cm} is the electrostatic coupling energy. Those quantities can be expressed as follows:

$$E_{C1} = \frac{e^2}{C_1}\left(\frac{1}{1-\frac{C_m^2}{C_1C_2}}\right), \quad E_{C1} = \frac{e^2}{C_2}\left(\frac{1}{1-\frac{C_m^2}{C_1C_2}}\right), \quad E_{Cm} = \frac{e^2}{C_m}\left(\frac{1}{\frac{C_1C_2}{C_m^2}-1}\right) \tag{2.23}$$

The function $f(V_{g1}, V_{g2})$ is a complicated expression describing the influence of the gate voltages V_{gi}. A full derivation of theses equations can be found in [48] and [4]. A more thorough treatment of the capacitance model, which is the foundation of this derivation, can be found in [4, 67]. The capacitances C_i from Equation 2.23 refer to the sum of all capacitances attached to the respective quantum dot, given by:

$$C_1 = C_L + C_{g1} + C_m, \quad C_2 = C_R + C_{g2} + C_m \tag{2.24}$$

The influence of other capacitances, e.g. additional gates, is neglected. In case of negligible mutual electrostatic coupling between the QDs ($C_m = 0$) Equation 2.22 further reduces to

$$U(N_1, N_2) = \frac{(-N_1|e| + C_{g1}V_{g1})^2}{2C_1} + \frac{(-N_2|e| + C_{g2}V_{g2})^2}{2C_2}. \tag{2.25}$$

Consequently, for vanishing electrostatic inter-dot coupling, the energy of the DQD system is the sum of the energies of the two separate dots. Another limiting case of a DQD system is characterized by $C_m/C_i \to 1$, which means that the electrostatic coupling between the dots becomes dominant. In this case the electrostatic energy of the system can be calculated as follows:

$$U(N_1, N_2) = \frac{\left(-(N_1 + N_2)|e| + C_{g1}V_{g1} + C_{g2}V_{g2}\right)^2}{2(C_1^* + C_2^*)}, \quad C_i^* = C_i - C_m \tag{2.26}$$

This result can be interpreted as the energy of a single dot with charge $N_1 + N_2$, which implies that the double dot can be treated as one large, single quantum dot.

Analogue to the treatment of a single quantum dot, one can now define an electrochemical potential μ, quantifying the energy needed to add an additional electron to the system. However, for the double dot system, the electrochemical potential of the left dot will in general differ from the one of the right dot. Therefore, one has to introduce two electrochemical potentials μ_1 and μ_2:

$$\mu_1(N_1, N_2) = U(N_1, N_2) - U(N_1 - 1, N_2) \tag{2.27}$$

$$\mu_2(N_1, N_2) = U(N_1, N_2) - U(N_1, N_2 - 1) \tag{2.28}$$

Inserting the above expression (Equation 2.22) for the total electrostatic energy $U(N_1, N_2)$ leads to the following expressions for the electrochemical potentials:

$$\mu_1(N_1, N_2) = \left(N_1 - \frac{1}{2}\right) E_{C1} + N_2 E_{Cm} - \frac{1}{|e|}\left(C_{g1}V_{g1}E_{C1} + C_{g2}V_{g2}E_{Cm}\right) \tag{2.29}$$

$$\mu_2(N_1, N_2) = \left(N_2 - \frac{1}{2}\right) E_{C2} + N_1 E_{Cm} - \frac{1}{|e|}\left(C_{g1}V_{g1}E_{Cm} + C_{g2}V_{g2}E_{C2}\right) \tag{2.30}$$

Analogously to Equation 2.17, one can define the addition energy of dot 1 and dot 2 by

$$E_{add1} = \mu_1(N_1 + 1, N_2) - \mu_1(N_1, N_2) \quad (2.31)$$

$$E_{add2} = \mu_2(N_1, N_2 + 1) - \mu_2(N_1, N_2), \quad (2.32)$$

corresponding to the charging energies E_{Ci} of the respective dot. Note that so far only electrostatic interactions were considered, while the discrete energy spectra of the dots are not yet included in this model. However, this purely classical model already suffices to construct the charge stability diagram (CSD) of a double quantum dot [48] (see Figure 2.12). The charge stability diagram - or honey comb diagram - represents the equilibrium charge configuration of the DQD as a function of the two gate voltages V_{g1} and V_{g2} that are used to control the number of electrons in the system. In case of

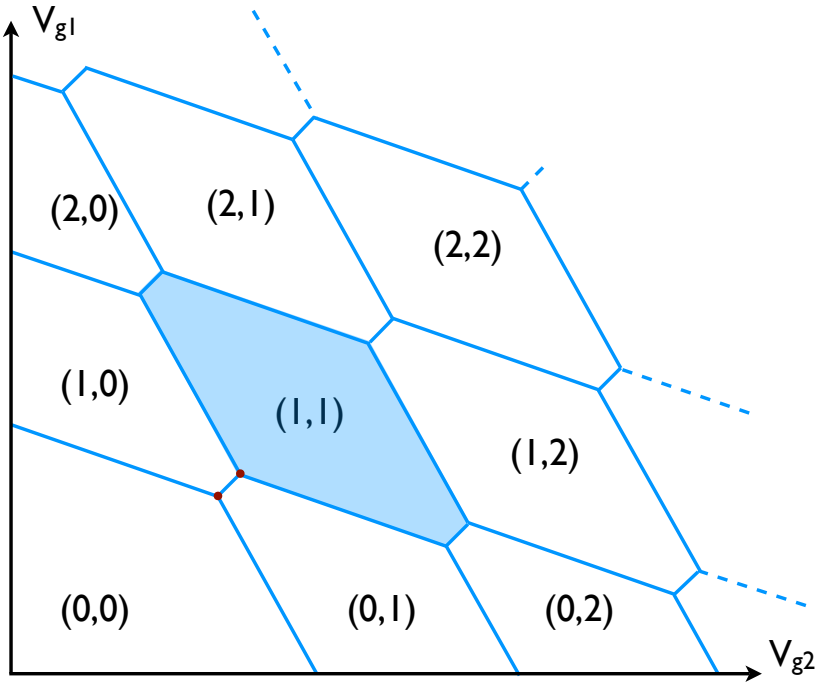

Figure 2.12.: Charge stability diagram of a double quantum dot according to the model described in the text. Stable charge configuration of the DQD build hexagonal domains, e.g. the blue shaded (1,1) configuration. The plotted charge transition lines correspond to a change in electron number. The red points indicate two of the so-called triple points, where three different charge states are degenerate.

zero source-drain bias, i.e. $V_{SD} = 0$, and in case of neither vanishing nor dominating inter dot coupling ($C_m \neq 0$ and $C_m/C_i < 1$), the stable charge configurations of a double quantum dot are hexagons (Figure 2.12). The borders of those hexagons correspond to a change of the electron configuration in the DQD system and are called charge transition lines. The edges of those hexagons are called triple points, since here

three different lines meet, i.e. at those points three different charge configurations are degenerate.

The final step in this model is to incorporate the discrete energy spectra which are present in both dots. Independently of how those discrete energy spectra are calculated, one can label the energy of level n by E_n and introduce a new electrochemical potential $\mu_{i,n} = \mu_i^{class} + E_n$ which includes E_n alongside the previously used classical electrochemical potential. The addition energy can then be written as:

$$E_{add1} = \mu_{1,m}(N_1 + 1, N_2) - \mu_{1,n}(N_1, N_2) = E_{C1} + \Delta E \tag{2.33}$$

$$E_{add2} = \mu_{2,m}(N_1, N_2 + 1) - \mu_{2,n}(N_1, N_2) = E_{C2} + \Delta E \tag{2.34}$$

As in the case of a single quantum dot, the addition energy now consists of two contributions, the classical charging energy and the quantum mechanical single particle level spacing. The energy ΔE only is required in case an electron has so be added to the next orbital state. The electron configuration, which minimizes the total energy of the DQD, is referred to as the ground state of the system, while any other configuration is an excited state. Obviously, the electron configuration corresponding to the ground state, is a function of the gate voltages V_{g1} and V_{g2}. Figure 2.13 depicts the (0,0) to (1,1) transition of the charge stability diagram in more detail. Here, different configurations of the DQD electrochemical potential are depicted with respect to the chemical potential of source and drain. Note that the configurations displayed in Figure 2.13 are only valid as long as there is no source-drain bias applied, i.e. $V_{SD} = 0$. At finite bias $V_{SD} \neq 0$, the charge stability diagram shows additional features, so-called bias triangles. They represent configurations of the DQD, where electron transport through the system is allowed and a current is flowing. The physics of non-linear transport through a DQD is discussed in detail in [48].

A thorough analysis of the position of the electrochemical potentials in the DQD with respect to the chemical potential in the leads is of great importance for understanding the experiments and calculations described in chapter 5. The six insets in Figure 2.13 show different configurations of the electrochemical potential in the dots with respect to the chemical potential in the leads. On the borderlines of the charge stability diagram (black lines), either μ_1 oder μ_2 is aligned with the chemical potential in the leads, while μ_1 and μ_2 differ from each other. Only on the line connecting two associated triple points, μ_1 and μ_2 are aligned, therefore this line is referred to as the zero-detuning line. At the triple points, not only the μ_1 and μ_2 have the same energy, they are additionally aligned with the chemical potential in source and drain. The ground state of the DQD is now defined by the relation between the two electrochemical potentials.

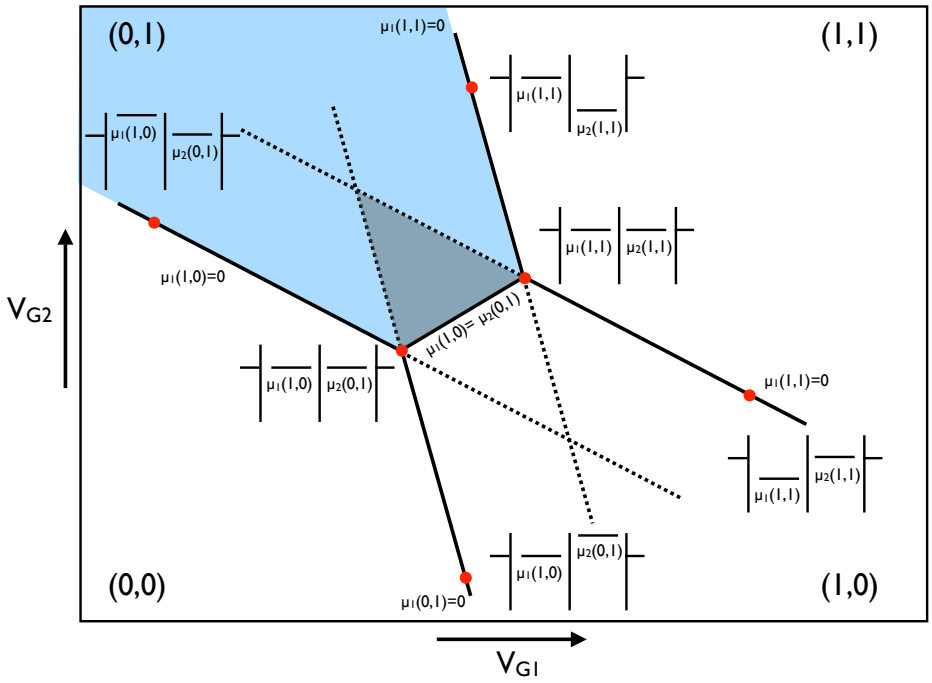

Figure 2.13.: Schematic representation of the (0,0) to (1,1) transition in the CSD of a DQD. The six red points correspond to the six insets and depict the position of the electrochemical potential in the DQD with respect to the chemical potential in the leads. The blue and grey shaded areas are discussed in detail in the text. (redrawn after van der Wiel *et al.* [48])

For example in the blue shaded (0,1) region of the CSD in Figure 2.13, μ_2 is lower in energy than μ_1, therefore the (0,1) state is energetically favorable. The situation is reversed in the (1,0) area, since here μ_1 lies lower in energy. Another important case can be found in the gray shaded region in Figure 2.13. Here, (0,1) is the ground state since μ_1 lies higher in energy than μ_2, but μ_1 still lies beneath the chemical potential in source and drain. Therefore, both states are theoretically energetically accessible. The same situation can be found on the other side of the zero-detuning line, but now again with μ_1 lying lower in energy than μ_2. Therefore, within the diamond shaped area indicated by the dotted lines in Figure 2.13, both μ_1 and μ_2 are energetically accessible, leading to thermally activated tunneling processes, described in detail in chapter 5. Measured charge stability diagrams are shown and described in Figure 2.14 and Figure 2.15.

So far, all considerations made here are still purely classical. Only in Equation 2.34 the discrete energy spectra of the dots are taken into account in order to express the addition energies. In the experiments on DQDs presented in this work, the tunnel coupling between both dots was made very small[9] and therefore the effects caused by

[9]The inter dot tunneling rate lies below 5 Hz.

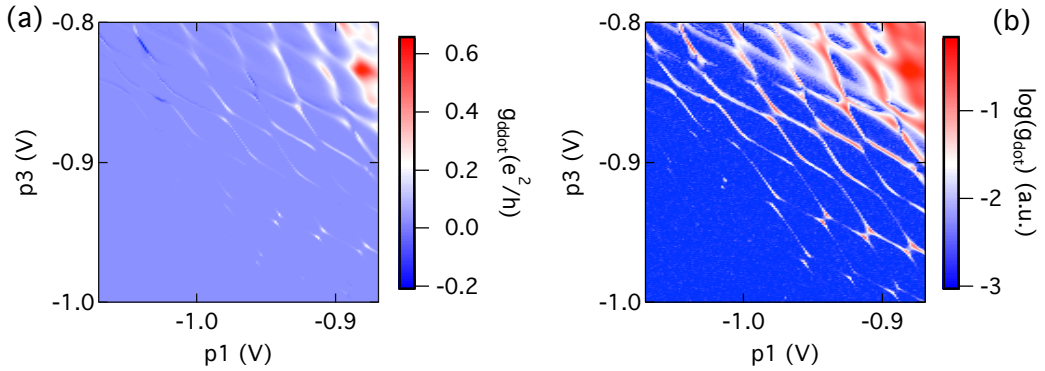

Figure 2.14.: (a) Transport measurement on a double quantum dot, where the conductance through the system is probed as a function of p1 and p3 (see. Figure 2.2). Different charge configuration, i.e. honey combs, can be distinguished. For more negative gate voltages, the number (N_1, N_2) of electrons in the DQD is reduced, while simultaneously the tunneling rates to source and drain are decreased. Due to the reduced tunneling rates, the measured conductance becomes smaller and finally is no longer detectable. Therefore it is often not practicable to perform transport measurements in the low electron regime. (b) Same data set as in (a) but on a logarithmic scale.

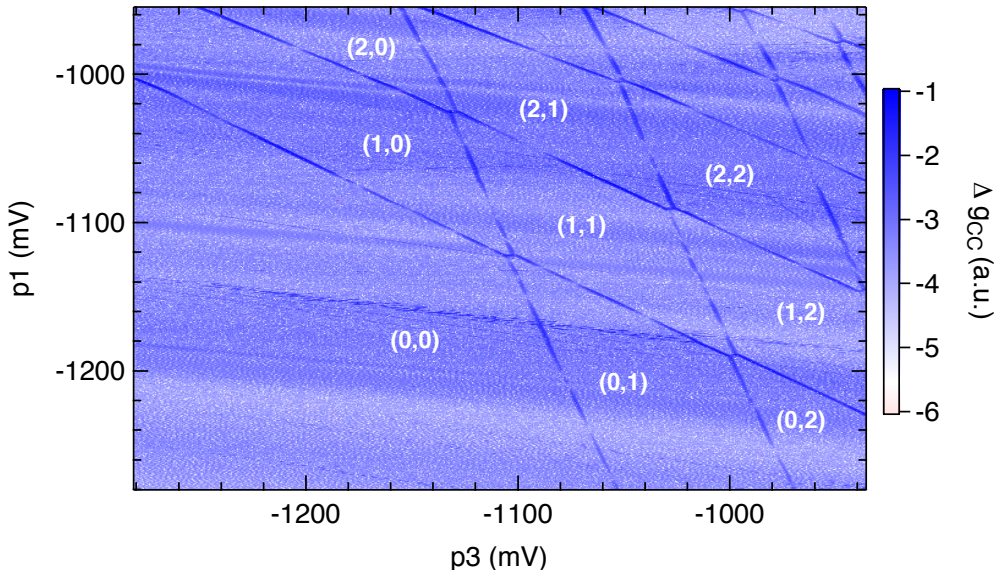

Figure 2.15.: Experimental charge stability diagram of a DQD sample similar to Figure 2.2. The depicted data was not obtained by performing transport measurements, instead this plot shows the change of a charge sensor signal (see. chapter 3) as a function of the the two gate voltages p1 and p3 (which correspond to V_{g1} and V_{g2} in the text). The lines in the charge sensor signal correspond to changes in the DQD charge configuration. Therefore, one can distinguish different charge configurations, including the (0,0) state, where the double dot is completely empty.

the coupling between both dots where minimal. However, this is not the general case and indeed in most experiments on DQDs the inter dot tunneling is of great importance. The strongest effect of inter dot coupling on the CSD appears around the triple point, where the sharp kinks (Figure 2.12) are rounded, such that the previously well-defined hexagons are less distinct. This effect is already visible in the data shown in Figure 2.14, where for less negative gate voltages the inter dot coupling increases.

A non negligible inter dot coupling corresponds to an additional interaction between the discrete energy levels of the two quantum dots. In case of a single electron per dot, the system can be modeled by a Hamiltonian of the form

$$\mathbf{H} = \begin{pmatrix} E_1(V_{g1}, V_{g2}) & \gamma_{12} \\ \gamma_{12}^* & E_2(V_{g1}, V_{g2}) \end{pmatrix}, \tag{2.35}$$

where E_i represents the energy of the respective dot level and γ_{12} is a matrix element describing the coupling between both states [4, 20, 48]. Problems like this are well know from basic quantum mechanics and are referred to as two-level system [68]. Diagonalizing the above Hamiltonian gives the two eigenenergies of the system

$$E_\pm = \frac{E_1 + E_2}{2} \pm \frac{1}{2}\sqrt{(E_1 - E_2)^2 + 4|\gamma_{12}|^2} = E \pm \frac{1}{2}\sqrt{\epsilon^2 + 4|\gamma_{12}|^2}, \tag{2.36}$$

where $\epsilon = E_1 - E_2$ is the detuning[10] between the dots and $E = (E_1 + E_2)/2$ is the average energy of both states. From Equation 2.36 one can see, that for vanishing coupling $\gamma_{12} = 0$ the resulting energies are the unperturbed energies E_1 and E_2 of the DQD. For a non-vanishing inter dot coupling both energies change, leading to the already described changes in the charge stability diagram.

The situation is even more complex in presence of magnetic fields and if one shifts the focus of attention to the border of the (1,1) and (0,2) hexagon of the CSD, or to even higher transitions. The electrons involved in the (1,1) to (0,2) transition, form singlet- and triplet states, as they are known from atomic physics [20]. The lifted spin-degeneracy leads to the observation of e.g. spin-blockade and other spin related effects [69, 70]. Finally, it is in this regime and e.g. at this transition, where a double quantum dot can be operated as a spin-qubit.

[10]The detuning here is identical to the (zero-)detuning described above. In general, the term detuning in this context refers to energy difference between associated energy levels in the left and the right QD.

Chapter 3

Real-Time Measurements

In the limit of very small tunneling rates between (double) quantum dots and leads, transport measurements become impossible because the current through the dot is to small to be measured. Therefore, one has to use another technique to probe tunneling processes and charge configurations in the investigated system - charge sensing [24, 43, 57, 71–75]. Almost all experimental data presented in this work was obtained by charge sensing measurements, hence this chapter treats its experimental implementation and technical realization. The first section of this chapter introduces charge sensing with quantum dots, and explores advantages and disadvantages using a QD in comparison to a quantum point contact (QPC), which also can be used as charge sensor. The following two sections treat the implementation of real-time measurements and the characterization of the real-time setup with respect to technical quantities such as bandwidth and noise.

3.1. Charge Sensing with QPCs and Quantum Dots

Reaching the few electron regime of a gate-defined quantum dot is difficult. That is because lower electron numbers can only be obtained by applying more negative voltages to the depletion gates, which inevitably reduces the tunneling coupling to the leads as well. The layout of the depletion gates and the design of the nanostructure play a crucial role here. Therefore, one tries to probe quantum dots with other devices that are immune to this effect, but maintain their sensitivity to changes of the quantum dot's charge state. A first attempt was made by Field *et al.* [43], using quantum point contacts [45, 46] as charge sensors. This new sensor technique proofed to be very versatile and was used in different experiments, e.g. in experiments related to the Kondo- or dephasing effects [76, 77]. Finally, charge sensing with QPCs was used to probe the few electron regime in quantum dots and double quantum dots [78–80], while simultaneously a theoretical treatment of charge sensing was developed [81–86].

The basic idea of charge sensing is to position a sensor device in direct proximity to the object of investigation. The standard choice is the aforementioned quantum point contact. The charge sensor and the investigated object, which in this work is either a QD or a DQD, belong to separate electric circuits. This fact is displayed in in Figure 3.1 (a), where the blue and red arrows indicate the different electric circuits. Therefore, there is no charge transfer between sensor circuit and device circuit. The current flowing through the sensor circuit can be measured simultaneous to transport measurement on the QD/DQD. As a function of gate voltage, the QPC-sensor shows the typical G-V characteristic with quantized conductance steps at multiples of $2e^2/h$ (see. Figure 3.1 (b)) [45, 46]. The G-V-characteristic of the QPC, however, depends rather sensitively on the electrostatic environment. Therefore, an electron tunneling on or off the QD leads to a change in the potential landscape, because the number of charges in the system is changing. As a result, one can observe small kinks in the G-V-characteristic of the sensor QPC, which are related to tunneling processes in the adjacent QD. An example is given in Figure 3.2, where a raw sensors signal is depicted

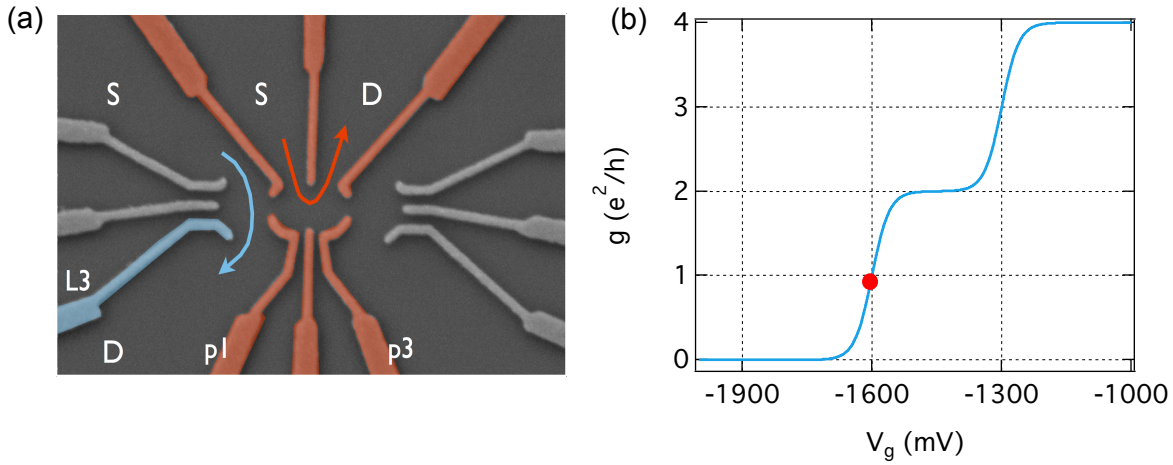

Figure 3.1.: (a) SEM picture of a device similar to the investigated sample, with gates used to form a QD/DQD artificially marked red. The blue marked gate is used to from the sensor QPC. The arrows indicate where current is flowing and that those two electric circuits are separated form each other, i.e. no current flows between sensor QPC and QD/DQD (b) Theoretical G-V characteristic of a QPC. The QPC's conductance is quantized in multiples of $2e^2/h$ (at $B = 0$) and between individual conductance steps, the G-V characteristic changes rapidly. Consequently, the slope is largest between two associated steps and hence the QPC is operated in this regime (red dot). Here, a small change in the potential landscape of the sensor QPC leads to the strongest change in the its conductance, i.e. the highest sensitivity.

alongside a processed version of the same data and a direct transport measurement on

the QD. The charge sensor can be characterized by its sensitivity, defined as

$$\eta = \frac{\Delta G_{sen}}{G_{sen,op}}, \tag{3.1}$$

where ΔG_{sens} is the change in sensor conductance due to an electron tunneling of the probed system, while $G_{sen,op}$ is the conductance at the operation point of the sensor. This operation point has to be chosen with respect to the slope of the sensor's G-V characteristic. A steep slope leads to a large change ΔG_{sen}, since here small changes of the potential landscape have the highest influence on the sensor's conductance. Additionally, the sensitivity also depends on geometrical properties such as the distance between sensor and device. This distance is of course predefined by the layout of the nanostructure, hence devices with charge sensors have to be designed accordingly. In

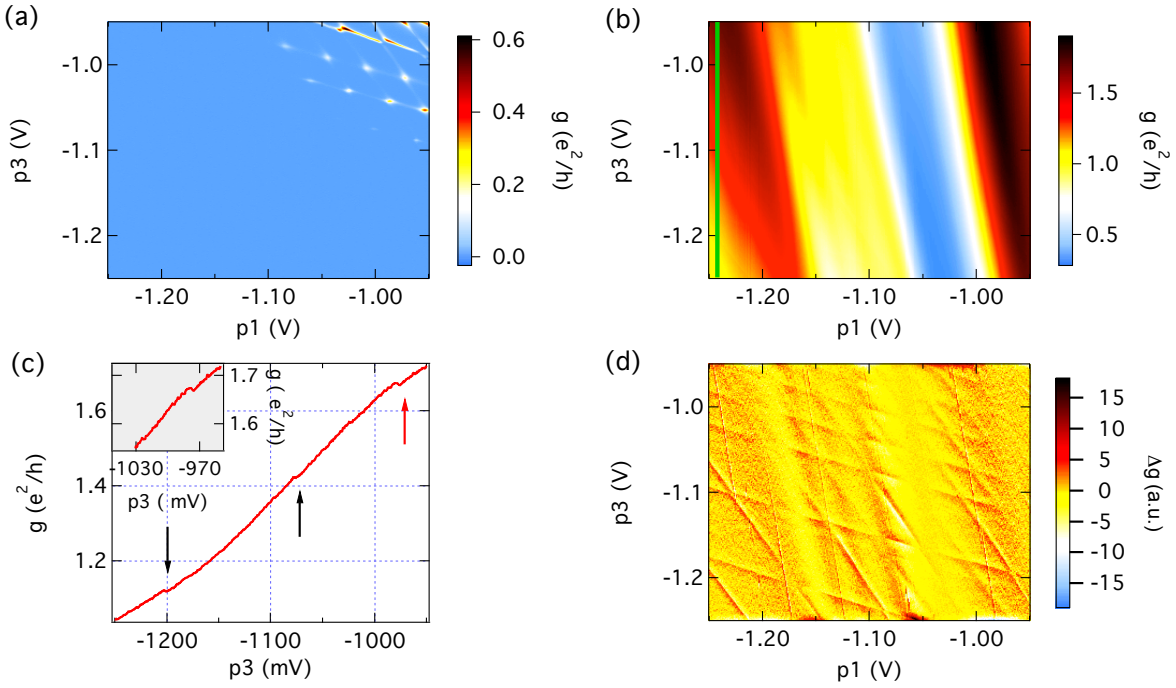

Figure 3.2.: (a) Transport measurement on a DQD device, where for less negative gate voltages the conductance through the system is still measurable. For more negative gate voltages, i.e. lower electron number, the transport signal vanishes due to the simultaneous decrease of tunneling rates to source and drain. (b) Charge sensor signal obtained with the QPC shown in Figure 3.1. (c) Cut-trough of the data in (b) at the green line. The arrows indicate small kinks in the sensor signal corresponding to tunneling processes in the DQD. The inset shows a zoom-in around the kink indicated by the red arrow. (d) Same data set as in (b) but in a processed version. Applying a background subtraction (see. Appendix B), reveals the kinks in the sensor signal.

general, the operation point for a QPC charge sensor is chosen to lay between the pinch-off region and the first conductance step. Here, the slope is steep and for more negative gate voltages, i.e. lower number of 1D-modes, the QPC moves closer to the

investigated device. For higher conductance steps the slope is equally steep, but here $G_{sen,op}$ increases, hence η decreases. This procedure ensures a maximum in sensitivity and one can obtain sensitivities in the range of $\eta = 0.01$ to $\eta = 0.1$, i.e. the sensor signal changes up to 10%. Figure 3.2 demonstrates that raw QPC-sensor data require additional processing in order to give a distinct signal. However, in the experiments presented here, charge sensing with QPCs was not optimized to give the best results. Instead, charge sensing with QPCs was only a intermediate step on the way to implement a sensor quantum dot.

The quality of charge sensing data can be improved tremendously when replacing the sensor QPC with a sensor quantum dot (SQD) [47, 87, 88]. The principle of operation remains the same but the much steeper slope of Coulomb oscillations in a SQD, compared to the G-V characteristic of a QPC, makes it the superior sensor device. Essentially, the slope of Coulomb oscillations in the SQD is only limited by temperature broadening, while the G-V characteristic of a QPC is given by the confining saddle-point potential. The operation point of a SQD has to be chosen such that it lies on the flank of a Coulomb peak. Figure 3.3 (b) depicts an exemplary measurement of Coulomb oscillations in a sensor-dot, alongside one possible choice for the operation point and the corresponding sensor-dot configuration (Figure 3.3 (a)). The

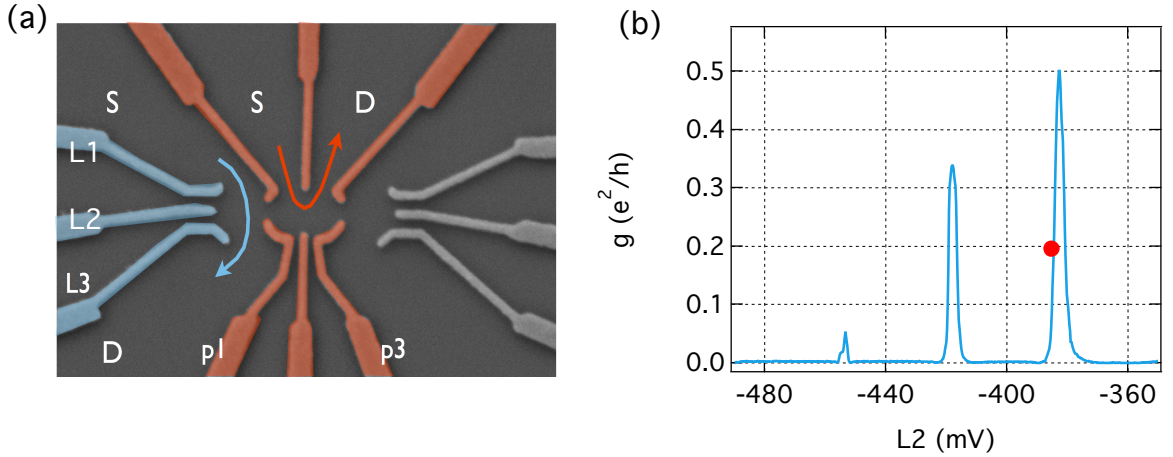

Figure 3.3.: (a) SEM picture of a device, where the artificially red marked structures correspond to gates used to form the (double) quantum dot. The blue marked structures indicate gates used to form the SQD. Here, the SQD on the left hand side is operated, but in general both SQDs work completely analogue. The blue and red arrows depict where current flows through the device and points out, that both circuits are independent of each other. (b) Exemplary measurement trace of Coulomb oscillations for the SQD marked in (a). The red dot indicates s suitable operation point of the sensor device.

increased sensitivity of a SQD also introduces additional complications. Although the DQD device and the sensor quantum dot are separate electric circuits, there still is

a capacitive coupling between them. This is also true for QPC sensor, but the resulting consequences are more drastic for a SQD. Performing a measurement on the DQD device requires sweeping through the voltages of to those gates, that are used to alter the number of electrons in the device. Via the capacitive coupling between sensor quantum dot and DQD device, these changes will drive the sensor away from the adjusted operation point. This dramatically influences the sensitivity of the sensor quantum dot. Whenever the sensor's operation point is driven into the gap between two associated Coulomb peaks, the sensitivity is reduced to zero and charge sensing becomes impossible. Whenever the operation point of the sensor lies on one of the Coulomb peaks, there still remains a non-zero sensitivity, which strongly depends on the corresponding slope of the Coulomb peak. An optimal charge sensor should be independent of such capacitive influences in order to have a fixed, maximal sensitivity. Therefore, one tries to compensate the capacitive coupling to the SQD device by introducing a feed-back mechanism. The implementation of this feed-back mechanism is described in Appendix B. Charge sensing with quantum dots is optimized by this feed-back procedure, hence all following measurements presented in this thesis were performed with this technique. Figure 3.4 gives an example for the quality of the obtained charge sensing data. The resulting sensitivity is increased drastically, compared to a sensor QPC. As is indicated in Figure 3.4 one can obtain sensitivities of $\eta > 2$, which corresponds to a change in the sensor's conductance of more than 200%. For such extreme sensitivities, one also can observe additional effects, like the one indicated in Figure 3.4 (c) and (d). Here, the sensitivity for tunneling events in the left sensor is much smaller than for tunneling processes in the right part of the DQD. This effect is caused by the increased distance between the SQD - which in this case is the left SQD - and the right dot in the DQD system. The situation is reversed for data obtained with the right sensor quantum dot, confirming the above explanations.

The sensor feed-back mechanism used for the measurements presented here, works very good on small scales, i.e. for small voltage changes at the gates of the DQD device (see. Figure 3.4). On larger scales, there are still features present in the data, which are due to the capacitive coupling. The reason for this is, that the implemented feed-back mechanism is linear in gate voltage, which, of course, is an approximation. When sweeping through larger ranges of gate voltage, the feed-back will become inaccurate and start to either overcompensate, or under-compensate. Thereby, the SQD will be driven through different Coulomb oscillations and its conductance will depend strongly on gate voltage again. This effect is visible in the data display in Figure 3.5. Different Coulomb peaks can be distinguished in Figure 3.5 (a) and the SQD conductance varies between 0 and 0.7 e^2/h. On the right hand side of Figure 3.5, the same data is shown after subtracting a background. Clearly, the charge transition lines of the CSD are

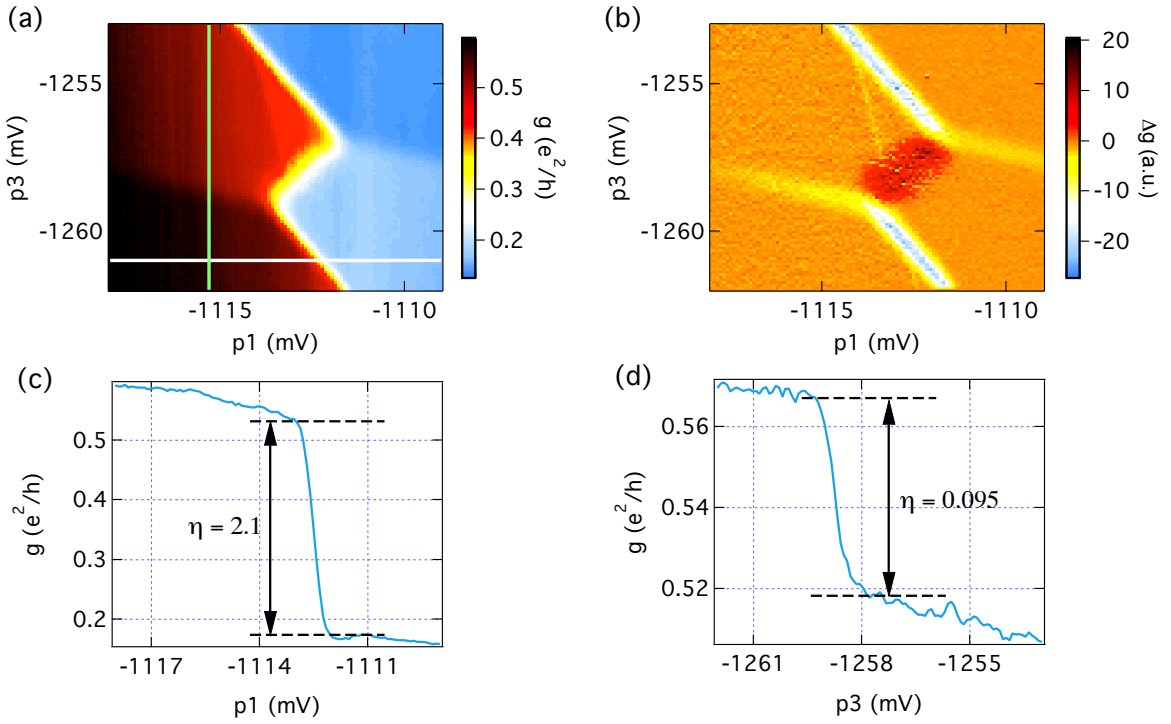

Figure 3.4.: (a) Data obtained with the left sensor dot (see. Figure 3.3). The part of the CSD displayed, corresponds to the (0,0) to (1,1) transition. (b) Same data as in (a), but after subtracting a background from the raw data. (c) Cut through (a) at the white line, corresponding to the (0,0) to (1,0) transition. Here, the tunneling process occurs in direct proximity to the SQD, which leads to extraordinary high sensitivities. (d) Cut trough (a) at the green line, corresponding to the (0,0) to (0,1) transition. Due to the increased distance between the tunneling event and the sensor, the sensitivity is smaller than in (c).

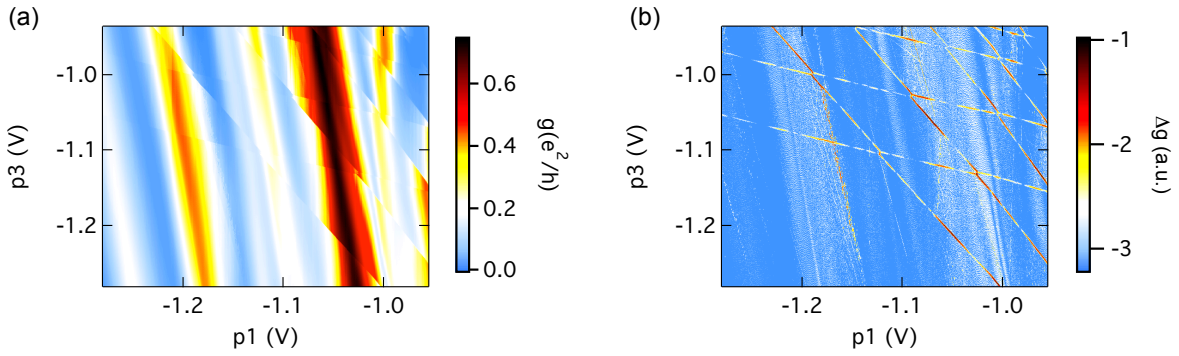

Figure 3.5.: (a) SQD data as a function of gate voltage p1 and p3. Both gate voltages are varied over more than 200 mV, which cannot be compensated by the linear feed-back mechanism of the SQD. Consequently, the SQD's conductance is not held constant, instead the SQD is driven over different Coulomb peaks, due to the capacitive coupling to the DQD device. (b) Same data as in (a), but after subtracting a background from the raw data. One clearly can distinguish the CSD of the probed DQD.

much more distinct here, than in the raw data. Hence, the lack of accuracy of the feedback mechanism on larger scales does not spoil charge sensing measurements in general. By applying additional software tools like the aforementioned background subtraction, those measurements reveal strong and clear charge transition lines, suitable for further analysis.

3.2. Real-Time Charge Sensing

The charge sensing measurements described so far, were time-averaged measurements. The experiments described in this thesis, however, require real-time measurements, i.e. the response time of the charge sensor has to be fast compared with single tunneling processes. Only if this condition is fulfilled, single electrons tunneling on an off a quantum dot can be monitored. Real-time charge sensing can be realized in various ways, all of them having their own advantages, disadvantages and technical challenges. Basically, one can differentiate between three different types of real-time charge sensing setups. The first method relies on room temperature electronics and only requires standard amplifiers and a DC voltage source [89]. Here, a DC-bias is applied across the SQD, while a current amplifier/I-V converter is used to detect and amplify the sensor's response. The second approach is very similar, except the room temperature I-V converter is replaced with a cryogenic amplifier [90]. In order to realize a faster readout, i.e. a higher bandwidth (BW), a high electron mobility transistor (HEMT) is used as amplification device. Usually this transistor is cooled down to helium temperature or even 1 K, in order to get the optimal results. The advantage of this approach, compared to room temperature electronics, is to minimize thermal noise from the amplifier and to obtain a higher bandwidth. A disadvantage of setups like this is the reduced flexibility, i.e. the possibility to do modifications and maintenance during measurement periods, since any change on the transistor is impossible as long as it is cold. The third method to realize real-time charge sensing, is integrating the SQD into an impedance matching circuit. A radio-frequency signal (rf-signal) is used to excite the system and the reflected power is monitored as a function of the sensor resistance [71, 88, 91]. This approach is the technically most sophisticated one and provides very high bandwidths in the order of MHz, depending on the resonance frequency of the tank circuit. One big challenge of such setups is to decrease electron temperatures below 100 mK. This is due to heating through the electric components of the impedance matching circuit.

All real-times measurements presented in this thesis are done by using the first of the three presented approaches. This is justified by the benefit of lower electron temperatures alongside a high flexibility of the real-time setup, together with a sufficiently high bandwidth. The realization of the real-time setup for the experiments described here,

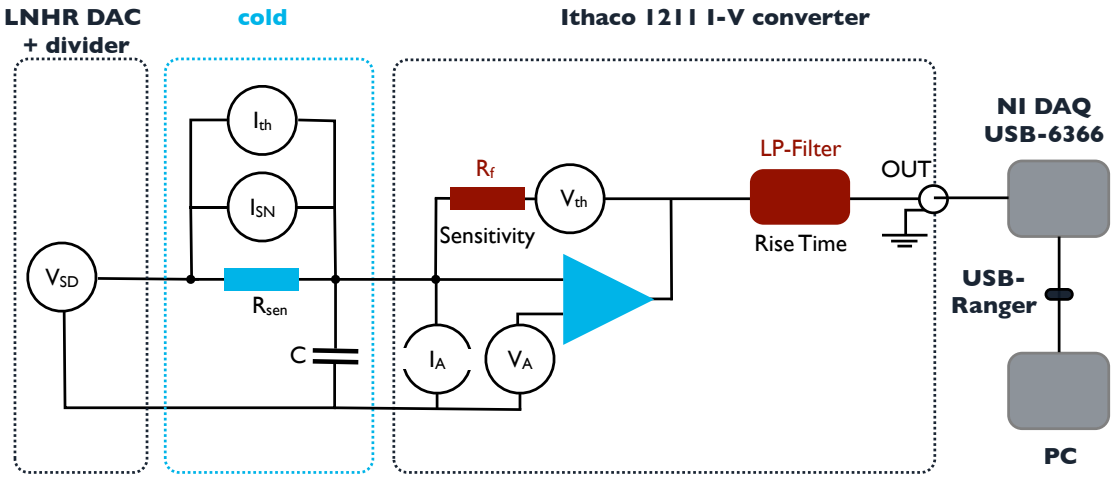

Figure 3.6.: Illustration of the real-time measurement setup. A LNHR DAC in combination with a voltage divider is used to apply a DC bias V_{SD} across the sensor. The electrical connections to the dilution refrigerator are twisted pair cables with additional, homemade filters [92]. R_{sen} is the combined resistance of sensor and twisted pairs. C represents the combined capacitance of filters and lines. The sensitivity of the I-V converter is defined by the feed-back resistor R_f. Additionally, a low pass filter is used to optimize the signal-to-noise ratio. This filter defines the rise-time of the system, hence the bandwidth of the setup is smaller than the technical maximum, which is reached by turning off the LP-filter. I_{SN}, I_{th}, V_{th}, V_A and I_A are noise sources, discussed in detail in the main text.

is subject of Figure 3.6. A LNHR DAC[1] is used as DC voltage source, together with homemade voltage dividers. The DC bias applied across the SQD changes from 10 µV to 250 µV, with 60 µV being the standard value. A commercially available Ithaco 1211 I-V converter amplifies the sensor signal, while a NI USB-6366 DAQ (Data Aquisition Device) is used to digitize the data. Finally, the NI-DAQ is connected via USB to the measurement computer with a USB-ranger in-between to avoid ground loops.

The NI-DAQ has a nominal data acquisition rate of 2 MHz. Here, however, the bandwidth of the setup is limited by the I-V converter to 25 kHz[2], therefore measuring with the full acquisition rate is not meaningful. Instead, the signal is integrated over a certain amount of time, e.g. 1 ms, and afterwards the average and standard deviation of this measurement interval are calculated. Thereby it is possible to drastically improve the signal-to-noise ratio (SNR). Additionally, this procedure allows to investigate the transition form the real-time regime (shorter integration intervals) to the non-real-time regime (longer integration intervals). For longer integration intervals the measured signal resembles the data obtained by generic transport measurements

[1]The LNHR DAC (low noise high resolution digital analogue converter) is a DC voltage source made by the electronics workshop of the University of Basel, under the direction of Michael Steinacher.

[2]Since bandwidth and noise are important issues for all real-time measurements, both topics are covered in more detail in the succeeding section of this chapter.

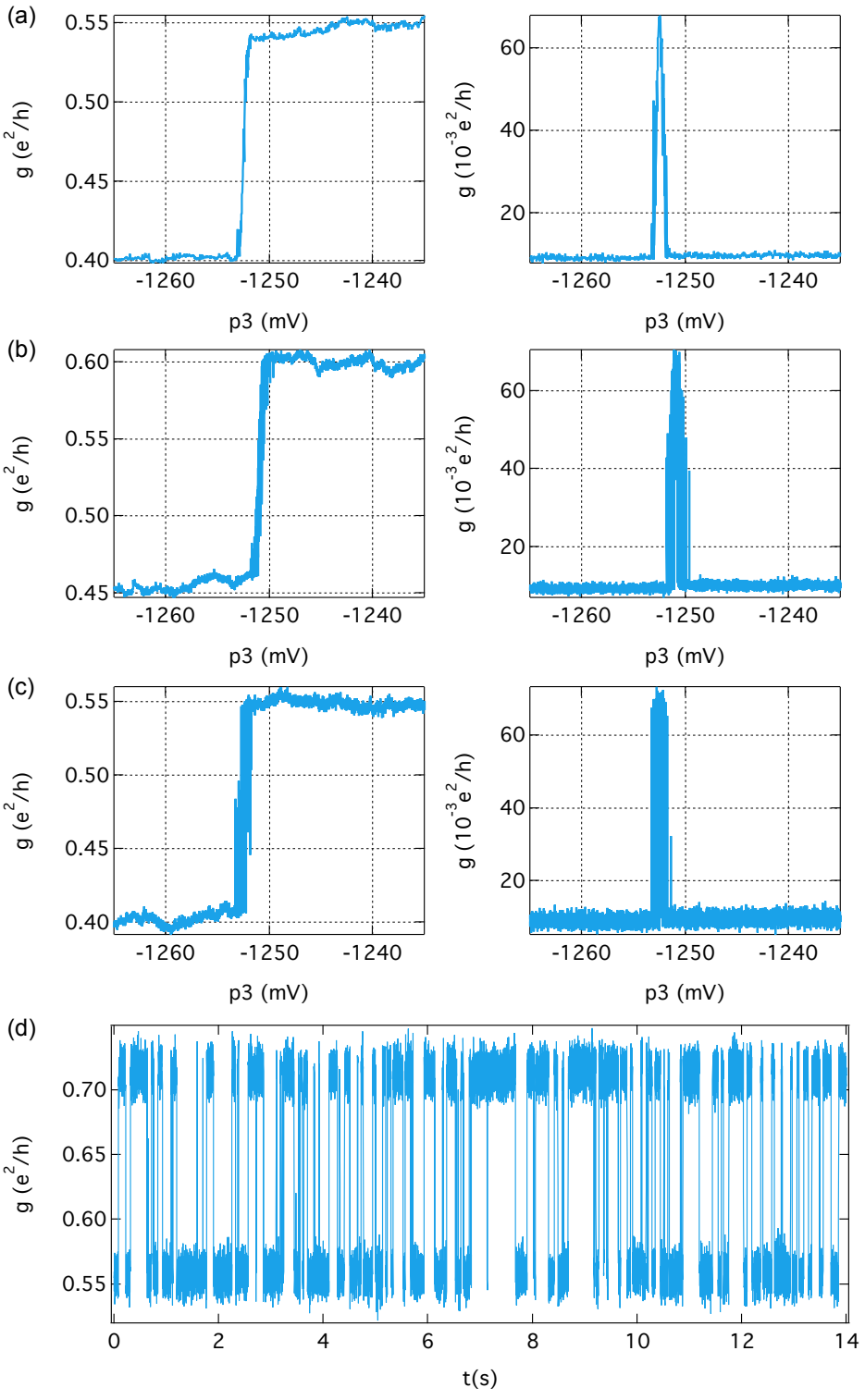

Figure 3.7.: (a) SQD conductance as a function of plunger gate voltage p3 (left pannel). Each data point is integrated for 1.5 s. For each integration interval average (left panel) and standard deviation (right panel) are calculated. (b) and (c) Same measurement as in (a), but with a reduced integration time of 0.5 s and 20 ms. (d) Real-time data, where the sensor signal is measured vs. time at the transition between $N = 1$ (upper level) and $N = 0$ (lower level) in a QD.

as they are described in chapter 2. Figure 3.7 illustrates this effect for three different integration intervals, 1.5 s, 0.5 s and 20 ms. Here, the observed electron transition gets better resolved for shorter integration intervals, as more single tunneling events can be detected. The standard deviation calculated from the integration intervals is depicted in Figure 3.7 as well and shows a pronounced maximum at the point of the electron transition. Calculating the standard deviation of such a measurement interval is extraordinary useful, scince it can serve as a efficient trigger to determine whether or not tunneling events occur at a certain gate voltage. For gate voltages fixed to the position of an electron transition, measurements against time show a telegraph-noise like signal as in Figure 3.7 (d). Here, electrons are tunneling resonantly on and off the QD with rates that are resolvable with the real-time setup.

3.3. Bandwidth and Noise

The sensitivity of the I-V converter is controlled by the feed back resistor R_f (see Figure 3.6) on the input side, which also defines the input resistance and thereby the theoretical maximum bandwidth of the setup [89]. For a sensitivity of 10^{-7} A/V the bandwidth is 25 kHz, while for 10^{-8} A/V the bandwidth already is reduced to 10 kHz. For even higher gains of the I-V converter, the bandwidth reduces further and overshoots, caused by the amplifier, make the evaluation of real-time data difficult. Lower gains lead to a decreased signal-to-noise ratio, hence additional filtering is required, which again reduces the bandwidth. For a sensitivity of 10^{-7} A/V or 10^{-8} A/V the signal-to-noise ratio still has to be improved by using the built-in low pass filter (LP-filter) of the I-V converter. Typically, the LP-filter is adjusted to a rise times between 0.03 ms and 0.1 ms[3], hence the bandwidth of the real-time setup lies between 1.1 kHz and 11.6 kHz. From the necessity of additional filtering it follows, that the limiting factor of the real-time measurements is the signal-to-noise ratio and not the technical bandwidth. Improving the real-time setup therefore requires an increased SNR, which has to be achieved through noise reduction.

In order to reduce the noise level of the measurement setup, one has to identify all possible source of noise and try to minimize their influence on the setup. Further, one has to distinguish between extrinsic noise sources, i.e. noise caused by electronic components and power supplies, and intrinsic noise sources, caused by fundamental physical effects. Figure 3.8 shows a measured noise spectrum of the real-time setup.

[3]In this case the 10%-90% rise times τ_r is used, while in general the $1/e$ time constant $\tau = RC$ is used throughout this thesis. Consequently, one has to take into account the conversion factor of $ln(9)$, i.e. $\tau_r = ln(9)\tau$. For calculating the bandwidth, corresponding to τ_r, the according conversion factor is $ln(9)/2\pi$, i.e. $\tau_r = ln(9)/(2\pi BW)$.

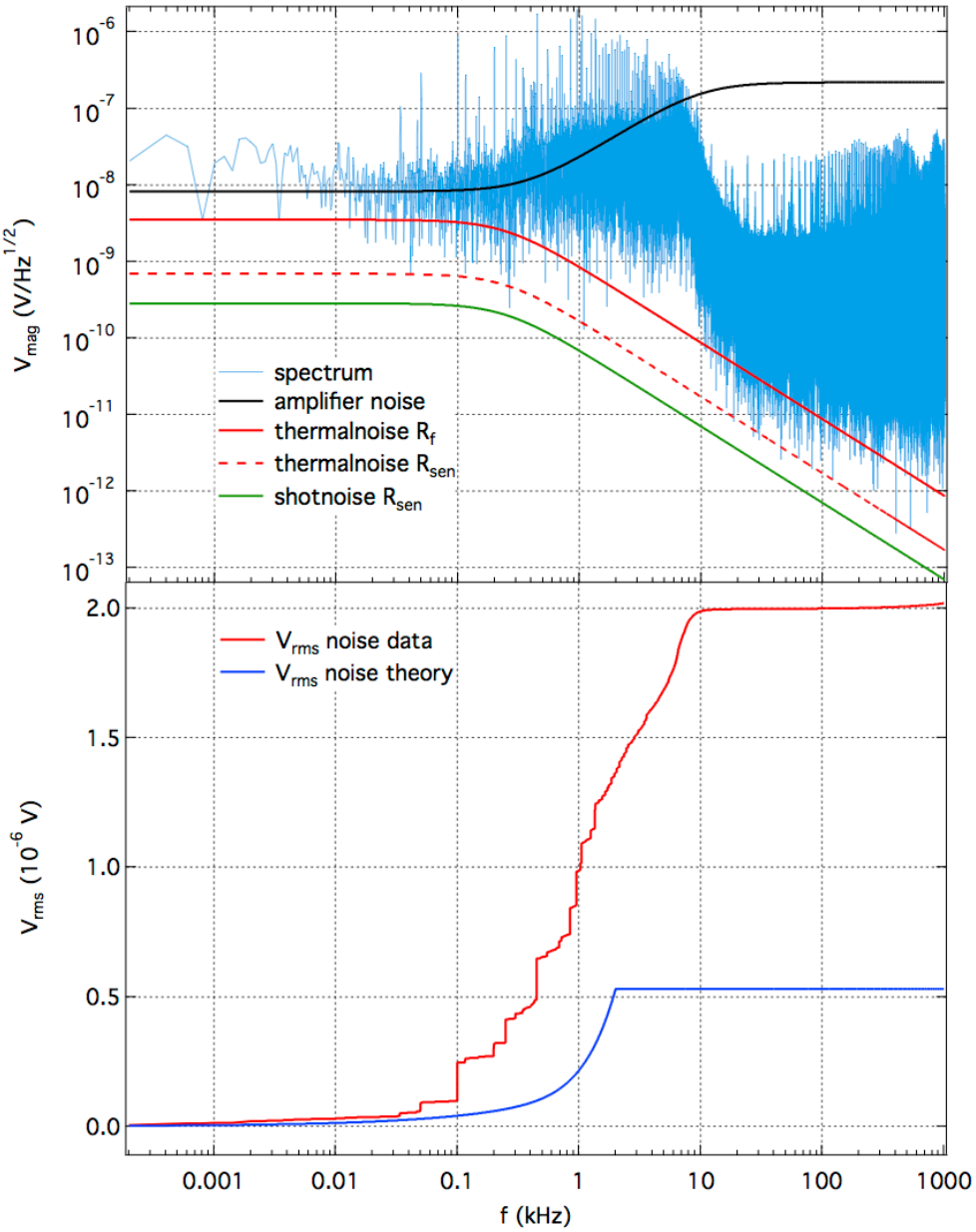

Figure 3.8.: Upper panel: Noise spectrum of the real-time setup, obtained by performing the Fourier Transform of real-time data taken with the I-V converter and the NI-DAQ (see Figure 3.6). The behavior above a frequency of 11 kHz is caused by the LP filter used to optimize the signal-to-noise ratio. Additionally, different contributions, obtained from theoretical considerations made in the text, are shown. Lower panel: Integrated noise spectrum giving $V_{rms} = 2.1 \cdot 10^{-6}$ V alongside the integrated noise of all theoretical spectra from the upper panel, giving $V_{rms} = 0.53 \cdot 10^{-6}$ V. The difference between both values gives an estimate on how much noise is picked up from other electronic components in the setup and from external sources.

From this noise spectrum one can calculate the V_{rms} noise through integration[4]. For the spectrum depicted in Figure 3.8 the result is $V_{rms} = 2.1 \cdot 10^{-6}\,\mathrm{V}$, as displayed in the integrated spectrum, which is also depicted in Figure 3.8.

One can distinguish three different intrinsic noise sources, which are relevant for the experiments described here. In any electrical conductor at finite temperature, there is thermal noise. Thermal noise - or Johnson-Nyquist noise [93–95] - does not require a mean current flow, since it is a equilibrium phenomenon, but it depends on the characteristics of the respective conductor. One can model thermal noise by a noise current I_{th}, as shown in Figure 3.6. Further, one can estimate the amplitude of this noise current by $I_{th} = \sqrt{4k_B T_e/R_{sen}} \approx 15\,\mathrm{fA}/\sqrt{\mathrm{Hz}}$, where $T_e = 100\,\mathrm{mK}$ and $R_{sen} = h/e^2$ were assumed. The corresponding voltage drop V_{th} across the RC circuit, which is formed by R_{sen} and C (In the setup described here, the capacitance of the system is about 5 nF, see Figure 3.6), is the product of I_{th} and the absolute value of its frequency dependent impedance $Z_i(f)$ [54, 95]:

$$V_{th} = I_{th}|Z_i(f)| = \left(\frac{4k_B T_e R_{sen}}{1 + (2\pi f\tau)^2}\right)^{\frac{1}{2}} \tag{3.2}$$

This function is plotted in Figure 3.8 as a function of frequency. Integrating this function gives $V_{rms} = 13 \cdot 10^{-9}\,\mathrm{V}$, which is only a small contribution to the overall noise amplitude of 2.1 µV.

In addition to thermal noise, another intrinsic noise source has to be considered, which originates from the quantization of charge - shot noise [96, 97]. In Figure 3.6, shot noise is modeled by the noise current I_{SN}, which flows parallel to the sample resistance R_{sen}. The shot noise current is given by $I_{SN} = \sqrt{2eI_{DC}\mathcal{T}(1-\mathcal{T})}$, where $\mathcal{T}$ is the transmission coefficient through the SQD. Obviously, $\mathcal{T}$ can take on values between 0 and 1 and I_{SN} vanishes for either $\mathcal{T} = 1$ or $\mathcal{T} = 0$. In order to estimate the size of I_{SN}, one can assume $\mathcal{T} = 0.5$ and get a worst-case estimate, giving $I_{SN} \approx 13\,\mathrm{fA}/\sqrt{\mathrm{Hz}}$. Here, a DC current of $I_{DC} = 2\,\mathrm{nA}$ was assumed, which is very reasonable, considering a DC bias of 60 µV and a typical resistance of about h/e^2. Analogously to Equation 3.2, one can calculate the corresponding voltage noise:

$$V_{SN} = I_{SN}|Z(f)| = \left(\frac{2eI_{DC}\mathcal{T}(1-\mathcal{T})}{1 + (2\pi f\tau)^2}\right)^{\frac{1}{2}} \tag{3.3}$$

The total contribution of shot-noise to the rms voltage noise measured in the experiment is approximately $2.5 \cdot 10^{-9}\,\mathrm{V}$, which is the smallest contribution of all intrinsic

[4]The depicted spectrum was obtained by performing a Fourier Transform of a fast measured real-time trace. The value of V_{rms} can be calculated by $V_{rms} = \sqrt{\frac{1}{T}\int_0^T \mathcal{F}^2(t)}$

noise source considered in Figure 3.8.

Finally, the third intrinsic noise source treated here, is random telegraph noise (RTN). RTN is caused by charge traps and impurities, charging or discharging as a function of time. These charging processes lead to random fluctuations of the potential landscape of the SQD and hence to discrete jumps in the sensor signal. Usually, a charge trap fluctuates between two well-defined discrete levels, but the presence of numerous such charge traps can give rise to multiple levels in the SQD signal. Such jumps disturb sensitive measurements and potentially render them impossible. For example, investigating tunneling processes in the QD/DQD is not possible if lots of RTN is present in the SQD, since the signals can barely be distinguished. Quantifying random telegraph noise is very difficult, because one has to know the precise position of charge traps and their activation can depend strongly on gate voltage. However, the number of RTN events occurring within a certain amount of time is a reasonable measure. A major switch between two levels of a charge trap in the direct vicinity of the SQD occurred approximately once every two or three days, depending on the actual gate voltage configuration. Hence, this kind of major switches only had minor influence on the experiment. In addition, there is RTN from charge traps which are further away from the SQD, leading to slow fluctuations and drifts in the SQD and the investigated QD/DQD on longer time scales. These fluctuations are more severe, because they have the potential to artificially smear out the measured Fermi functions in the experiment, which can manifest itself e.g. by the inability to resolve the Zeeman splitting. Especially, experiments that require gathering large amounts of data in order to obtain sufficient statistics, and therefore have to run for several days, are vulnerable to this effect. Therefore, one has to implement feed-back and correction mechanisms, which allow to compensate for slow drifts and fluctuations. The feed-back mechanisms implemented for the experiments described here, are treated in detail in chapter 4.

In addition to intrinsic noise sources, one has to consider extrinsic noise sources, e.g. amplifier noise, thermal noise in the amplifier and electric noise originating from power supplies, ground loops in the measurement setup or other external sources. Since a commercial I-V converter is used for all experiments, it is known from the manufacturer's specifications, that the amplifier noise is approximately $V_{spec} = 8\,\mathrm{nV}/\sqrt{\mathrm{Hz}}$ at a frequency of 1 kHz. On can model the frequency dependence of the amplifier noise by multiplying V_{spec} with the noise gain function:

$$V_{amp} = V_{spec}\left(1 + \frac{Z_f}{Z_i}\right) \tag{3.4}$$

Here, Z_f is the impedance of the RC circuit, formed by the feed back resistor R_f (see Figure 3.6) and the capacitance of the LP filter. Z_i is the impedance formed by R_{sen}

and C, both depicted in Figure 3.6. For a sensitivity of $10^{-7}\,\mathrm{A/V}$ and a rise time of 0.1 ms, one can assume $R_f = 10\,\mathrm{M\Omega}$ and $C_f = 1.2\,\mathrm{pF}$. For Z_i the same values are assumed as stated above ($R_{sen} = h/e^2$ and $C = 5\,\mathrm{nF}$). Using these values, the amplifier noise V_{amp} is calculated and plotted in Figure 3.8. The corresponding V_{rms} value is 520 nV, a considerable contribution to the overall voltage noise. As a matter of fact, the considerations made for the amplifier noise are not entirely correct. For a more precise quantification of the amplifier noise, one has to multiply Equation 3.4 with an additional function, characterizing the field effect transistor used in the amplifier. Since the required information is not available, the above model can not be adjusted any further. In general, this additional feature leads to a linear decrease (on log scale) of V_{amp} for high frequencies instead of the constant behavior (see. Figure 3.8) that is predicted by the model used here. This effect is covered by the effect of the LP filter of the amplifier, which further reduces the bandwidth of the setup to about 11 kHz in the spectrum shown in Figure 3.8. Therefore, this problem is bypassed by integrating Equation 3.4 only from 0 to 2 kHz in order to calculate the corresponding V_{rms} value. Hence, a lower limit of the amplifier noise of 520 nV is obtained.

As can be seen in Figure 3.6, there is a feed-back resistor R_f parallel to the input of the amplifier. R_f also contributes to thermal noise. Since the amplifier is operated at room temperature, the corresponding thermal noise exceeds that of the SQD by far. In Figure 3.8 the thermal noise of R_f is plotted using the formula

$$V_{th} = |Z_i(f)|I_s = \left(\frac{4k_BT}{R_f}\frac{R_{sen}^2}{1+(2\pi f\tau)^2}\right)^{\frac{1}{2}}, \tag{3.5}$$

where $I_s = \sqrt{4k_BT/R_f} \approx 46\,\mathrm{fA}$ is the corresponding noise current at $T = 300\,\mathrm{K}$ and for a feed-back resistor of 10 MΩ. Integrating this equation over frequency gives a total thermal noise of $V_{rms} = 30\,\mathrm{nV}$ originating from the feed-back resistor. Hence, thermal noise from R_f gives a small but noticeable contribution to the total noise spectrum in Figure 3.8.

In addition to amplifier noise and thermal noise in the feed-back resistor, there is always electrical noise present in the setup, which originates from power supplies, ground loops, or external sources. These noise source lead to distinct peaks in the noise spectrum (see Figure 3.8), e.g at a frequency of 50 Hz and its multiples. Extrinsic noise source can change on a daily basis. Thus, reducing extrinsic noise by avoiding ground loops, improving the electrical isolation of the system from the environment and turning off unused electronic devices is crucial. From the spectrum in Figure 3.8, one can calculate a total noise of $V_{rms} = 2.1 \cdot 10^{-6}\,\mathrm{V}$, however, in the best case V_{rms} was reduced down to$V_{rms} = 0.8 \cdot 10^{-6}\,\mathrm{V}$, while in the worst case values of $V_{rms} = 2.8 \cdot 10^{-6}\,\mathrm{V}$ and above were measured. According to the considerations made above, the theoretical

minimum is about $V_{rms} = 0.53 \cdot 10^{-6}\,\mathrm{V}$, therefore one can conclude, that the measured V_{rms} is mainly caused by additional noise pick up from electrical components in the setup and from other external sources.

Chapter 4

Investigating Tunneling Processes

Investigating single electron tunneling is essential for the experiments described in this thesis. Electrons tunnel between (double) quantum dot and leads with a rate Γ, that can be controlled via gate voltage. Hence, is it possible to tune the device to the preferred regime of tunneling rates. For fast tunneling between dot and leads, i.e. high tunneling rates, the electrons residing on the QD/DQD interact with electrons in the leads, which e.g. gives rise to the Kondo effect [98–100]. Therefore, the regime of high tunneling rates is also referred to as the Kondo regime. The situation is changed for slow tunneling, i.e. low tunneling rates. Here, electrons on the QD interact only weakly with those in the leads. In this situation, the dominant interactions are the hyperfine interaction between electron and nuclear spins of the host material, as well as spin-orbit interaction. Hyperfine interaction leads to decoherence of electron spins [23, 35, 36, 101, 102], e.g. in spin-qubits, while spin-orbit interaction couples the electron spin to the phonon bath and thereby give rise to the dominant spin-relaxation mechanism [27, 54]. Further, in the regime of low tunneling rates, one can observe thermally activated, metastable charge state switching in double quantum dots, as they are describe in chapter 5.

This chapter describes how real-time charge sensing is used to investigate electron tunneling an extract the corresponding tunneling rates. The first section of this chapter treats the basic physics of tunneling on and off a quantum dot. The next section describes, how tunneling rates are extracted from real-time tunneling data. The experiments described here require gathering large amounts of data in order to have sufficient statistics for further analysis, e.g. extracting tunneling rates. Hence, long measurement periods are inevitable and additional feedback mechanisms have to be implemented, to correct for drifts of the QD/DQD and the charge sensor. Those feedback mechanisms are described in the third section of this chapter. Finally, the last section of this chapter specifies, how tunneling rates are extracted in the presence of an external magnetic

field. Furthermore, the g-factor for GaAs is measured and the visibility of the Zeeman splitting, which is relevant for spin-relaxation time measurements, is discussed.

4.1. Tunneling On and Off a Quantum Dot

This section sets the physical foundation to understand the tunneling processes, that are investigated in this thesis. The main goal is to derive a relation between tunneling rates and measured real-time data, i.e. the measured time-intervals t_{on} and t_{off} during which an electron resides on or off the quantum dot. For the following derivation, one assumes the QD to be in the single-electron regime and that there is only one orbital energy state accessible for the electron, i.e. the excitation energy is much larger than the thermal energy $k_B T_e$. Consequently, the considered QD can either be empty, or occupied with one electron residing in either the spin-up or spin-down state. Additionally, one takes into account the possibility of two electrons residing on the dot, which of course requires the charging energy E_C for the second electron. Now one can calculate the grand canonical partition function, known from basic thermodynamics [2, 103]:

$$Z = \sum_i e^{\frac{E_i - \mu N_i}{k_B T_e}} = 1 + 2e^{-\frac{1}{k_B T_e}(E_g - \mu)} + e^{-\frac{1}{k_B T_e}(2E_g + E_C - 2\mu)} \tag{4.1}$$

In this equation, E_g refers to the QD ground state energy, while E_C is the aforementioned charging energy and μ is the chemical potential in the leads, which is often set equal to the Fermi energy E_F in semiconductor physics. In the grand canonical ensemble, the average particle occupation number is given by [103]:

$$\bar{N} = -\frac{\partial}{\partial \mu}\Omega = -\frac{\partial}{\partial \mu}(-k_B T_e \ln Z) \tag{4.2}$$

As stated above, the single-electron regime is considered here, therefore one now neglects the possibility of two electron residing one the dot, which is justified by taking into account that the charging energy E_C is typically in the order of a few meV and therefore exceeds the thermal energy by far, i.e. $E_C \gg k_B T_e$. Under this assumption, Equation 4.2 can be written as:

$$\bar{N} = \left(1 + \frac{1}{2} e^{\frac{E_g - \mu}{k_B T_e}}\right)^{-1} = P_{on} \tag{4.3}$$

In the last step of this equation, the average number of electrons in the system was identified with the probability P_{on} for an electron to reside on the quantum dot. By relating the ground state energy with gate voltage via the lever arm α, the probability

P_{on} can be written as

$$P_{on} = \left(1 + \frac{1}{2} e^{\frac{-e\alpha_g V_g}{k_B T_e}}\right)^{-1}, \tag{4.4}$$

which can be interpreted as a Fermi function, shifted by the factor $k_B T_e \ln 2$. Now on can derive a rate equation for the considered quantum dot, which incorporates the tunneling rates Γ_{on} and Γ_{off}[1]:

$$\dot{P}_{on}(t) = \Gamma_{on} P_{off}(t) - \Gamma_{off} P_{on}(t) \tag{4.5}$$

Here, one a priori assumes equal tunneling rates into the spin-up and spin-down states, as no external magnetic field is applied that would lift spin degeneracy. Since the dot is either empty or filled with one electron, one can conclude $P_{off}(t) = 1 - P_{on}(t)$, from basic probability considerations. Hence, one can derive an equation for P_{off} analogue to Equation 4.5 by inserting both relations into each other. The above differential equation is solved by

$$P_{on}(t) = \frac{\Gamma_{on}}{\Gamma_{on} + \Gamma_{off}} - \frac{\Gamma_{on}}{\Gamma_{on} + \Gamma_{off}} e^{-(\Gamma_{on} + \Gamma_{off})t}, \tag{4.6}$$

under the boundary condition $P_{on}(t = 0) = 0$, i.e. at time $t = 0$ the dot is empty. Equation 4.6 describes the dynamical process of an electron tunneling on and off a quantum dot. However, the experimental situation is different. In Figure 4.1 exemplary real-time data is depicted, showing a telegraph-noise like signal, that corresponds to resonant tunneling into the ground state. As explained in detail in the second section of this chapter, one experimentally determines the intervals of the signal, which correspond to the time an electron remains in the dot, or respectively the time during which the dot remains empty. Such a time interval begins at t_0 with an electron tunneling on the QD. Now there is definitely an electron on the QD and the time it remains on the QD is measured. Those time intervals are called t_{on} and they are distributed according to tunneling rate Γ_{off} (a detailed treatment can be found e.g. in [54]):

$$\rho_{on}(t_{on}) \propto e^{-\Gamma_{off} t_{on}}, \tag{4.7}$$

A high rate Γ_{off} implies short time intervals during which an electron remains on the dot. The same consideration is true for the t_{off} events, i.e. the measured time intervals during which the QD remains empty.

$$\rho_{off}(t_{off}) \propto e^{-\Gamma_{on} t_{off}} \tag{4.8}$$

[1]Note, that this semi-classical description with definite electron numbers is only valid for slow tunneling rates, as they are observed in the experiments described in this thesis.

A high Γ_{on} leads to short time intervals during which the QD remains empty. Consequently, one has to extract Γ_{off} from the distribution of t_{on} intervals, while the distribution of t_{off} intervals contains information about Γ_{on}.

In Addition one can determine the probability for an electron to reside on the QD from the extracted tunneling rates. By taking Equation 4.5 and assuming a steady state, i.e. $\dot{P}_{on} = 0$, one can show the relation

$$P_{on} = \frac{1}{1 + \frac{\Gamma_{off}}{\Gamma_{on}}} \tag{4.9}$$

to be valid. In the experiment Γ_{on} and Γ_{off} are functions of gate voltage, since the dot levels are shifted with respect to the chemical potential by varying V_g. By inserting the above relation into Equation 4.4 one obtains

$$\frac{\Gamma_{off}}{\Gamma_{on}} = \frac{1}{2} e^{\frac{-e\alpha_g V_g}{k_B T_e}}, \tag{4.10}$$

which can be further simplified to $\Gamma_{on} = 2\Gamma f(E)$, where $\Gamma_{off} = \Gamma(1 - f(E))$ is assumed. In other words, the tunneling rate Γ through the barrier is modulated with the density of unoccupied states in the leads, $(1 - f(E))$, and $E = -e\alpha_g V_g$. This assumption is justified if tunneling is elastic. (The factor of 2 for Γ_{on} describes an increased probability for tunneling on the QD, due to spin degeneracy)

After extracting the t_{on}- and t_{off} intervals from data sets such as the one depicted in Figure 4.1, one can histogram t_{on} and t_{off} and fit the exponential function from Equation 4.8 and Equation 4.7 to the data. An example is given in Figure 4.2, where the data is plotted on a logarithmic scale and the corresponding fits are lines instead of exponential functions, which improves automatic fitting. Here, the slopes of the fitted lines correspond to the tunneling rates Γ_{on} and Γ_{off}. Repeating this procedure for data sets taken at different points of an electron transition (see e.g. Figure 4.1), yields different on- and off rates, which can then be inserted into Equation 4.9 to compute the probabilities P_{on} and P_{off}. Figure 4.2 (c) shows an example for the resulting probability for an electron to be on the QD.

Automatically creating histograms of t_{on}- and t_{off} intervals might cause difficulties. The number and size of bins has to be chosen reasonably, in order to obtain statistically and physically meaningful histograms. Predefined algorithms of the used analysis software, which determine bin size and number of bins according to statistical considerations and number of data points, repeatedly caused problems. Manually implemented algorithms are capable of reducing these difficulties, but are no definite solution. This procedure also introduces a binning error in addition to the inevitable

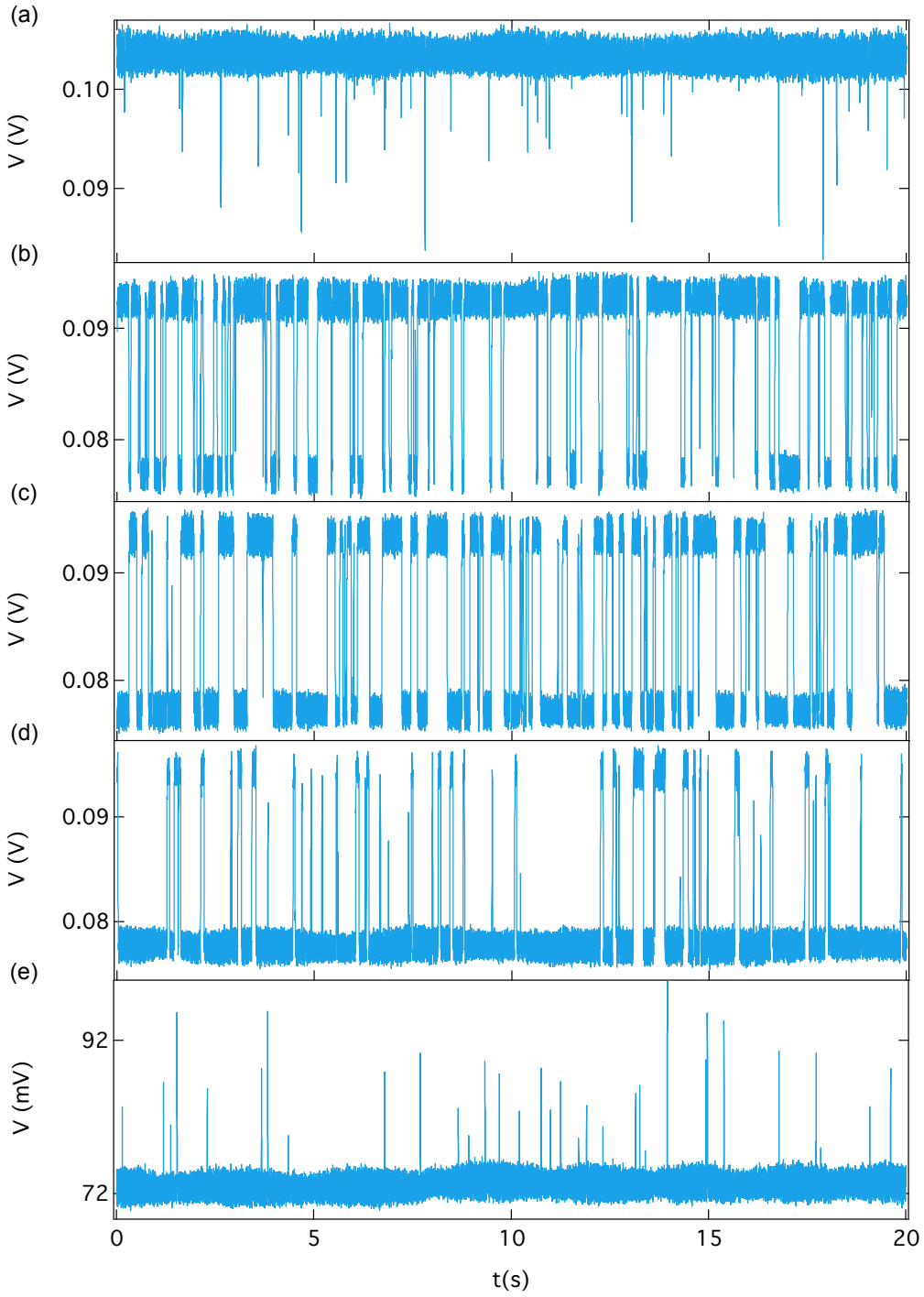

Figure 4.1.: (a)-(e) Real-time data, where the voltage across the charge sensor is measured against time at different points of an electron transition. The upper state corresponds to a QD occupied by one electron (t_{on} intervals), while the lower state corresponds to an empty QD (t_{off} intervals), which was derived from previous scans over the corresponding electron transition. In (a) the QD is occupied most of the time. Increasing the applied gate voltage shifts up the dot level with respect to the chemical potential in the leads, such that tunneling off becomes more likely (b) until resonant tunneling occurs (c). Further shifting the dot level, reverses the situation. Now, tunneling on the QD becomes less likely (d) until the QD is empty most off the time (e). Finally, the QD will be completely empty and tunneling events are no longer observed (Situation not depicted).

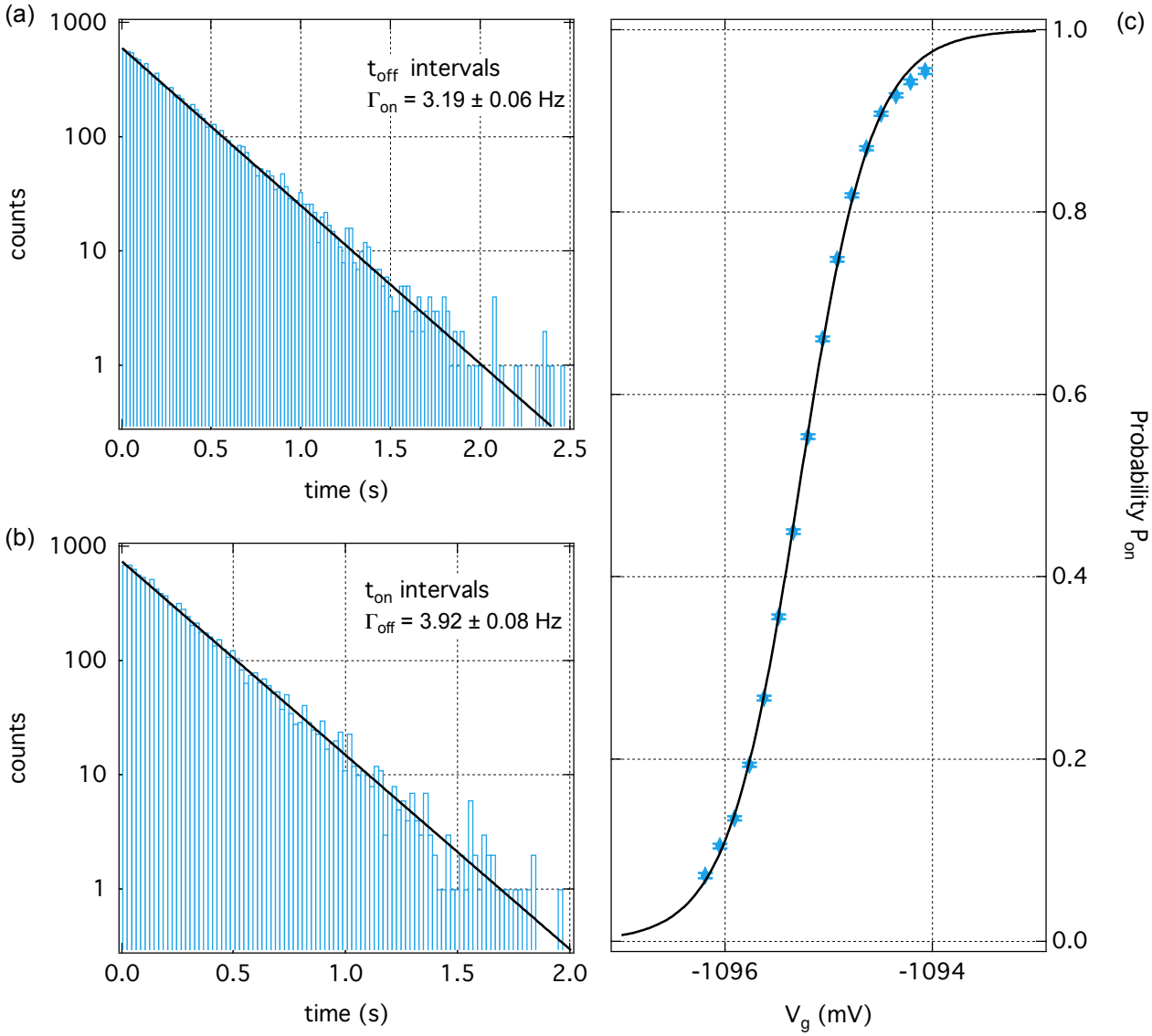

Figure 4.2.: (a), (b) t_{off} and t_{on} intervals extracted from real-time data (see Figure 4.1). Both histograms are plotted on a logarithmic scale and the linear fits correspond to Equation 4.8 and Equation 4.7. From the slopes of these linear fits, the according tunneling rates are extracted. (c) Repeating this procedure for different data sets, taken at different points of an electron transition (see Figure 4.1), leads to gate voltage dependent on- and off rates. Here, the extracted values for Γ_{on} and Γ_{off} are used to calculate P_{on} according to Equation 4.9 (blue data points). In this graph, a Fermi function (black line) is fitted to the P_{on} data. Fit and data are in good agreement and with a lever arm of $\alpha = 61.9\,\mu\text{eV/mV}$ an electron temperature of $T_e = 115\,\text{mK}$ is extracted. Small deviations between fit and data close to $P_{on} = 1$, respectively $P_{on} = 0$, are due to the limited bandwidth of the experimental setup and the reduced number of events, i.e. a increased statistical error, in this regions. All data was taken with zero bias across the QD.

statistical error. Especially analyzing data for measurements such as the one depicted in Figure 4.2 (c) is problematic, since here tunneling rates strongly depended on gate voltage. Hence, the distribution of t_{on}- and t_{off} intervals underlie strong changes as a function of gate voltage.

Even in cases where automatically creating histograms was successful, the corresponding automatic fits might cause additional problems. In general, fitting lines to logarithmic histograms is more stable than fitting exponential functions to the original data. But still, the resulting fits can be influenced strongly by a small number of events, which are much longer than the majority of detected events. Such events are statistically less likely, but especially for larger data sets taken during long measurement periods, they are still detected. A high number of such events also can hint towards a deviation from the exponential distribution, which might be caused by drifts or the presence of more than two possible electron states. But even if this is not the case, automatic fit routines tend to overestimate bins containing a low number of counts for data on a logarithmic scale (and bins containing a high number of counts for data plotted on a linear scale). This problem of the automatic fits, of course, can be reduced or even solved by performing weighted fits, where bins with higher numbers of counts are weighted stronger than bins with only a small number of counts. Alternatively, one also can introduce a cutoff, such that bins containing less the e.g. 10 events (corresponding to a statistical uncertainty of approximately 30%) are not considered for fitting. However, the effort required to suitably solve all these difficulties is considerable. Therefore, another possibility to extract tunneling rates from the measured time intervals was developed and tested. It turns out that Γ_{on} and Γ_{off} rates can be calculated directly from t_{on} and t_{off} intervals, hence eliminating the need for histogramming and fitting data. This completely eliminates binning and fitting errors, reducing uncertainties to statistical errors.

Consider a total measurement interval T. In case of resonant tunneling, there is one electron tunneling on and off the QD continuously, and the corresponding real-time measurement shows a telegraph-noise like signal (see Figure 4.1). Hence, the measurement interval T only consists of t_{on} and t_{off} intervals that are distributed according to the exponential function derived in Equation 4.8 and Equation 4.7:

$$T = T_{on} + T_{off} = N_{on} \langle t_{on} \rangle + N_{off} \langle t_{off} \rangle \tag{4.11}$$

In this equation N_{off} and N_{on} denote the number of events according to the underlying histogram (see e.g. Figure 4.2), while T_{on} and T_{off} are the total time an electron is on the dot or not, i.e. the sum of all t_{on}- and t_{off} intervals. Finally, $\langle t_{on} \rangle$ and $\langle t_{on} \rangle$ denote the average time on, respectively off the dot. In the continuous case, where binning

effects are not taken into account, these two expressions can be calculated by:

$$\langle t_{on} \rangle = \int_0^\infty dt\ e^{-\Gamma_{off} t} = \frac{1}{\Gamma_{off}}; \quad \langle t_{off} \rangle = \int_0^\infty dt\ e^{-\Gamma_{on} t} = \frac{1}{\Gamma_{on}} \tag{4.12}$$

On the other hand, these two expressions also can be determined by:

$$\langle t_{on} \rangle = \frac{2 \cdot T_{on}}{N_{total}}\ , \quad \langle t_{off} \rangle = \frac{2 \cdot T_{off}}{N_{total}} \tag{4.13}$$

Combining Equation 4.12 and Equation 4.13 leads to the results

$$\Gamma_{off} = \frac{N_{total}}{2 \cdot T_{on}}, \text{ and } \Gamma_{on} = \frac{N_{total}}{2 \cdot T_{off}} \tag{4.14}$$

By exploiting this relation, one can calculate the tunneling rate directly from the extracted t_{on}- and t_{off} intervals and thereby circumvent the difficulties that arise from the necessity to implement automatic histogramming and fitting procedures. Of course, the so calculated tunneling rates are only correct as long as the assumptions (i.e. only two available states, exponential distribution[2] of t_{on} and t_{off} intervals) made for the above derivation are valid. Only if the t_{on}- and t_{off} intervals follow the exponential distribution from Equation 4.11, or Equation 4.8 and Equation 4.7 respectively, this calculation is correct. However, the same assumption is made when histograming data and fitting exponential functions. The accuracy of extracting tunneling rates strongly depends on statistics, i.e. how many events were detected in the evaluated data set. For a total number N_{total} of switches the statistical uncertainty is given by $\sqrt{N_{total}}$. Consequently, the uncertainty in the extracted tunneling rate is given by $\Delta\Gamma_{on} = \frac{\sqrt{N_{total}}}{2T_{off}}$ (and equivalentely for $\Delta\Gamma_{off}$).

Good agreement is found between both analysis methods, as long as there are enough events detected, i.e. for sufficient statistics. The data shown in Figure 4.2 is such an example, as here fitting lines to the histograms gives $\Gamma_{on} = 3.19 \pm 0.06\,\text{Hz}$ and $\Gamma_{off} = 3.92 \pm 0.08\,\text{Hz}$, while calculating tunneling rates according to Equation 4.14 gives $\Gamma_{on} = 3.24 \pm 0.03\,\text{Hz}$ and $\Gamma_{off} = 3.99 \pm 0.04\,\text{Hz}$. The uncertainties for the fitted tunneling rates are originating from the fit routine only, while the additional uncertainty due to binning is not included.

4.2. Measuring Tunneling Rates

The previous section treats the mathematical and statistical basics required to determine tunneling rates from t_{on}- and t_{off} intervals extracted from real-time data.

[2]Here, a Poisson distribution is assumed for the tunneling events. In case succeeding events are independent, the exponential distributions are valid.

Independent of the procedure used to determine the actual tunneling rate, the algorithm used to extract t_{on}- and t_{off} has to work properly, otherwise all further analysis methods will give wrong results. Consequently, the algorithm used to extract t_{on}- and t_{off} has to be tested thoroughly. In this section, the method used to determine t_{on}- and t_{off} is described shortly, alongside the procedure used to test this method by creating artificial real-time data with predefined tunneling rates.

The software written to analyze real-time data and to extract t_{on}- and t_{off} intervals was designed under the premise of generality and high flexibility. Hence, a two-step trigger mechanism is implemented, that determines first, whether or not tunneling events are present in the input data and second, if the measured signal matches the given conditions of real-time tunneling events in the experiment. The first step of the trigger mechanism, determining the presence or absence of real-time tunneling events, relies on a data smoothing procedure (binomial/Gaussian smoothing). For every real-time trace the difference between maximum- and minimum voltage is calculated, $\Delta_{trig} = V_{max} - V_{min}$. In case the input signal contains only noise and no real-time tunneling events, smoothing data substantially reduces the difference Δ_{trig}. This is not the case for data sets containing tunneling events. Here, only the noise on top of the much slower real-time tunneling events averages out. Hence, the ration $\Delta_{trig}^{smooth}/\Delta_{trig}$ is small for data sets without tunneling events, while data sets containing tunneling events lead to a high ratio of 0.5 and above.

If the first step of the trigger has identified the presence of tunneling events in the input data, the second trigger step determines, whether or not the amplitude of the tunneling events is within a predefined window. This window has to be chosen according to the configuration and sensitivity of the charge sensor, in order to prevent triggering on exceptional high noise peaks and other false events. In general, this window can be chosen such that a very wide range of real-time tunneling events is correctly identified, while false events are ignored successfully. After a data set has passed the trigger stage and the presence of tunneling events has been detected, the actual evaluation procedure begins. The basic idea of this procedure is very simple, but also very effective. In a first step the data set is symmetrisized around zero by subtracting a value, which is calculated individually for every input by $(V_{max} + V_{min})/2$, where $V_{max/min}$ refers to the maximum and minimum of the input data. Now, the two levels of the telegraph-noise like input signal have different signs. The upper level lies above zero, while the lower level lies below zero. Consequently, the upper level corresponds to positive values, while the lower level corresponds to negative values, and every tunneling events requires a change of sign. This situation is illustrated in Figure 4.3, where the analysis of an exemplary data trace is depicted, including several intermediate steps. The evaluation procedure now identifies every zero crossing of the data set, since they correspond to

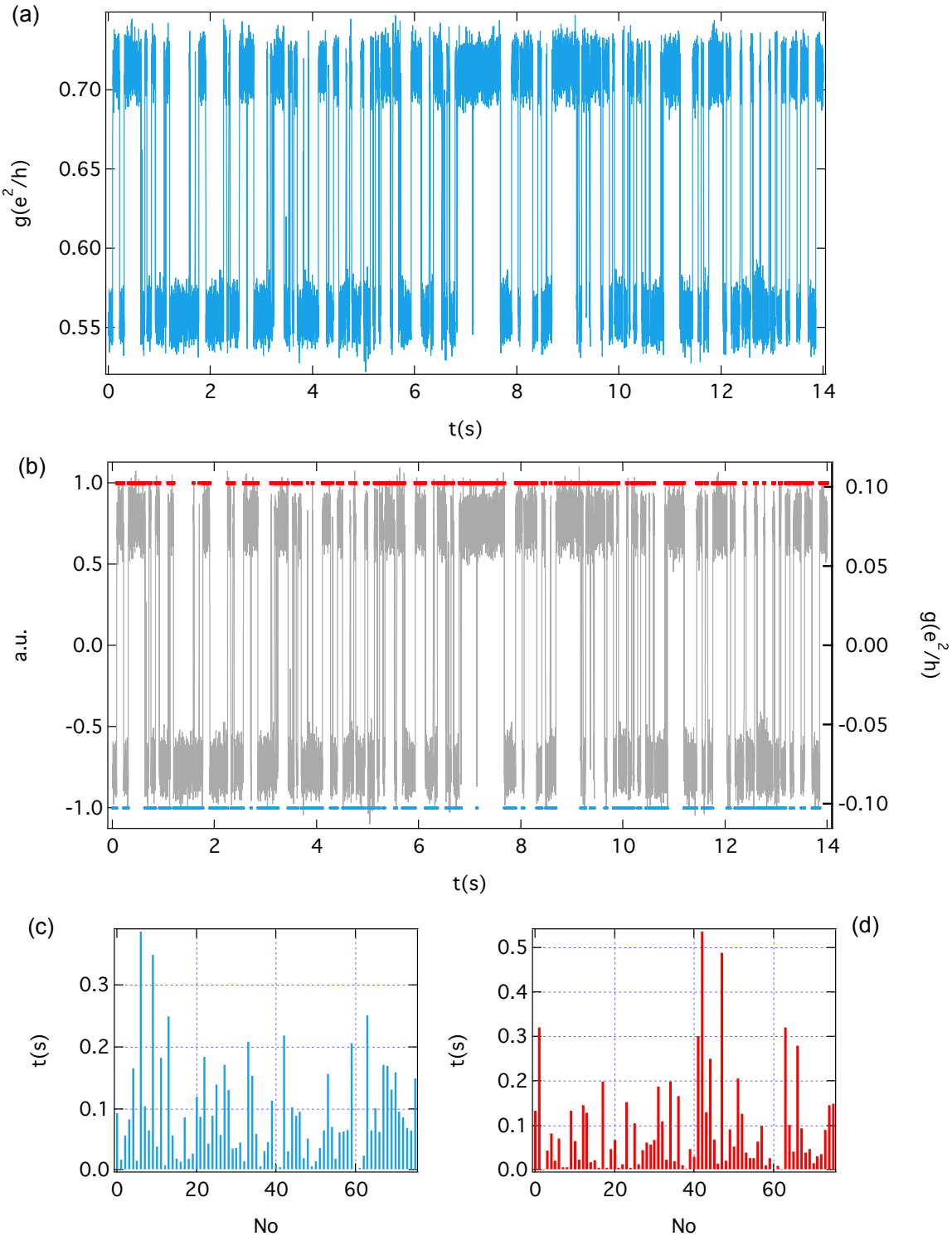

Figure 4.3.: Illustration of the evaluation procedure used to extract t_{on}- and t_{off} intervals from real-time data. (a) Exemplary real-time data trace, where resonant tunneling in the QD is detected as a function of time by the charge sensor. (b) After the two-step trigger stage has successfully identified the presence of tunneling events in the data set, the signal is made symmetric around zero (gray data). By determining all zero crossings of the signal and calculating the distance of succeeding events, it is possible to receive all time intervals an electron remained in the upper level (red) and in the lower level (blue). (c)+(d) The two classes of time intervals can be identified with the t_{on}- (red) and t_{off} intervals (blue).

the actual tunneling events in the data set. In addition, the algorithm checks, whether the first point of the data set was positive or negative, i.e. if the data set starts with an electron in the upper- or in the lower state. Now, all time intervals, during which an electron was in the lower- or the upper level can be calculated simply from the distance of succeeding roots in the input signal. From previous measurements on the QD it is possible to determine whether the upper level corresponds to an electron on the QD or an empty dot and vice versa. Thereby, one can identify the two classes of extracted time intervals with the t_{on}- and t_{off} intervals. Finally, both sets of output data are stored for further analysis, such as e.g. calculation of the corresponding tunneling rates.

Every evaluation algorithms hast to be tested carefully, before the resulting output data is analyzed any further. Since the main objective of this analysis procedure was to determine tunneling rates from the extracted t_{on}- and t_{off} intervals, the most reasonable test is to feed the program real-time data with known tunneling rates and compare the results obtained from the evaluations procedure with the correct values. Since experimental data with known tunneling rates was not available, an additional program was written, which creates artificial real-time data with predefined, adjustable tunneling rates. In addition, this software is able to create artificial real-time data with different signal-to-noise ratio (SNR) and with an adjustable rise-time, in order to explore the effects of bandwidth limitations on data evaluation. Figure 4.4 shows an example of such artificially created data sets. The program creates random fluctuations between two levels that are separated by a predefined amplitude and with time intervals distributed according to Equation 4.8 and Equation 4.7. The amplitude is fixed within every artificially created data set, but can be adjusted prior to running the program, in order to match the actual charge sensor signal (see Figure 4.4 (a)). In addition, Gaussian distributed noise is added to the artificial data set (see Figure 4.4 (b)). The amplitude of the Gaussian noise also can be adjusted in order to simulate different values of the signal-to-noise ratio. Figure 4.4 (b) depicts artificial data with a SNR of $\Delta_{SNR} = 8$, while in Figure 4.4 (c) the SNR was reduced to $\Delta_{SNR} = 2$. By introducing an additional time constant τ in the creation of artificial real-time data, one can simulate the influence of a limited bandwidth on the real-time data in general, and especially on the evaluation procedure. Hence, it is possible to determine how fast real tunneling events can be, i.e. how fast one can measure on the experimental setup, before the limited bandwidth is dominating the real-time data and renders data analysis impossible. Figure 4.4 (d) demonstrates the effect of a limited bandwidth on the artificially created data. Here, a rise time of $\tau = 2\,\text{ms}$ was chosen. In comparison with Figure 4.4 (a) and (b), where a rise time of $\tau = 0.1\,\text{ms}$ was set, the influence of this additional time constant on the tunneling data is obvious.

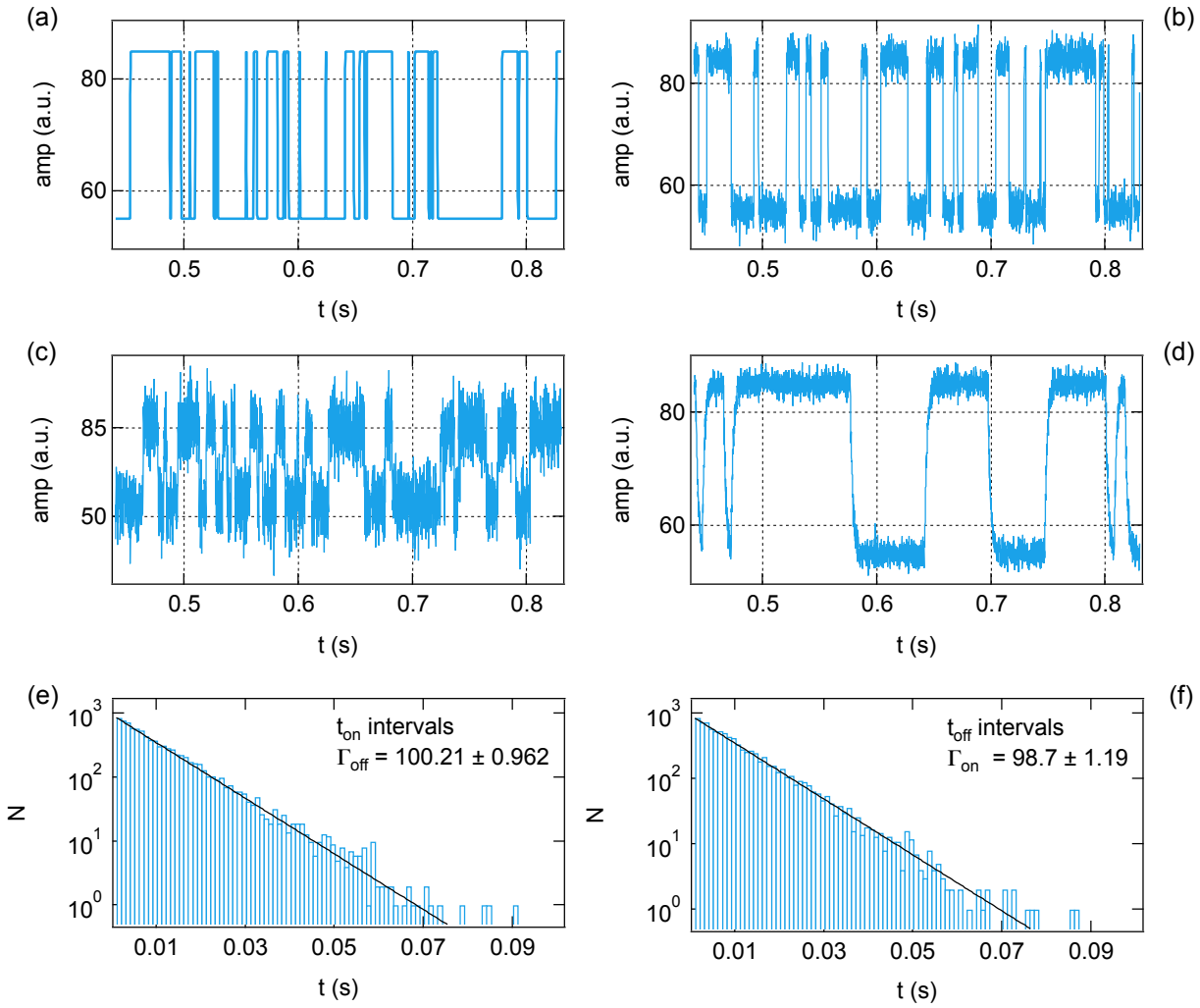

Figure 4.4.: Illustration of artificial real-time data creation. (a) In a first step, random fluctuations between two levels are created to simulate resonant tunneling. The time intervals in the upper and lower state are distributed according to Equation 4.8 and Equation 4.7. (b) In addition, Gaussian distributed noise is added to the signal, here with a signal-to-noise ratio of $\Delta_{SNR} = 8$. (c) Reducing SNR to $\Delta_{SNR} = 2$ leads to artificial real-time data that barely can be processed by the evaluation procedure anymore. (d) By adding an additional rise time to the procedure, it is possible to explore the influence of a limited bandwidth on data evaluation. (e)+(f) Exemplary test results of the evaluation procedure, as discussed in the main text.

With the help of this program, one finds a signal-to-noise ratio of $\Delta_{SNR} = 2$ and higher to be sufficient for data analysis. Lower values of SNR lead to event miss-identification and hence to false results of the evaluation software. Additionally, one can conclude, that the experimentally accessible rise-times of $\tau = 0.1 - 0.03\,\mathrm{ms}$ of the real-time setup do not have influence on data analysis (for tunneling rates below $1 - 5\,\mathrm{kHz}$). Hence, data analysis is limited by the SNR, not by the bandwidth of the experimental setup. Figure 4.4 (e) and (f) show histograms obtained from evaluating artificial real-time data with symmetric tunneling rate of $\Gamma_{on} = \Gamma_{off} = 100\,\mathrm{Hz}$. Determining the tunneling rates with the evaluation procedure gives $\Gamma_{off} = 100.2 \pm 1\,\mathrm{Hz}$ and $\Gamma_{on} = 98.7 \pm 1.2\,\mathrm{Hz}$ (As stated above, the errors of the calculated rates are statistical errors determined from the number of detected events N_{total}). Extensive tests for a wide range of different parameters, such as tunneling rates, SNR and rise time, proof the correct functionality of the evaluation procedure, especially for experimentally accessible parameter values. In addition, it is possible to explore the borders of parameter space, where the evaluation routine starts to fail and correct data analysis is no longer possible.

4.3. Active Drift Compensation

Many experiments described in this thesis, require large amounts of data in order to obtain sufficient statistics to allow for further analysis with the necessary precision. Hence, long measurement periods on the timescale of several hours up to two days are not uncommon. Those long measurements are not possible without additional feedback and correction mechanisms, that compensate for small drifts in the QD, as well as the charge sensor. In this section, a two step active feedback and drift correction mechanism is described, capable of stabilizing the energy levels in the QD and the sensor quantum dot with the necessary precision and on the required timescales.

Because of the background charge fluctuations of the wafer material (see also chapter 3), the energy levels of the QD and the SQD fluctuate over time [26, 54]. Due to drifts of the amplifier[3], which manifest itself in a variable DC offset, there might also be drifts in the SQD. While the first kind of fluctuations are fundamental and are expected to average out over long times, the second kind of drift is of technical nature and does not necessarily cancel out over time. However, even small fluctuations in the QD have considerable influence on e.g. the tunneling rate on and off the QD. Hence, any measurement of tunneling rates is influenced strongly by such fluctuations, or even

[3]The drift of the amplifier/I-V converter, which is about $\pm 2\,\mu\mathrm{V}$ per hour, is dominating over the drift of the LNHR DAC, which is about $\pm 10\,\mu\mathrm{V}$ over period of eight hours and for a constant temperature of 25 °C. Here one has to take into account that the drift of the LNHR DAC is further reduced by the lever arm α between depletion gates and 2DEG.

rendered impossible. Drift in the SQD and charge sensor setup manifests itself in a shift of the measured Coulomb peak. As a consequence, the operation point of the charge sensor (see chapter 3) is not fixed, which might lead to massive change in the SQD sensitivity.

To compensate for shifts in the QD, an active feedback mechanism is applied, similar to the one described by Amasha *et al.* [54]. This feedback mechanism relies on measuring the Γ_{off} rate in the exponential tail of the Fermi function. From previous considerations, one can assume the off-tunneling rate to be given by $\Gamma_{off} = \Gamma(1-f(x))$, where $f(x)$ is the Fermi function and x a parameter describing the energy as a function of gate voltage and temperature. As can be seen from Figure 4.5, this function can be approximated by an exponential, $\Gamma_{off} \approx \Gamma e^{-e\alpha_g V_g/k_B T_e}$. In the region, where this approximation is valid, Γ_{off} is exponentially sensitive to changes of $-e\alpha_g V_g/k_B T$, i.e. to shifts in the energy levels of the QD. This exponential sensitivity is exploited for the feedback mechanism, which stabilizes the QD energy levels by regularly measuring Γ_{off}.

At the beginning of every measurement period, one has to determine a set-point, where Γ_{off} takes one a certain value, e.g. 20 Hz and lies in the exponentially sensitive region. Further, one has to chose a tolerance threshold, within which Γ_{off}, i.e. the energy level of the QD, is allowed to fluctuate. In the experiments described here, this threshold was typically chosen to be $\Gamma_{tol} = 2.5$ Hz. The active feed back mechanism now regularly checks, whether or not the deviation of the measured Γ_{off} rate is larger than the tolerance threshold. The chosen measurement time t_{fb} for which the actual tunneling rate is determined, has to be chosen such that the statistical error is much smaller than the tolerance threshold, otherwise the compensation mechanism can not function properly. In order to chose a long enough measurement interval, the estimate $t_{fb} \geq \Gamma_{off}^{set}/\Gamma_{tol}^2$ is applied [54]. In case the tolerance is exceeded, the feed back mechanism automatically calculates the necessary gate voltage corrections that are required to regulate Γ_{off} back to the tolerated range. Figure 4.5 depicts Γ_{off} on a logarithmic scale, where the exponential part of the Fermi function becomes linear. The slope of the linear part is given by $-e\alpha_g V_g/k_B T_e$ and hence depends on electron temperature and the lever arm α_g. Both parameters have to be known for the implementation of the active feed back mechanism.

The compensation in gate voltage, carried out by the feedback mechanism, is recorded in order to control its functionality. Thereby, it is also possible to learn more about the nature of the compensated fluctuations. In Figure 4.6 (c) an example of the automatic corrections, made by the feedback mechanism, is displayed. Here, positive and

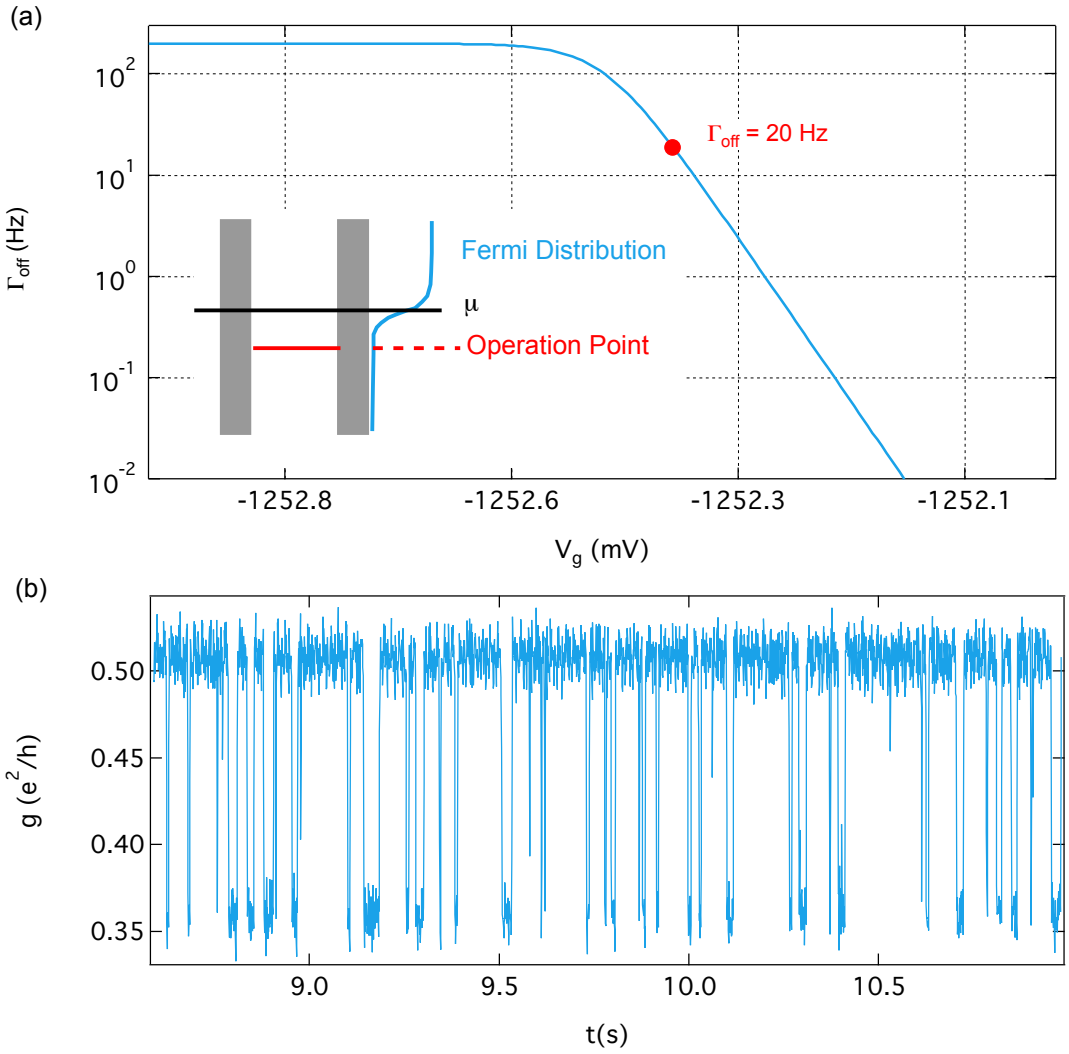

Figure 4.5.: Active feed back mechanism used to stabilize the energy levels in the QD. (a) Γ_{off} as a function of V_g on a logarithmic scale. For the active feed back system, one has to choose a set-point, e.g. $\Gamma_{off} = 20\,\text{Hz}$ in the linear region (in log-scale). If the regularly measured deviations of Γ_{off} exceed the tolerance (e.g. 2.5 Hz), the active feedback automatically calculates the required change of V_g in order to regulate Γ_{off} back to the set-point. The inset depicts the according energy level diagram. (b) A measurement of the active feedback system, which corresponds to a set-point of 20 Hz. The length of such a measurement has to be chosen such that the according error is smaller than the tolerance threshold, $t_{fb} \geq \Gamma_{off}^{set}/\Gamma_{tol}^2$ [54].

negative compensations are canceling each other out[4], i.e. the sum of all corrections made is zero. This behavior is expected for the aforementioned background charge fluctuations in the heterostructure. Of course, this compensation mechanism is only capable to compensate for fluctuations on the time scale of two succeeding compensation cycles[5]. Faster fluctuations still potentially disturb measurements, but for more frequent compensation cycles, one finds the fluctuations usually to be within the predefined tolerance threshold. Hence, reducing the tolerance would be necessary, which on the other hand would require longer measurement periods for the compensation mechanism and thereby would reduce the actual data gathering periods even further. Since QD stability resulting from compensation cycles once every fifteen minutes is sufficient for the experiments performed for this thesis, increasing the compensation interval was not necessary. Since one compensation cycle takes between 15 s and 60 s, approximately 2 - 7% of the overall measurement time are required for this procedure. Of course, the situations can be different for other kind of experiments [42].

The second kind of compensation mechanism implemented here, aims at stabilizing the sensor quantum dot. An approach similar to the QD feed back mechanism is implemented, where the part around the operation point of the charge sensor is approximated linearly. In Figure 4.6 (a) a measurement of a Coulomb peak in the sensor quantum dots is depicted, alongside the according operation point and the linear fit used to approximate the area around the operation point.

The explanation why the area around the operation point is linearly approximated, instead of fitting the full functional dependency of the according Coulomb peak is, that due to the already implemented sensor feed back (Appendix B), which compensates for the capacitive coupling between QD and SQD, the sensor is expected to fluctuate only within a small range around the operation point. The advantage of this procedure is the simplified calculation of the according sensor compensation, while the main disadvantage is, that in case of larger jumps and drifts in the SQD, the sensor drift compensation might fail. Since such events a rare, the simpler but faster sensor compensation mechanism was applied.

Before every measurement period, the sensor has to be set manually to its operation point and for every run of the sensor drift compensation, the procedure automatically determines whether or not the occurred drift lies within the defined tolerance, by measuring the average sensor conductance over fives seconds. Independent

[4]The data shown here, correspond to a measurement period of twelve hours. Since sometimes more than one compensation step is required to tune Γ_{off} back to the set-point, the number of data points here is not directly related to the number of measurement cycles of the actual experiment.

[5]Usually, the time between two succeeding runs of the active feed back mechanism was fifteen to twenty minutes.

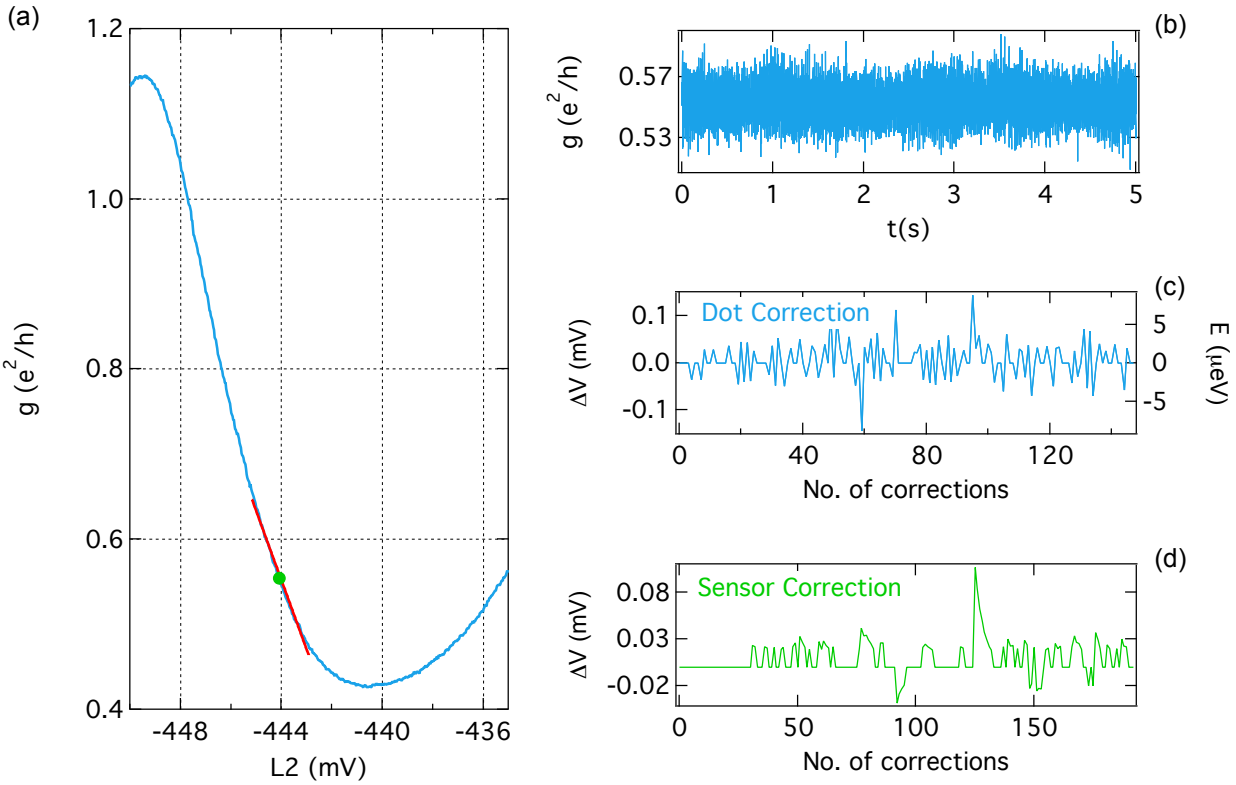

Figure 4.6.: SQD drift compensation: (a) Measured Coulomb peak (blue line), where the according operation point is marked green. The slope of the linear fit (red) around the operation point is used to calculate the necessary gate voltage compensation, whenever the deviation between operation point and measured sensor conductance exceeds the tolerance. (b) Exemplary measurement used to determine the actual average sensor conductance. (c) Recorded QD compensations, as discussed in the main text. (d) Sensor dot compensations analogue to (c) see discussion in the main text.

of the actual operation point of the SQD, the tolerance was set to $g_{tol} = 0.01\,e^2/h$. If $|(g_{op} - g_{meas})| \geq g_{tol}$ the slope of the linear fit around the operation point can be used to calculate the required correction for the voltage on the SQD plunger gate.

Figure 4.6 (d) depicts the sensor dot compensation operations carried out parallel to the QD feed back operations in Figure 4.6 (c), i.e. for the same measurement period of twelve hours. In contrast to the data of Figure 4.6 (c), the sum of all compensation operations is not zero. Hence, one can conclude that the background charge fluctuations are not the main drift and fluctuation mechanism in the SQD system, although they very likely contribute, since the SQD is part of the same wafer material. Instead, the amplifier in the SQD system probably produces the dominating source of drifts. Since amplifier drifts like this are a function of temperature and other experimentally not accessible parameters, this assumption can not be proved easily. However, independent of the responsible drift mechanism, the senor drift compensation is capable of stabilizing the charge sensor withing the requested range of parameters. The two compensation mechanisms cannot be executed in parallel. Instead, they are executed serial, with the sensor drift compensation applied prior to the QD drift compensation. The order of execution is important, since both compensation mechanisms interfere with each other. Applying the SQD compensation algorithm after the QD compensation algorithm will shift the energy level in the QD and thereby eventually undo the compensations made before. On the other hand, the QD compensation algorithm also influences the SQD, but here this parasitic effect can be tolerated and does not influence the measurement results.

4.4. Tunneling in the Presence of a Magnetic Field

All experiments discussed so far were performed in the absence of external magnetic fields. In order to investigate spin related effects in GaAs quantum dots, one inevitably has to lift spin degeneracy by applying external magnetic fields. As described in chapter 2, external magnetic fields are always applied in-plane of the sample, in order to prevent additional quantization effects, e.g. Landau quantization. Tunneling in the presence of external magnetic fields has been studied in other works before, in GaAs system [27, 54, 59, 104, 105], as well as in other materials [106, 107].

This section describes experiments, where real-time charge sensing is used to resolve the Zeeman splitting in a QD, induced by an external magnetic field applied in-plane. Such measurements are required to determine the electron g-factor of the QD system and in order to calibrate the read-out stage of the pulsing scheme used to perform spin-relaxation time measurements, as they are described in chapter 7 (Ionization in the first step and loading in the second step).

In all these experiments, the tunneling rate Γ_{on} into an empty quantum dot is measured by applying the exact same two-step pulsing scheme, that already is described in chapter 2 (Ionization in the first and loading in the second step). The quantum dot is connected to two individual electron reservoirs (see Figure 2.2). One of the tunneling barriers is made very high such that tunneling through this barrier is negligible. Since in the experiments here, the left sensor dot is used, the right barrier was closed by increasing the voltage on gate wr (see Figure 2.2). Hence, electrons only tunnel on and off the QD through the left barrier, which is closer to the charge sensor and leads to a slightly improved sensitivity due to small shifts of the dot position. The two-step pulsing scheme is applied to gate p3, while the same pulse but with opposite sign and different amplitude is applied in parallel to the plunger gate L2 of the left SQD. This additional pulse is required to compensate for the capacitive coupling between L2 and p3, otherwise pulses applied to p3 would drive the SQD away from the adjusted operation point. The pulsing setup and the associated compensation pulses applied to the SQD plunger gate, are described in more detail in Appendix B. The two-step pulsing scheme ensures, that the QD is ionized completely during the first step, i.e. there are no electrons residing on the QD, while the second step is lowering the ground spin-state of the QD below the chemical potential in the left electron reservoir. Hence, the ground state is now accessible and an electron tunnels on the QD. By increasing the amplitude of the second step of the pulsing scheme, the excited spin-state eventually also lies below the chemical potential. Now, tunneling into both spin-states is possible and consequently one expects Γ_{on} to increase.

Figure 4.7 shows experimental data, which was obtained with this procedure. After the empty QD enters the load stage, i.e. the second part of the pulsing scheme is reached, it takes a time t_l until an electron tunnels on the QD (see Figure 4.7). By repeating the pulsing scheme numerously[6], the statistical basis becomes large enough for further analysis. The time intervals t_l are extracted from these data sets and either a histogram is made to determine Γ_{on}, or the tunneling rate is directly calculated according to Equation 4.14. Figure 4.7 (b) depicts an example of such a histogram. Extracting Γ_{on} in this way and for different settings of the pulse amplitude, i.e. for different positions of the energy levels in the QD with respect to the chemical potential, leads to graphs like those in Figure 4.8. Here, Γ_{on} is plotted as a function of gate voltage p3 and for different magnetic fields, i.e. for different Zeeman splittings.

The data in Figure 4.8 (a) was measured at a magnetic field of $B = 3\,\mathrm{T}$. Here, one can clearly distinguish the onset of a second step in the data, which corresponds

[6]Usually, one such measurement consists of up to 100000 repetitions of this pulsing scheme for each individual data point. In this context an individual data point means a different value of the amplitude in the second part of the pulsing scheme and hence a different position of the energy levels in the QD with respect to the chemical potential.

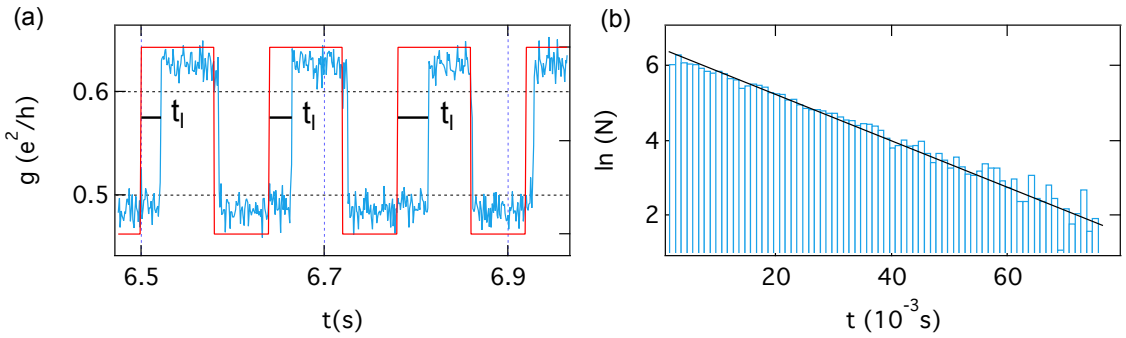

Figure 4.7.: Experimental data as it is used to determine Γ_{on} and the according Zeeman splitting (a) Exemplary real-time trace (blue) including four pulse cycles, as indicated by the overlaid pulsing scheme (red). The lower state corresponds to a ionized QD, while in the upper state there is one electron in the QD. The t_l-intervals are the time that passes between the system is pulsed into the load stage and the actual time an electron tunnels on the dot (black lines). (b) Numerous repetitions of this measurement scheme provide enough data to determine Γ_{on} by creating histograms (blue) and fitting lines (black) to the data (fit is done over full data range). Alternatively, Γ_{on} can also be calculated directly from Equation 4.14.

to the excited spin-state. For lower fields this feature could not be observed. The Zeeman splitting gets more distinct for higher fields of up to $B = 11\,\mathrm{T}$ (Figure 4.8). As expected, the splitting increases with increasing magnetic field . The data in Figure 4.8 exhibits another interesting feature, which has been observed and studied before [54, 108, 109] - spin dependent tunneling. Naively, one would expect Γ_{on} to be twice as high whenever ground spin-state and excited spin-state both are available. However, the data in Figure 4.8 shows a different behavior. Following Amasha *et al.* [54, 108], the data in Figure 4.8 is modeled with the function

$$\Gamma_{on} = \Gamma \cdot e^{-\beta_g V_g} \cdot \Big[f(V_g) + \chi f(V_g + \Delta V_g) \Big], \tag{4.15}$$

where $f(V_g)$ and $f(V_g + \Delta V_g)$ are Fermi functions centered around the positions of the ground- and excited spin-state, and the exponential function takes into account the energy dependence of Γ_{on} [74]. Γ is the bare tunneling rate through the respective barrier and the newly introduced factor χ describes the relative visibility of the excited spin-state with respect to the ground spin-state. For pulses driving ground- and excited spin state below the chemical potential, $f(V_g) \approx f(V_g + \Delta V_g) \approx 1$, hence $\chi = \Gamma_{on,e}/\Gamma_{on,g}$. Equation 4.15 is fitted to the experimental data in Figure 4.8 (red lines) and the relative visibility χ is extracted (see Figure 4.9). As stressed above, from a naive point of view one would expect $\chi = 1$, independent of magnetic field. However, this is not the case for the visibility extracted from the experiment, where χ takes one values between 1.0 at $B = 3\,\mathrm{T}$ and 0.3 at $B = 11\,\mathrm{T}$. Figure 4.9 shows,

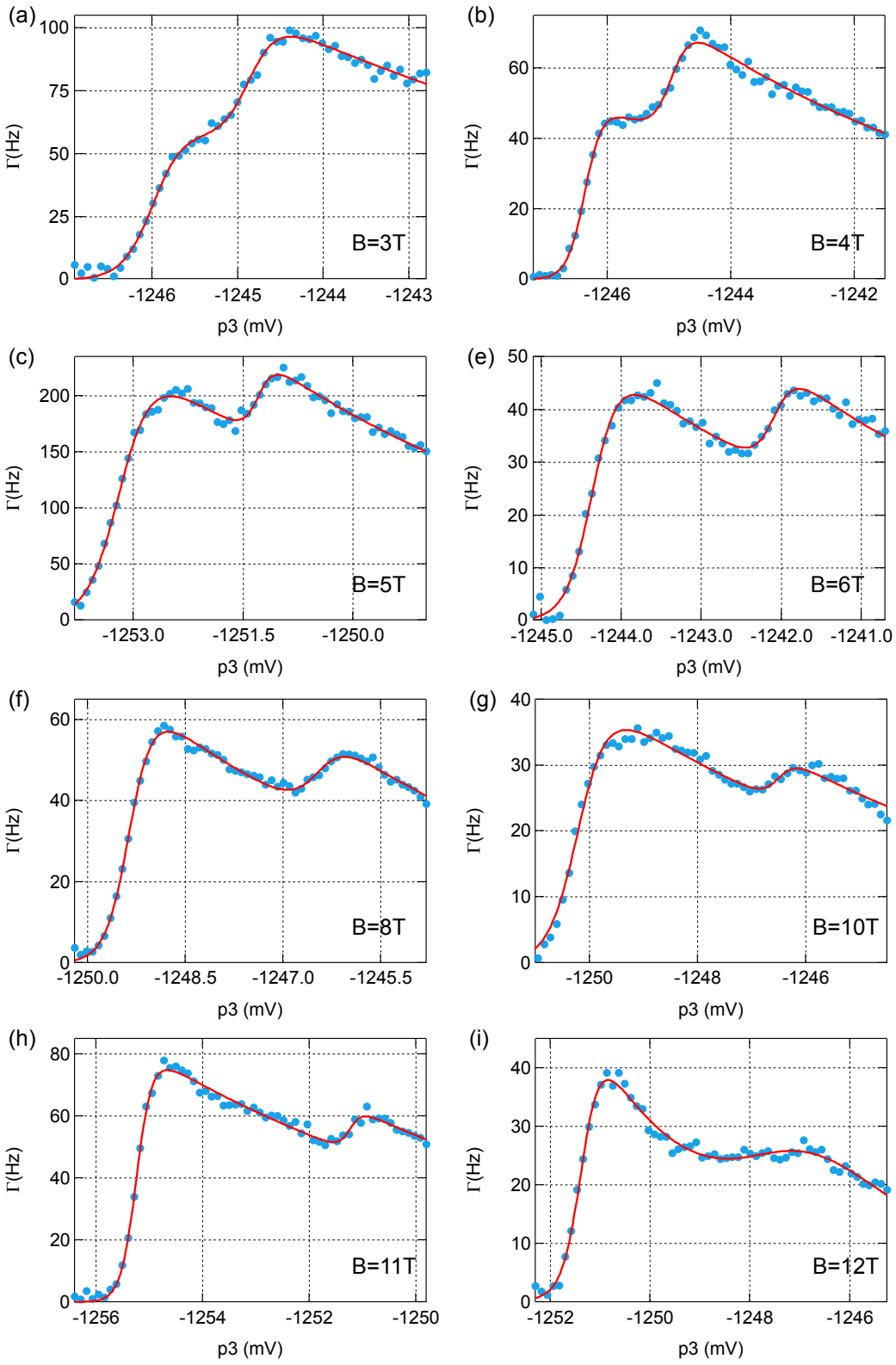

Figure 4.8.: (a)-(i) Γ_{on} (blue makers) as a function of gate voltage and for magnetic fields between B=3 T and B=12 T as indicated. For lower magnetic fields the Zeeman splitting cannot be resolved because of thermal broadening, i.e. $k_B T_e \approx E_Z$. For higher magnetic fields the visibility χ is to small. Red lines correspond to fits, as discussed in the main text. All data was take with B pointing in the direction 45 ° between the $[01\bar{1}]$ and [011] direction (in-plane).

that the visibility tends to decrease with increasing magnetic field, which is consistent with the observations made in [54, 108]. In the work of Amasha *et al.* this effect was empirically related to the shape of the investigated quantum dot and hence to the angular wave function of the electron in the dot. This issue was also addressed from the side of theoretical physics [109]. But the considerations made there are only able to explain the observed effect qualitatively but not quantitatively. Therefore, it is still unclear why tunneling into the excited spin state seems to be suppressed for higher magnetic fields and χ becomes smaller than one. Due to the lack of a theory,

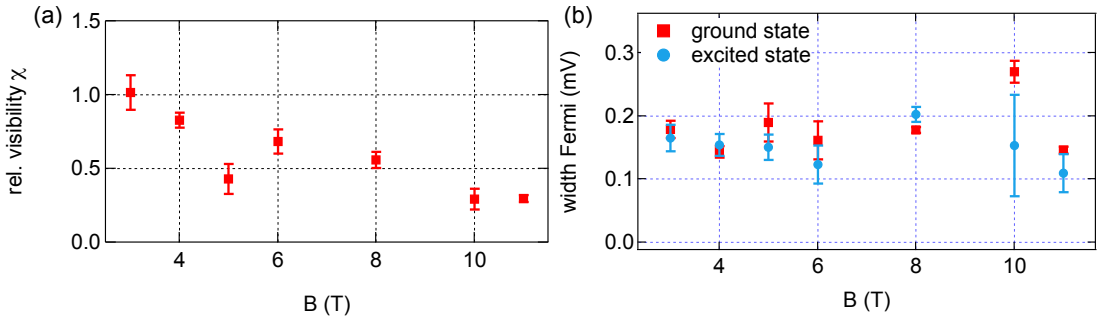

Figure 4.9.: (a) Visibility χ extracted from fits to the data in Figure 4.8. Here, χ tends to decrease with increasing field, in contrast to the naive expectation that $\chi = 1$, independent of magnetic field. For higher magnetic field the visibility takes on values smaller than one, which can be interpreted as suppressed tunneling into the excited spin state. For magnetic fields of $B = 4\,\mathrm{T}$ an below, one observes $\chi \approx 1$. (b) Width of the Fermi function fitted to the ground spin-state and the excited spin-state. Since this width is proportional to electron temperature in the system, one expects the same width for both states. The expected behavior is observed for low magnetic field, but for magnetic fields of 8 T and above, there are discrepancies between both values. The deviations observed here, might be explained by less good fit results at high magnetic fields.

these observations are not yet fully understood and should be investigated further in future experiments. It would be of special interest to investigate, whether or not the observed effect shows a angle dependence, i.e. if rotating the sample with respect to the magnetic field has influence on χ. Measuring an angle dependence could be an evidence for the involvement of spin-orbit interaction in this effect. Additional or improved theoretical models would be very helpful to understand this observation as well.

By varying the applied magnetic field, the Zeeman splitting, $|g|\mu_B B$, is varying accordingly. Consequently, one expects the Zeeman splitting, extracted from the experimental data, to be a linear function of magnetic field, with a slope proportional to the g-factor. Figure 4.10 displays experimentally determined Zeeman splittings, extracted from Figure 4.8. A linear fit to this data set gives $|g| = 0.39 \pm 0.014$, which is in good agreement with other measurements made on the same or similar material [54].

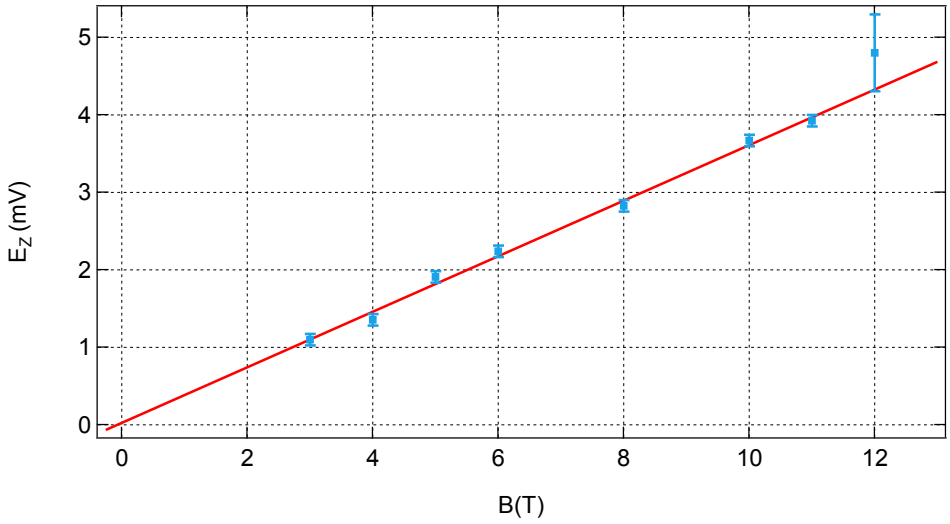

Figure 4.10.: Zeeman splitting as a function of magnetic field, extracted from the data in Figure 4.8. The data shows an excellent linear behavior, as expected, and extracting the g-factor from this measurement gives $|g| = 0.39 \pm 0.014$. Due to the small visibility at large fields, the data point at $B = 12\,\mathrm{T}$ is subject to a large error. Hence, the Zeeman splitting extracted at $B = 12\,\mathrm{T}$ was not taken into account for the linear fit shown here.

The lever arm used to calculate the g-factor is $\alpha_{p3} = 61.9\,\mu\mathrm{eV/mV}$. The exact procedure use to extract this lever arm is describe in Appendix B. Knowing the g-factor is essential for calibrating the pulsing scheme required for spin-relaxation time measurements. For this pulsing scheme the read-out stage has to be positioned precisely such that the excited state lies above the chemical potential, while the ground state lies still below the chemical potential. To adjust the read-out stage correctly, one has to convert the measured Zeeman splitting in to a gate voltage ΔV_p, which defines the amplitude of the pulse that drives the dot into the read-out stage. Hence, evaluating the above data and extracting the g-factor is a mandatory step towards implementing this pulsing scheme, which is discussed in detail in chapter 7, alongside the experimental implementation and the physical background of spin-relaxation time measurements.

Chapter 5

Thermally-Activated Charge Fluctuations in a GaAs Few Electron Double Quantum Dot

Daniel E. F. Biesinger, Christian P. Scheller, Dominik M. Zumbühl
University of Basel, Klingelbergstrasse 82, CH-4056 Basel, Switzerland

Bernd Braunecker
SUPA, School of Physics and Astronomy, University of St Andrews, St Andrews, UK

J. Zimmerman, A.C. Gossard
Materials Department, University of California, Santa Barbara, California, USA

Abstract

We investigate a laterally defined few electron double quantum dot in the limit of very low tunnel rates. We observe a sharply defined diamond shaped region centered between two associated triple points of the charge stability diagram. Within this region a nearby real-time charge sensor detects metastable charge state switching, indicating a change in the double dots electron configuration. The switching frequency can be controlled by gate tuning and shows a pronounced temperature dependence. We identify the effect as thermally activated charge fluctuations and provide an extension of the canonical theory of double quantum dots to capture this dynamical effect.

This chapter is in preparation for publication

5.1. Motivation

Quantum dots are a promising approach to implement qubits, the building blocks of a quantum computer, in solid state systems [16]. Numerous sophisticated experiments have by now demonstrated the successful implementation, control, and single-shot readout of electron spin qubits in GaAs quantum dots [20, 23, 37, 38, 47, 110]. To make further progress, the full control of the electron spin dynamics is crucial. The latter is characterized by two time scales, the relaxation time T_1 and the coherence time T_2. Since energy relaxation inevitably destroys coherent spin states, T_1 always sets an upper limit for T_2, $2T_1 > T_2$ [28, 32]. Yet usually T_2 is much shorter than its theoretical maximum, mainly due to the interaction of the electron spin with the Overhauser field created by the nuclear spins of the host material. This effect has been mitigated in recent experiments by applying spin-echo techniques, and T_2 times up to $200\,\mu$s were achieved [39], reaching close to T_1. A further understanding of how to control the mechanisms limiting T_1 becomes therefore necessary.

5.2. Experimental Observations

In this work we report real-time observations of thermally activated charge fluctuations in a double quantum dot (DQD). These fluctuations appear in a diamond shaped region centered between two associated triple points of the charge stability diagram (CSD), with the charge transition line as short diagonal. By tuning to very low tunnel rates and to electron temperatures $T_e = 50$-$60\,$mK we resolve single electron switching events by a nearby real-time charge sensor. We identify the observations as thermally activated charge fluctuations between metastable states and provide a dynamical extension of the canonical theory of DQDs. As this process persists at higher tunnel rates, we can provide by its time scale an upper limit to T_1 within the diamond shaped region.

5.3. Device Fabrication

Our samples are fabricated on a $Al_{0.3}Ga_{0.7}As$/GaAs heterostructure, which incorporates a 2D electron gas 110 nm below the surface of the wafer with a density $n = 2.6 \cdot 10^{11}\,\mathrm{cm}^{-2}$ and a mobility $\mu = 4 \cdot 10^5\,\mathrm{cm}^2/\mathrm{Vs}$. Ti/Au surface depletion gates as shown in Fig. 5.1 (a) are used to form and control the nanostructure. The two quantum dots adjacent to the DQD are used as real-time charge sensors, allowing single-shot charge readout with a minimal rise time of $6\,\mu$s and sensitivities as large as $\delta g/g \sim 1$ per electron [24, 43, 111].

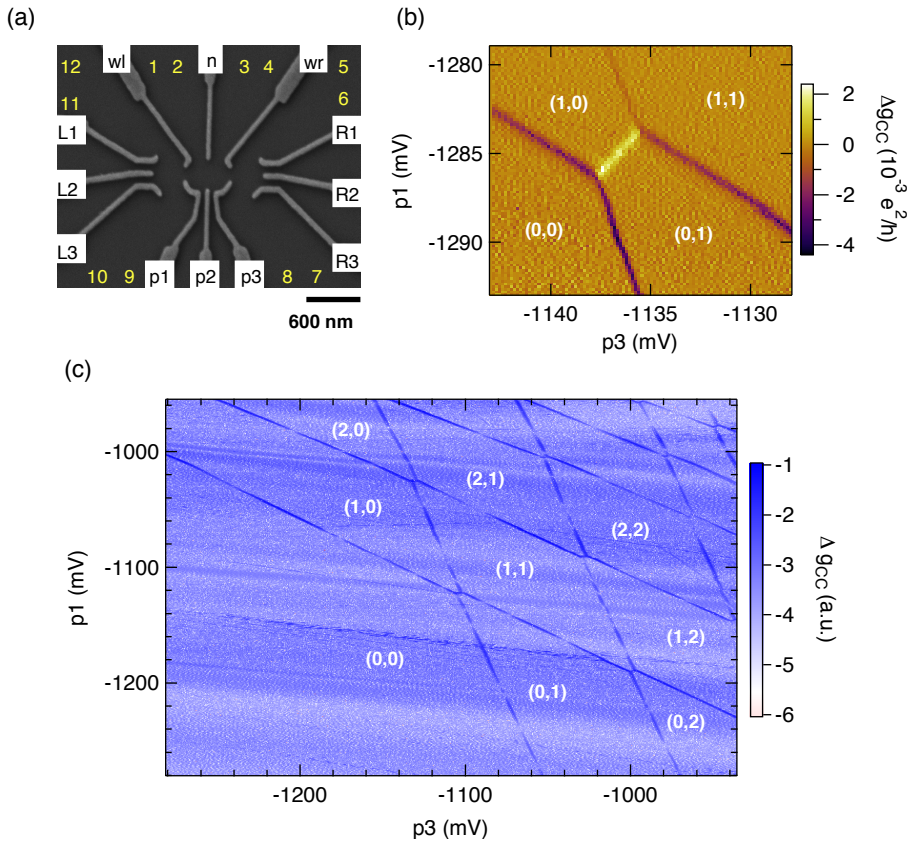

Figure 5.1.: (a) SEM picture of a device similar to the one used in the experiment. Yellow numbers indicate the position of ohmic contacts. Gates p1 and p3 are used to control the double dot, while gates L1, L2, and L3 are forming the left sensor dot. (b) Transition point from $(0,0)$ to $(1,1)$. (c) Large section of the CSD showing numerous charge configurations. The displayed data corresponds to the numerical derivative of the sensor signal Δg_{CC}.

All data presented here was acquired with the left sensor, yet similar results were obtained with the right sensor. The sensor was positioned on the flank of a Coulomb peak to maximize its sensitivity. During measurements the conductance was held approximately constant by a linear feedback mechanism controlling gate L2, to counteract the capacitive coupling to gates p1 and p3 [see Fig.5.1(a)]. The experiment was performed in a dilution refrigerator at a base temperature $T_{mc} = 22\,\mathrm{mK}$. The high stability of the device is demonstrated in Fig. 5.1(c), which displays a repeatable, textbook-like honeycomb structure of the CSD, measured over a large section of charging states. Numerous charge configurations (N_1, N_2), with N_j the occupation number of dot j, are easily distinguishable. A zoom on the $(0,0)$ to $(1,1)$ transition [Fig. 5.1(b)] reveals an undisturbed zero detuning line.

5.4. Metastable Region in the Charge-Stability-Diagram

A new regime is entered by decreasing the inter-dot coupling to tunnel rates smaller than a few Hz. It is characterized by a diamond shaped region centered between the two triple points of the $(0,0)$ to $(1,1)$ transition (see Fig. 5.2). In this region the charge sensor detects a time depending, metastable switching between the $(1,0)$ and $(0,1)$ states. The effect vanishes for larger inter-dot coupling and can only be observed if the tunnel rates to source and drain do not exceed the bandwidth of the charge sensor.

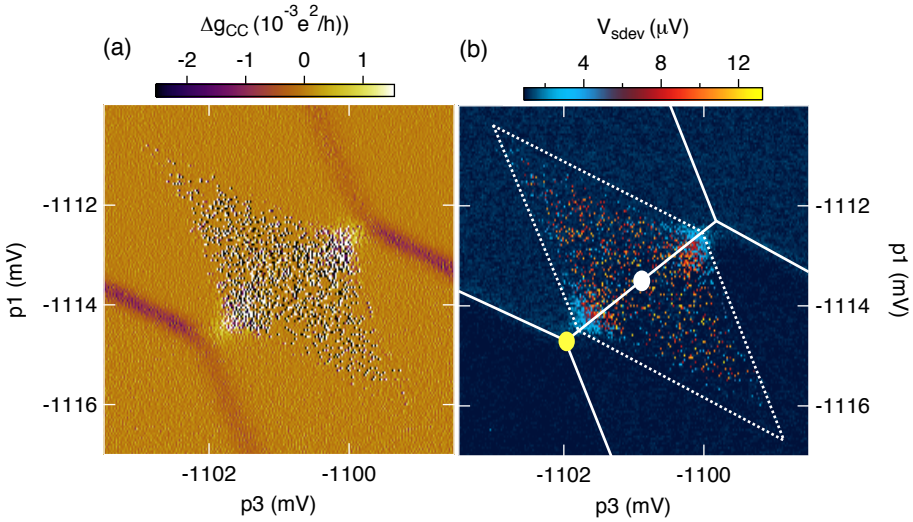

Figure 5.2.: Averaged conductance (a) and standard deviation (b) of the real-time signal of the left charge sensor, with each point integrated over 20 ms. A zoom on the transition between the $(0,0)$ and $(1,1)$ states is shown. The solid white lines in (b) correspond the transition lines of the CSD. The dashed lines mark the borders of the region of detectable charge fluctuations. The white and yellow dots are referring to Fig.5.4.

The detected switching frequencies range from 5 Hz up to a few kHz. A typical time trace is shown in Fig. 5.3 (e). We focus on the $(0,0)$ to $(1,1)$ transition but the effect is also found at different transitions points in the CSD. Since additionally the effect is observed over a wide range of gate voltages, we already can exclude spurious trapped charges as possible explanation. In Fig. 5.2 we show the average and the standard deviation of the real-time measurements, which both clearly display the metastable diamond region. The solid white lines in Fig. 5.2 (b) represent the CSD honeycomb, and the dashed lines the borders of the detectable metastable region. Both types of lines have similar slopes. Since the lines of the CSD are representing the resonance between the energy levels of the double dot and the leads, this hints to an involvement of the leads in the switching effect. We observe this charge switching even at 5 μV bias voltage across the sensor dot. Since also low electron temperatures are required, and

since the diamond represents a broad energy range (the short diagonal corresponds to 148 μeV or 1.7 K), it is unlikely that phonon or photon assisted tunneling causes this effect [112]. Our observations are also clearly distinct from any sensor back-action reported in the literature [113–115].

5.5. Real-Time Data

To further quantify the switching process, we extracted the switching rates between both observed states for all points of the metastable region by analyzing telegraph signals as shown in Fig. 5.3 (e). The resulting 2D tunnel maps are displayed in Fig. 5.3. The upper and lower state of the telegraph signal can be identified with the configurations $(0,1)$ and $(1,0)$. From the times spent in each state, $T_{(0,1)}$ and $T_{(1,0)}$, and the number N of switches during a measurement interval, we determine the switching rates $\Gamma_{(1,0)\to(0,1)} = \Gamma_R = N/(2\,T_{(1,0)})$ and $\Gamma_{(0,1)\to(1,0)} = \Gamma_L = N/(2\,T_{(0,1)})$. Figures 5.3 (a) and (b) show that Γ_L is largest at the upper borders of the diamond, while Γ_R is largest at the lower borders. Within the diamond, both rates are very small compared with their values at the borders. The average switching frequency $f = 2(1/\Gamma_L + 1/\Gamma_R)^{-1}$, shown in Fig. 5.3 (c), has pronounced maxima in the regions closest to the triple points, but is constant everywhere else in the diamond. The probabilities of finding an electron in the right/left dot, $P_{R/L} = \Gamma_{R/L}/(\Gamma_L + \Gamma_R)$ correspond to the z information obtained from long time integrations of the signal. As seen in Fig. 5.3 (d) they contain mainly the traditional information on the $(1,0)$ and $(0,1)$ occupation number regions of the CSD. From Fig. 5.3 (f) we see furthermore that the rates $\Gamma_{L,R}$ have a pronounced temperature dependence. The saturation of $\Gamma_{L,R}$ at low temperatures is due to the saturation of the electron temperature T_e. Above 60 mK, however, $\Gamma_{L,R}$ increases exponentially, showing that the DQD can actually be used as an exponentially sensitive on-chip thermometer. From all this data we deduce that the fluctuations involve a charge exchange with the leads, with the exponential temperature dependence of the rates arising from tunneling into the tails of the Fermi distribution of the leads. Therefore, intermediate charging states, notably $(0,0)$ and $(1,1)$, should be detectable as well.

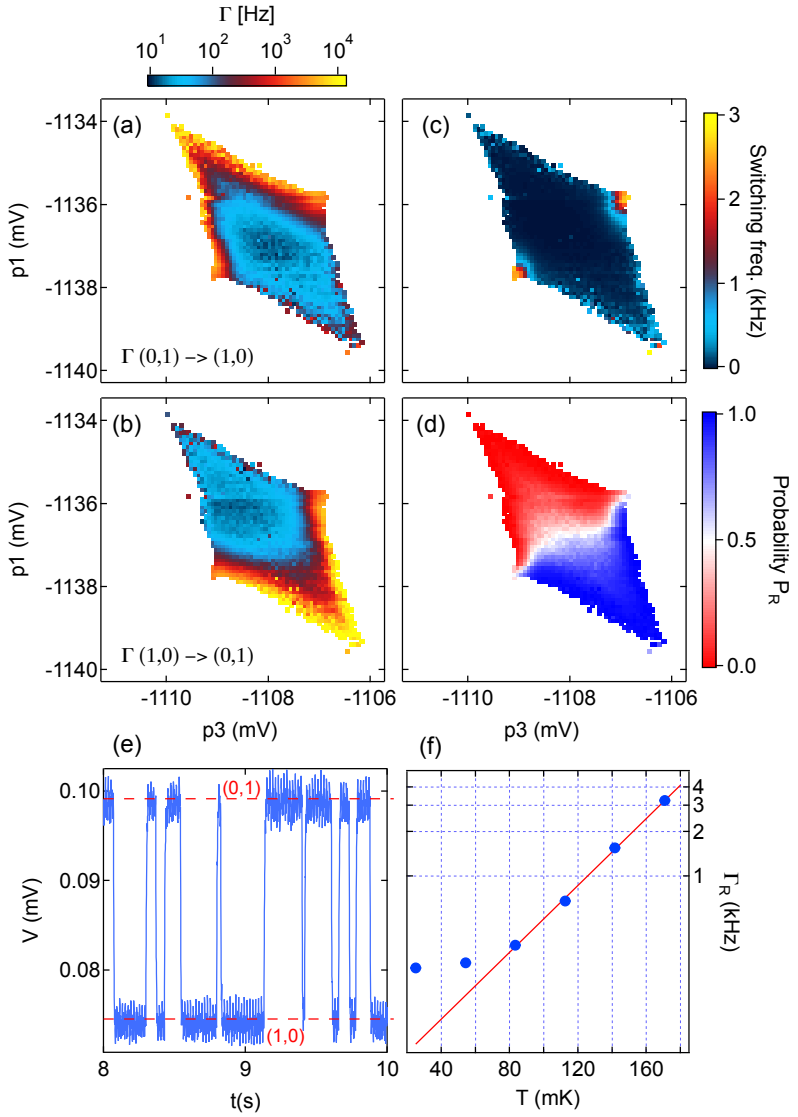

Figure 5.3.: (a) Tunnel rate from $(0,1)$ to $(1,0)$, (b) from $(1,0)$ to $(0,1)$, both in logarithmic scale. (c) Average switching frequency f. (d) Probability P_R calculated from the tunnel rates of (a) and (b). P_R passes through 0.5 on the zero detuning line and is converging to either 1 or 0 for positive/negative detuning. The existence of $P_{(1,1)}$ and $P_{(0,0)}$ are not taken into account here. (e) Example of a real-time trace used to determine $\Gamma_{L,R}$. (f) Exponential temperature dependence of Γ_R, as described in the text (Γ_L has the same behavior). The saturation at low temperatures is due to the saturating electron temperature. The data of (e) and (f) was taken at the center of the diamond [white dot in Fig. 5.2 (b)].

5.6. Time Resolved Four-Level System in the Metastable Region

To corroborate this interpretation, we have further decreased the tunnel coupling to source and drain while heating up the sample to 200 mK. This has slowed down the switching processes, yet allowed us to still detect a sufficient number of switches within

reasonable time.

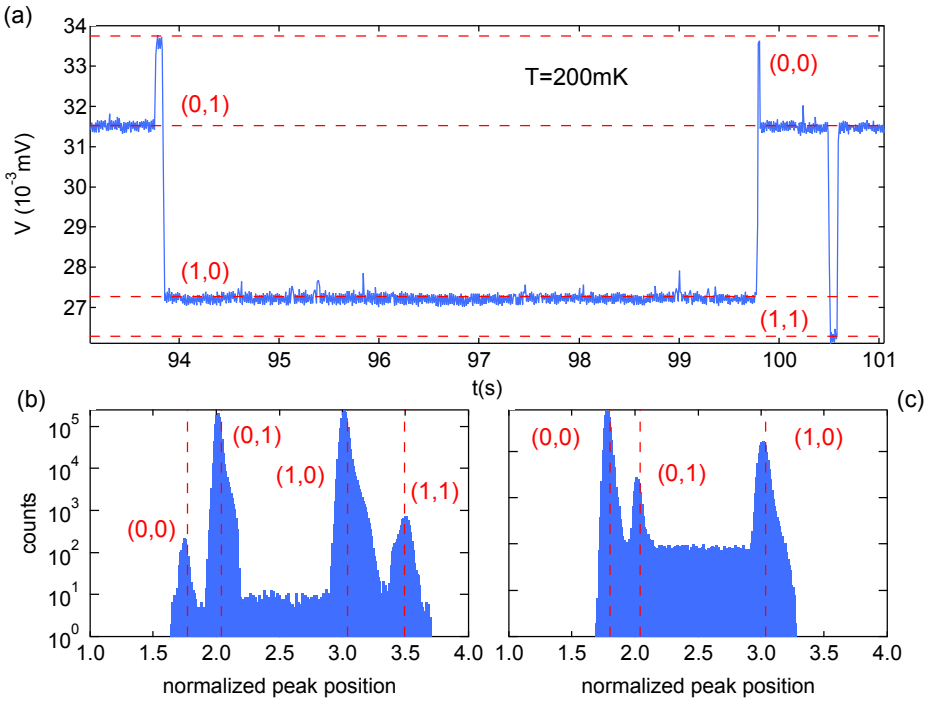

Figure 5.4.: (a) Example for a real-time trace of switching between four states, taken at the center of the diamond [white dot in Fig. 5.2 (b)] at 200 mK. (b) From numerous traces we calculate the histogram displaying the number of counts as a function of peak position normalized to the positions of the $(1,0)$ and $(0,1)$ state. (c) For comparison, at the lower triple point [yellow dot, Fig. 5.2 (b)] only three states can be distinguished. Only in the metastable area all four charge states are visible.

Figure 5.4 (a) shows that then indeed the states $(0,0)$ and $(1,1)$ become visible. From numerous real-time traces as in Fig. 5.4 (a) we have determined histograms showing the number of count as a function of the position normalized to the $(1,0)$ and $(0,1)$ state. In the center of the diamond [white dot in Fig. 5.2 (b)] we obtain the histogram of Fig. 5.4 (b) with 4 clearly distinguishable states. At the lower triple point [yellow dot in Fig. 5.2 (b)] only the 3 states are detectable which are there energetically degenerate. The same qualitative picture is observed for the other triple point, and far outside the diamond on the honeycomb lines of the CSD only the 2 states involved in the corresponding transition are observed. Only within the diamond region we can detect 4 states. In the exact center of the diamond [white dot in Fig. 5.2 (b)] the two large and the two small peaks in Fig. 5.4 (b) are of equal height for identical switching rates. Assuming that $T_e = T_{mc} = 200\,\mathrm{mK}$ we find that the ratio of large to small peaks for the data of Fig. 5.4 (b) is precisely a Boltzmann factor. This allows to extract the lever arm α. We extract α furthermore from the width of the Fermi function obtained from scanning across a charge transition line.

5.7. Extension of the Orthodox Theory for Transport in DQDs

In the following we provide an extension of the orthodox theory for transport in DQDs [48] that incorporates the observed charge fluctuation dynamics. The theory is based on a minimum of assumptions, yet captures all the main features of the observations. We start by noting that the switching rates observed in the experiment are slow enough such that we can use a semi-classical description with definite occupation numbers N_j of dots $j = 1, 2$. The charge fluctuations lead to switching between different configurations $x = (N_1, N_2)$, which we express through a master equation for the occupation probabilities P_x,

$$\partial_t P_x = \sum_{x' \neq x} \left[P_{x'} \Gamma_{x' \to x} - P_x \Gamma_{x \to x'} \right], \tag{5.1}$$

with $\Gamma_{x' \to x}$ the tunneling rate from configuration x' to x. In accordance with the experiment, we maintain only $x = (1,0), (0,1), (0,0), (1,1)$. We can neglect a direct tunneling between the two quantum dots, $(1,0) \leftrightarrow (0,1)$, because it would be lead to resonant switching rates at the boundary between the $(1,0)$ and $(0,1)$ regions of the CSD, which are not observed. Instead the switching rates increase toward the borders of the metastable diamond, where the chemical potential of one of the dots comes close to the Fermi level of the neighboring lead [see Fig. 5.5 (b)]. This indicates that the $(1,0) \leftrightarrow (0,1)$ transition takes place mainly through the intermediate of the $(0,0)$ and $(1,1)$ states, in which electrons are exchanged between dots and leads, and for Eq. (5.1) we keep only the rates between the states $(1,0) \leftrightarrow (0,0) \leftrightarrow (0,1)$ and $(1,0) \leftrightarrow (1,1) \leftrightarrow (0,1)$. By the Pauli principle, the bare tunneling rate Γ_j between dot j and its neighboring lead are weighted by the number of occupied lead states when tunneling onto the dot, $f(\mu_j(N_1, N_2))$, and by the number unoccupied lead states when tunneling out of the dot, $1 - f(\mu_j(N_1, N_2))$. Here $\mu_j(N_1, N_2)$ is the chemical potential of dot j [48], $f(\epsilon) = [1 + \exp(\epsilon/k_B T)]^{-1}$ the Fermi function (with Boltzmann constant k_B and temperature T), and we have chosen the zero of energy at the Fermi level $\epsilon_F = 0$ of the unbiased leads. This leads to the set of rates $\Gamma_{(0,0)\to(1,0)} = \Gamma_1 f(\mu_1(1,0))$, $\Gamma_{(1,0)\to(0,0)} = \Gamma_1[1 - f(\mu_1(1,0))]$, $\Gamma_{(1,0)\to(1,1)} = \Gamma_2 f(\mu_2(1,1))$, $\Gamma_{(1,1)\to(1,0)} = \Gamma_2[1 - f(\mu_2(1,1))]$, assuming energy independent $\Gamma_{1,2}$. The further rates are obtained by $(1,0) \to (0,1)$ and the exchange of indices $1 \leftrightarrow 2$. The stationary solution $\partial_t P_x = 0$ of Eq. (5.1) becomes the straightforward inversion of a 4×4 matrix and leads to the results shown in Fig. 5.5 (c) – (f), which reproduce the main features shown in Fig. 5.3. To understand better the implications of this model, let us assume that $(0,1)$ is the DQD ground state and focus on the transition to the metastable state $(0,1) \to (0,0) \to (1,0)$ as shown in Fig. 5.5 (a).

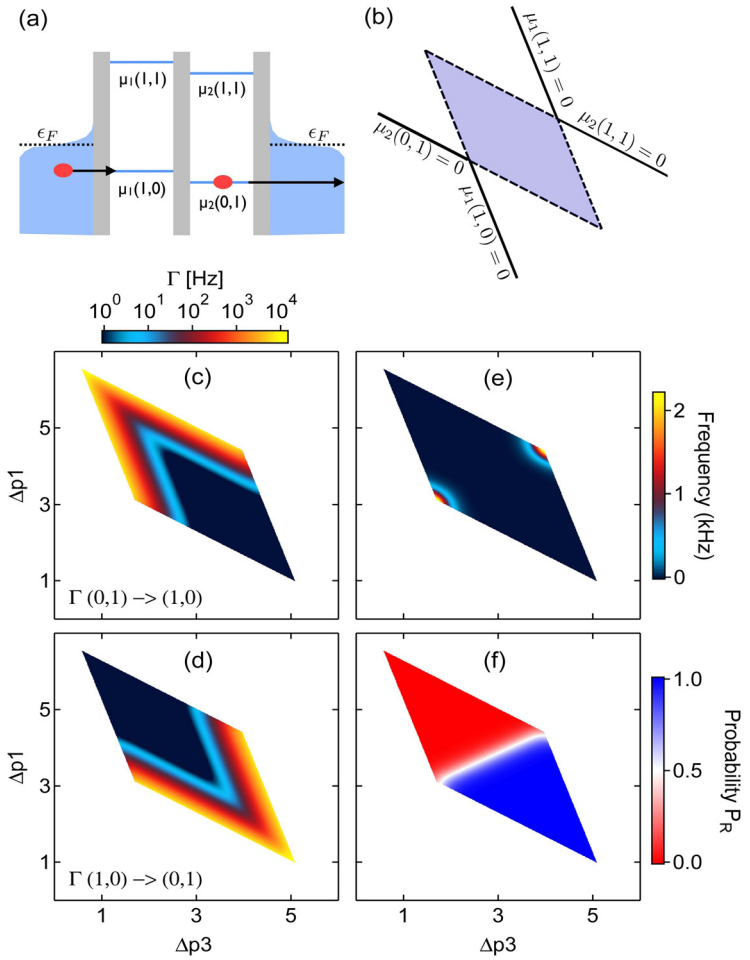

Figure 5.5.: (a) Illustration of the effective switching $(1,0) \to (0,1)$ by first tunneling out of the right dot (slow rate, suppressed by almost unavailable unoccupied states in the lead), and then tunneling onto left dot into the metastable $(1,0)$ state (fast rate due to high occupation number in lead at this energy). (b) Chemical potential at the borderlines of the honeycomb with the blue area indicating where both $\mu_1(1,0), \mu_2(0,1) < \varepsilon_F = 0$. (c)–(f) Calculated transition rates $\Gamma_{L,R}$, average switching frequency f, and probability P_R, qualitatively matching the experimental results shown in Fig. 5.3 (a)–(d). For the calculations $T_e = 60\,\mathrm{mK}$ and $\Gamma_1 = \Gamma_2 = 20\,\mathrm{kHz}$ were assumed.

Since $\mu_2(0,1) < 0$, the first transition, the tunneling of the dot electron into the lead, is strongly suppressed by the exponentially small tail of the Fermi function $1 - f(\mu_2(0,1))$. Such rare transitions set the overall time scale for the slow switching rates. The state $(0,0)$ obtained after this tunneling event, however, is highly unstable since tunneling back into $(0,1)$ is weighted by $f(\mu_1(0,1))$, and so the rate is on the order of the bare tunneling rate Γ_2. Yet, within the shaded diamond shaped region shown in Fig. 5.5 (b), the chemical potential of dot 1 for the configuration $(1,0)$ lies below the Fermi level as well, $\mu_1(1,0) < 0$ [Fig. 5.5 (a)], and tunneling into this metastable state has a large rate $\Gamma_1 f(\mu_1(1,0)) \sim \Gamma_1$, too. Hence the particle spends

a notable fraction of time in $(1,0)$, with short excursions over $(0,0)$ as well as $(1,1)$. The weighting by the Fermi functions shows that the switching frequency increases when $\mu_1(1,0), \mu_2(0,1)$ or $\mu_1(1,1), \mu_2(1,1)$ (for transitions over $(1,1)$) approach 0, which corresponds to approaching the dashed boundaries of the shaded region in Fig. 5.5 (b). Close to the lower triple point $\mu_1(1,0) = \mu_2(0,1) = 0$, the average time spent in $(0,0)$ becomes of the same order as the time spent in $(0,1)$ and $(1,0)$, while state $(1,1)$ is almost never populated and decays very quickly, while at the upper triple point the role of $(0,0)$ and $(1,1)$ is reversed. On the other hand, the line $\mu_1(1,0) = \mu_2(0,1)$ marking the separation between the $(0,1)$ and $(0,1)$ regions has no special feature since the direct tunneling $(0,1) \leftrightarrow (1,0)$ is absent. All these characteristics reproduce the main experimental observations. Of course, there are discrepancies between model and data, most prominent being the S-shape of $P_R \approx 0.5$ in Fig. 5.3 (d). If each dot is tunnel coupled to more than a single lead, such an S-shape could arise from slight differences in the Fermi levels leading to a multi-step shape of the transition rates, due to the sum over shifted Fermi functions. Alternatively, the screening in the leads of the different charge configurations on the DQD leads to slight shifts of the chemical potentials. Different energy shifts from $(1,1)$ and $(0,0)$ then can cause an asymmetry along the $(0,1),(1,0)$ boundary.

5.8. Summary

In summary, we observe thermally activated switching between the four charge states connected by the diamond shaped area, and we can identify it as intrinsic charge fluctuations. The time scale $T_f \sim 1/\Gamma$ of this effect is a natural limitation of T_1, where Γ is the fastest switching rate. Generically in the diamond, this rate is on the order of the rates of tunneling into the $(0,0)$ or $(1,1)$ configurations. Therefore, a very small coupling to the leads is most likely necessary, yet a further tuning can be achieved through the dependence on the tails of the Fermi distribution in the leads. As a consequence, however, the initialization time of the qubit would be much longer than, e.g., the 50 ns in recent experiments [116].

Acknowledgments

We thank M. Brühlmann and D. Stepanenko for helpful discussions. The support by the Swiss SNF is gratefully acknowledged.

Chapter 6

Thermally Activated Charge Fluctuations - Addendum

In the previous chapter some of the main results of this thesis are discussed, namely the effect of thermally activated, metastable charge state switching in GaAs double quantum dots. This newly discovered effect is an intrinsic feature of double quantum dots coupled to electron reservoirs and hence is of great interest. In this chapter additional data is presented, that underlines some of the statements and conclusions of chapter 5.

The first section of this chapter treats the influence of tunnel coupling to source and drain on thermally activated tunneling and clarifies further, how to tune a DQD to the regime where this effect is observable. The fact, that thermally activated charge state switching can be observed at different electron transitions of the DQD simultaneously, is illustrated in the second section of this chapter. Here, a detailed data set is presented, showing the (1,1) to (0,2) electron transition of the device, which is of particular interest for spin-qubits implemented in similar devices. Though the temperature dependence of the thermally activated tunneling processes is captured in quite some detail in chapter 5, the third section of this chapter provides some additional data required to give a complete picture of the influence of temperature on the experimental observations. Finally, the last section treats the influence of a DC bias across the charge sensor on the shape of the metastable area in which thermally activated tunneling occurs. Further, the influence of an additional DC bias across the DQD is presented as well. The effect observed here is discussed briefly in chapter 5, but the data shown here sheds more light on this matter, which is not yet completely understood and may even be the starting point for additional experiments on this newly discovered effect.

6.1. The Influence of Tunnel Coupling

Thermally activated tunneling describes tunneling processes from the DQD to electron reservoirs and vice versa, in the area of the charge stability diagram where both dots have energy states that lie below the chemical potential in the reservoirs (see chapter 2 and chapter 5). Hence, the tunnel coupling to those electron reservoirs plays a crucial role for this effect. By variation of the tunnel coupling to both electron reservoirs and realization of symmetric- and asymmetric tunnel coupling, one can examine, if the effect shows the expected dependencies. Figure 6.1 (a) and (c) shows the same region of the CSD, namely the (0,0) to (1,1) transition but for different couplings to source and drain. The data presented in this graph was obtained by reducing the coupling to the drain electrode by decreasing the gate voltage applied to gate wr (see Figure 2.2) by more than 100 mV. In Figure 6.1 (a) the region of metastable charge state switching

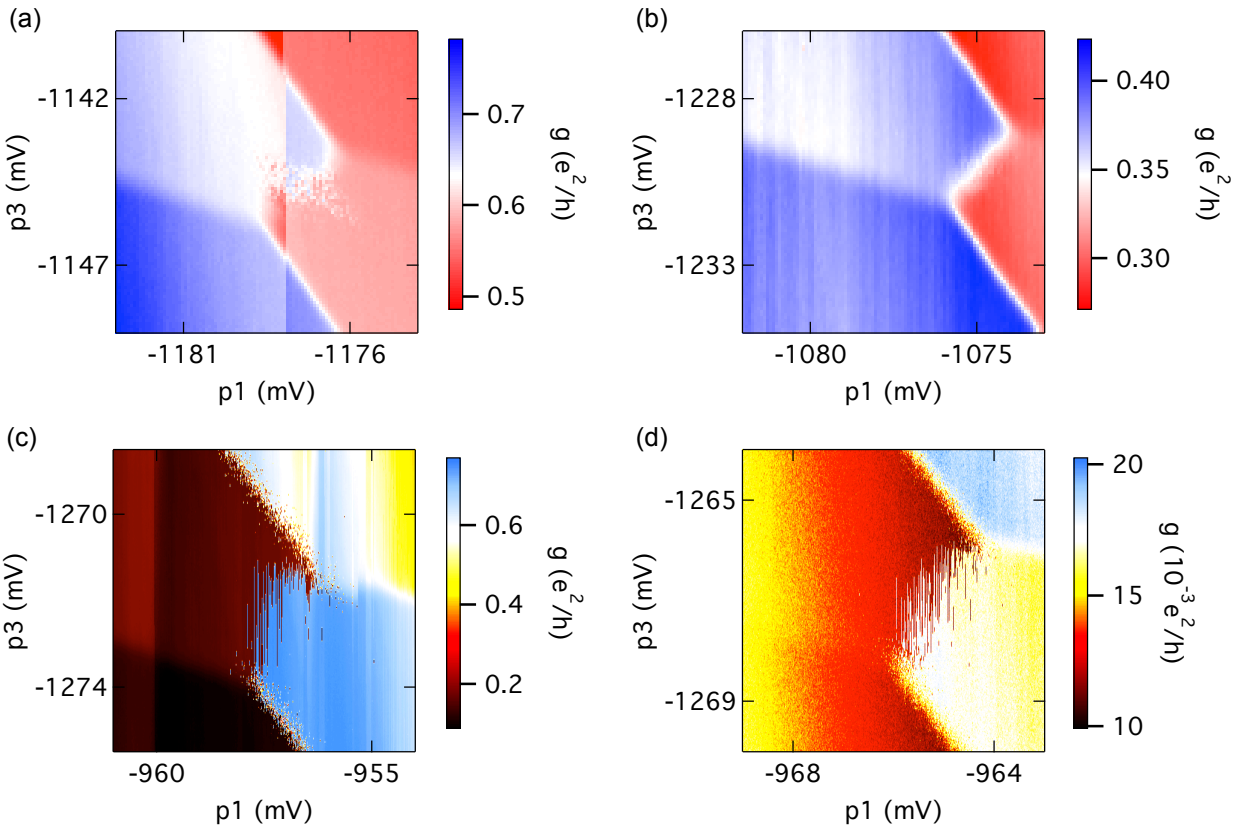

Figure 6.1.: Influence of coupling to source and drain: (a)-(b) While the *noise diamond* is present in (a), it cannot be observed in (b), where the coupling to the drain side was increased considerably, by applying a less negative voltage to gate wr (see Figure 2.2). (c)-(d) By further decreasing the coupling to the source side with respect to the configuration in (a), the according charge transition line can be resolved in real-time, and the metastable charge state switching depicts a lower frequency. Both observations are in very good agreement with the model of thermally activated tunneling.

is pronounced very clearly, although the observed borders do not expand to the theoretical maximum (see Figure 5.5). The reason for this is the limited bandwidth of the real-time setup, which does not allow to resolve the high frequency metastable charge state switching in the region between the theoretical borders and the observed borders of the *noise diamond*. In Figure 6.1 (b), where the coupling to the drain electrode is much higher due to the less negative voltage on gate wr, the metastable region cannot be observed. This does not mean that metastable charge state switching does not occur, instead one interprets this observation as an increase in switching frequency beyond the measurement bandwidth, in agreement with the theoretical model presented in chapter 5. The completely analogue behavior is observed by increasing the coupling to the source side, instead of the drain side (no example shown).

From the gate voltage configuration of Figure 6.1 (a), one can further decrease the coupling to source by applying a more negative voltage to gate wl. From the model of thermally activated tunneling, presented in chapter 5, one would expect this procedure to decrease the switching frequency in the metastable region. Figure 6.1 (c) and (d) show according measurements, where the coupling to source was reduced strongly, as indicated by the (0,0) to (1,0) transition line, that now can be resolved in real-time. At the same time, the switching frequency in the metastbale region decreases considerably. This can be deduce from the very long times the system now remains in either one of the charge states, which leads to a *latching* like effect in Figure 6.1 (c) and (d). Additionally, the diamond now extends to the full range that theoretically is possible, i.e. over the full range of the zero detuning line.

Both measurements are in full agreement with the model. Further, measurements like this, which help to understand the behavior of this new effect, helped developing this model, since they depict a very characteristic behavior. Hence, when tuning a DQD device to the regime where thermally activated tunneling can be observed, measurements like those in Figure 6.1 can be used as consistency test.

6.2. Visibility at Different Transitions

Thermally activated tunneling is an intrinsic effect that should exist in any DQD device coupled to source and drain electrodes. While the observability of this effect depends on the coupling to source and drain, as well as on the inter-dot coupling and the bandwidth of the implemented real-time setup, it should not depend on the investigated electron transition (e.g. (1,0) to (0,1) or (0,2) to (1,1)). Therefore, thermally activated tunneling is expected to be visible at higher transitions than the (0,0) to (1,1) transition. Figure 6.2 depicts a large area of the charge stability diagram of the same device, which also is the object of investigation in chapter 5. While Figure 6.2 (a) shows raw

data obtained by charge sensing, a processed version of the same data set is depicted in (b). In the raw data one can distinguish several charge transition lines plus two spots, where the conductance of the charge sensor is increased by almost a factor of two. Those two spots correspond to metastable regions, i.e. *noise diamonds* at higher transitions. This fact becomes more obvious in the processed version of this data set in Figure 6.2 (b). In order to simplify orientation in the charge stability diagram, the according charge configurations are marked in this graph (white numbers). The four white arrows in Figure 6.2 (b) point towards four different charge transitions, where the metastable region can be observed, simultaneously, i.e. in the same measurement. This measurements verifies the universality of the observed effect and that thermally activated charge state switching is not limited to a special electron transition of a DQD. This might particularly be of interest in experiments, which require operating a DQD device in different charge configurations and close to the zero detuning line of the respective transition. Whenever a DQD device is operated in the region of the CSD, where thermally activated tunneling is possible (for very low inter-dot coupling and observable only if tunneling rates to source and drain do not exceed the bandwidth of the charge sensor), the resulting effects and influences on the respective experiments have to be considered. This also applies to spin-qubit experiments, where the (1,1) to (0,2) transition of a DQD plays a crucial role. All these spin-qubit experiments rely on driving the DQD from one charge configuration to the other (e.g. from (1,1) to (0,2)) and any distortion of these states, or the participation of intermediate states in the CSD are parasitic effects. However, since thermally activated tunneling is an intrinsic effect, one cannot simply avoid this effect and hence has to take into account its influences on the respective experiment.

Since a large number of experiments on spin-qubits are done at the (1,1) to (0,2) transition, Figure 6.3 demonstrates the presence of the *noise diamond* at this transition. Here, one can clearly observe the region of metastable charge state switching, equivalently to the (0,0) to (1,1) region of the CSD, that was investigated in detail in chapter 5. In this measurement, the *noise diamond* does not extend up to the triple points of the CSD, i.e. to the theoretical maximum (this is again due to the limited bandwidth of the real-time setup).

Whether or not the presence of this effect has influence on spin-qubit experiments, depends strongly on the respective time-scales. Experiments on spin-qubits usually incorporate fast pulsing sequences in the order of nanoseconds. If those pulses and the associated experiments occur on a time-scale much faster than the processes, that are connected to thermally activated tunneling, the effect described here will not influence those experiments. If this is not the case, thermally activated tunneling might be a enormous problem, since those tunnel processes destroy coherence. The reason

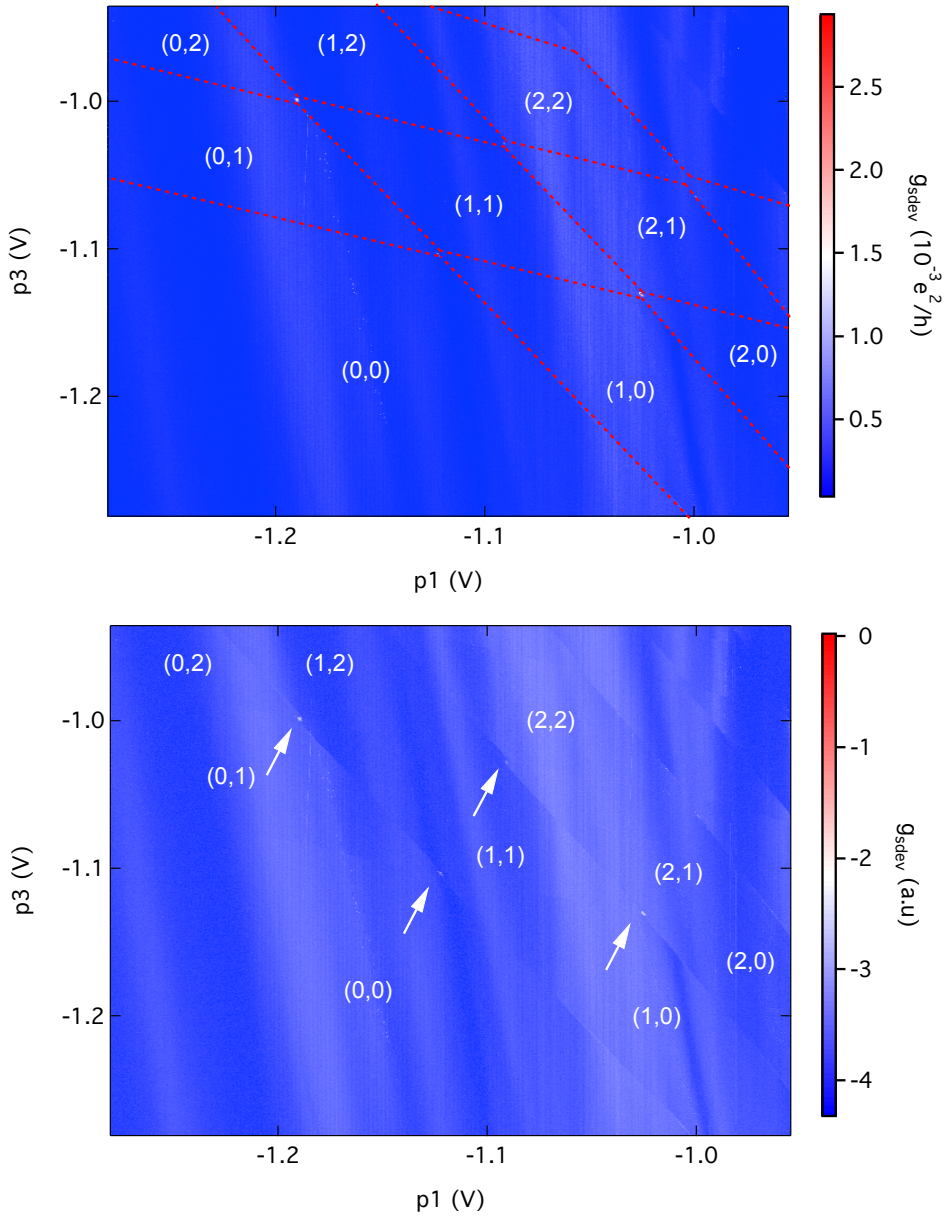

Figure 6.2.: Thermally activated charge state switching at different electron transitions: (a) Larger section of a measured CSD, where several charge transition lines between different charge configurations can be identified. Additionally, two spots with increased charge sensor conductance appear, which correspond to *noise diamonds*. (b) Processed version of the same data set as in (a), where white numbers indicate different charge configurations of the DQD and white arrows point at different *noise diamonds*, observed simultaneously in this measurement.

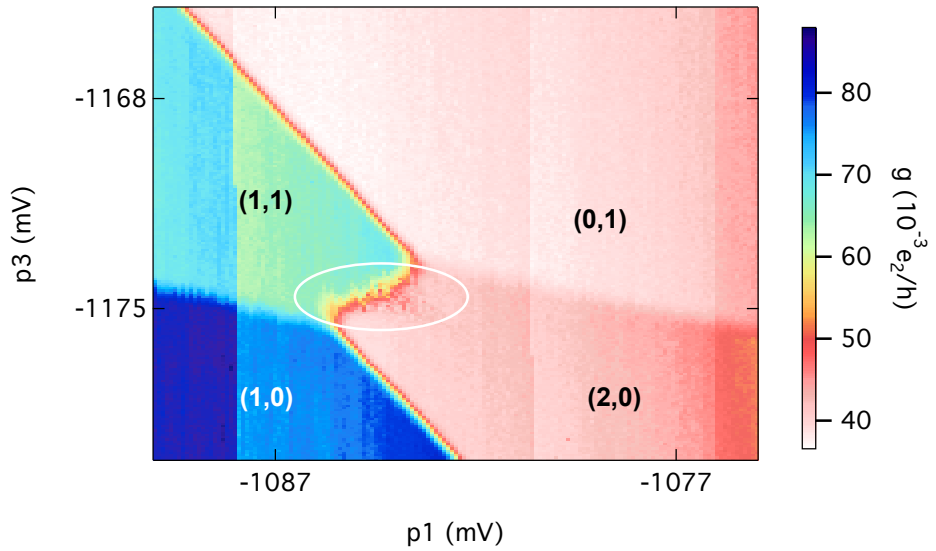

Figure 6.3.: Charge sensing measurement showing the (1,1) to (0,2) (black numbers) transition of the charge stability diagram, including a area where metastable charge state switching is observed (white circle). Since this electron transition is of special interest for implementing spin-qubits, the presence of this effect and its consequences for the respective spin-qubit experiments should be considered carefully.

for this is that thermally activated tunneling processes include electron exchange with the leads. Consequently, the electrons in the DQD are replaced with electrons from the leads, which inevitably destroys coherence. Since the time-scale on which thermally activated tunneling takes place depends strongly on the coupling to source an drain, a sufficiently high tunneling barrier to both electron reservoirs should ensure an undisturbed execution of such spin-qubit experiment. The drawback, however, is that weak coupling to the reservoirs, next to reducing the metastable charge state switching frequency, also increases the timescale to initialize a qubit. Of course, temperature is another important parameter, which has to be considered here. In general, lower electron temperature slow down tunneling processed that are caused by thermal activation.

6.3. Temperature Dependence

Tunneling processes due to thermal activation, obviously, show a pronounced temperature dependence, as depicted in Figure 5.3. The observed exponential temperature dependence, was already discussed in chapter 5. The quantitative analysis there is the result of measuring the tunneling rate at one fixed position within the metastable area. Due to the increasing temperature, the Fermi distribution in the leads broadens, hence the number of unoccupied electron states below the chemical potential increases.

Consequently, the rates of thermally activated tunneling, which are proportional to the number of unoccupied states below the chemical potential, increase as well (see Equation 5.1 and the corresponding section 5.7 of chapter 5).

Figure 6.4 mediates a qualitative picture of the temperature influence on the area of thermally activated tunneling. Here, the same section of the charge stability diagram is depicted for four different refrigerator temperatures. Figure 6.4 (a) was measured at a fridge temperature of 50 mK. From previous measurements, the base temperature of the fridge (22 mK) is known to correspond to an electron temperature of about 50 mK. Hence, in the data set of Figure 6.4 (a) one expects a very similar behavior as for base temperature. In this graph the area of metastable charge state switching displays the same appearance as in some of the measurements displayed and discussed above. Due

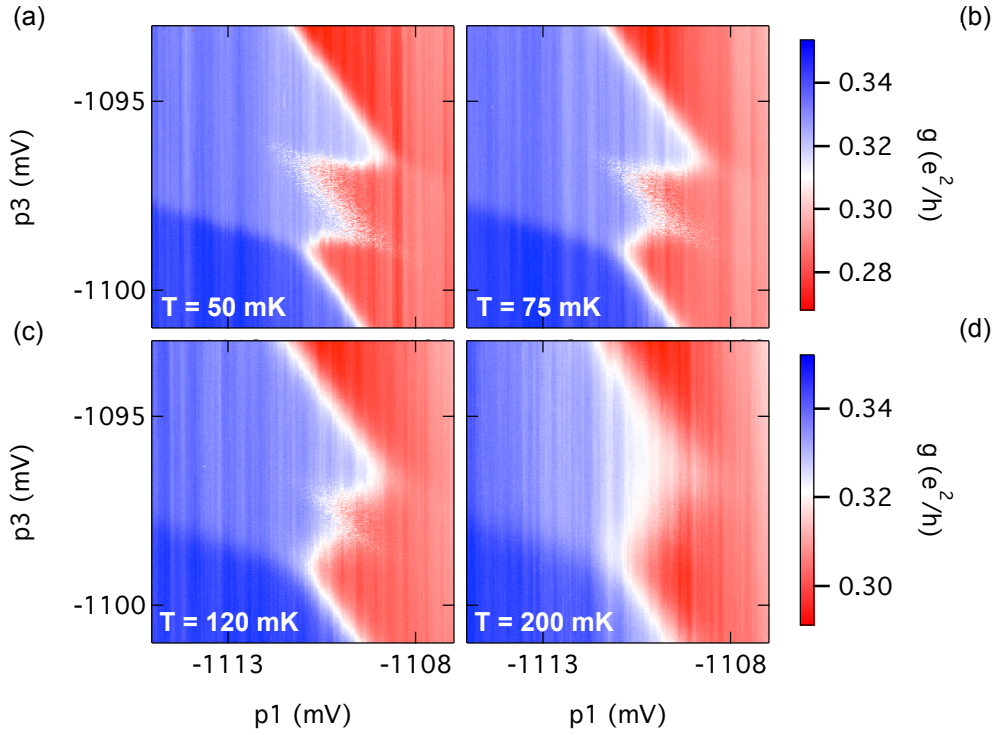

Figure 6.4.: Qualitative analysis of the temperature dependence of thermally activated tunneling: (a) At a fridge temperature of 50 mK the *noise diamond* is clearly visible. The borders of the *noise diamond* are given by the bandwidth of the real-time setup. (b) and (c) step-wise increasing the fridge temperature leads to higher tunneling rates, hence the observable area of thermally activated tunneling reduces. (d) At a fridge temperature of 200 mK the measured CSD is almost undisturbed, since thermally activated tunneling processes are now too fast to be detected. All four data sets were taken with a DC bias $V_{DC} = 75\,\mu$V across the charge sensor, which leads to the Z-shape of the metastable area (see next section).

to tunneling rates that exceed the maximum frequency still detectable by the real-time charge sensing setup, the measured area of thermally activated tunneling does not fill

out the total area, where this effect is possible according to the model. By increasing the temperature, the area where thermally activated tunneling is observable with the available real-time setup shrinks further, as can be seen in Figure 6.4 (c) to (d). For a fridge temperature of 75 mK and 120 mK (Figure 6.4 (b) and (c)), the effect is still detectable, but in a much smaller section of the CSD. For the data set in Figure 6.4 (d), which corresponds to a fridge temperature of 200 mK, the effect seems to be almost completely absent. The result is a almost undisturbed charge stability diagram, where thermally activated tunneling is still present in the system, but cannot be detected with the used real-time setup.

This series of measurements further illustrates the influence of temperature on thermally activated tunneling and clarifies that, depending on the actual electron temperature of the system and the bandwidth of the according experimental setup, this effect can be hard to detect and even seems to be absent. Hence, this effect is overlooked very easily. However, the data presented here, in combination with the quantitative temperature dependence already discussed in chapter 5, is in absolute agreement with the predictions made by the model of thermally activated charge state switching.

6.4. Bias Dependence

The last section of this chapter, which has to be read as an complement to chapter 5, treats the influence of a DC bias across the charge sensor and across the DQD on the effect of thermally activated tunneling. The resulting data is not yet understood and might be the subject of future experiments aiming at learning more about this issue.

Figure 6.5 shows as series of measurements depicting the measured tunneling rate $\Gamma_{(1,0)\to(0,1)}$ alongside the corresponding Probability P_R for an electron to be in the right dot of the DQD system (gate p3 is the right *hand-gate* of the DQD system, see also Figure 2.2), as a function of DC bias across the charge sensor. The tunneling rate $\Gamma_{(1,0)\to(0,1)}$ in all four panels shows as similar behavior as in Figure 5.3. While the tunneling rate $\Gamma_{(1,0)\to(0,1)}$ is very high at the outer border of the right side of the metatstable area, a rapidly decreasing rate towards the left half of the diamond shaped area is observed. The measured tunneling rates vary over more than two orders of magnitude from the right to the left side of the metastable area. As stressed in chapter 5, the reverse situation is observed for $\Gamma_{(0,1)\to(1,0)}$[1]. From the data in Figure 6.5 one can see, that with increasing DC bias across the charge sensor, the originally V-shaped area of very high tunneling rates is transformed towards a Z-shaped area (see Figure 6.5 (d)).

[1]Note, that here the same nomenclature is used as in chapter 5, although there it is demonstrated, that within the model of thermally activated tunneling no direct tunneling from (0,1) to (1,0) is occurring and all tunneling processes require an intermediate state which either is the (0,0) or the (1,1) charge state of the DQD system.

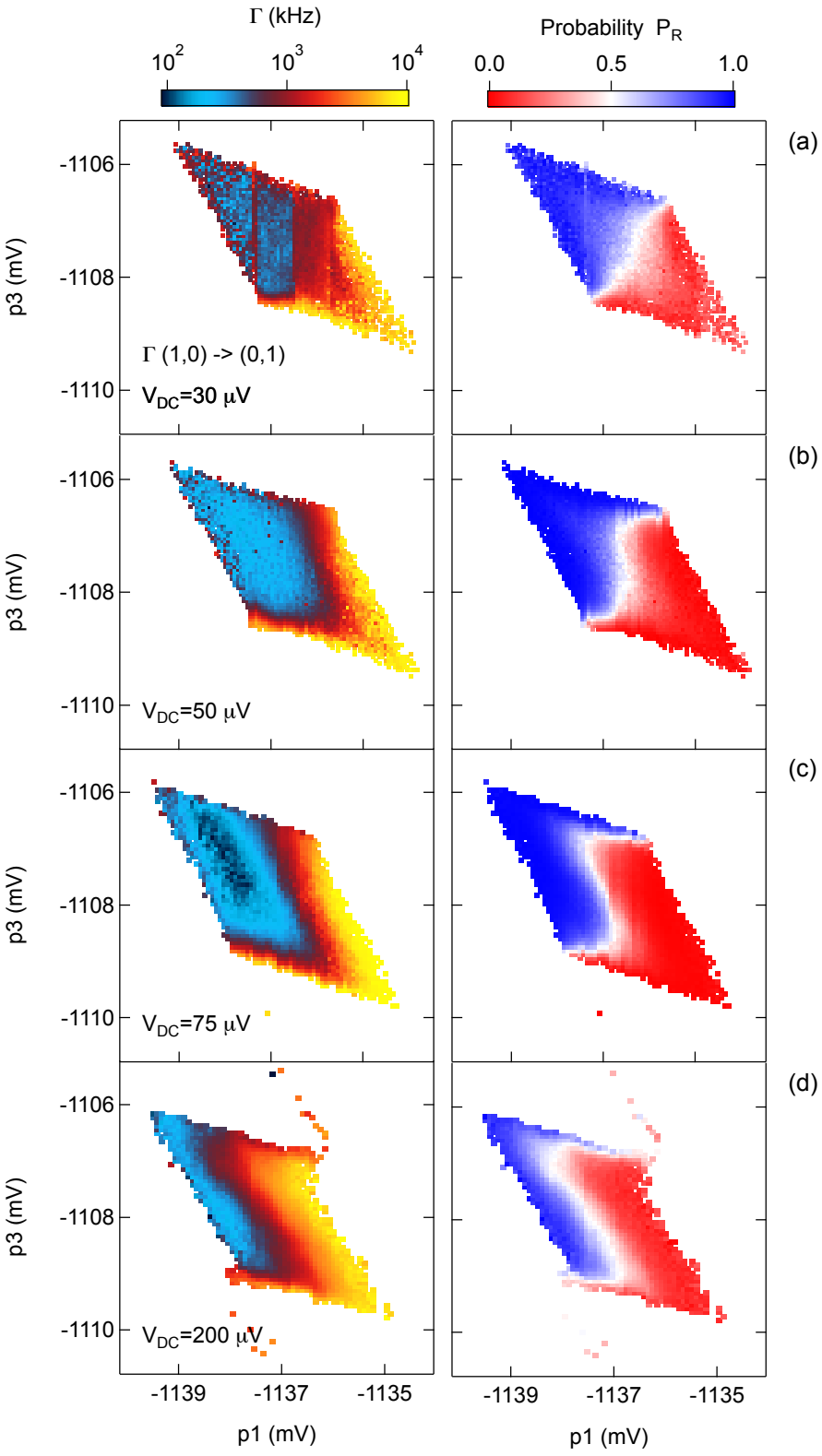

Figure 6.5.: Illustration of the influence of DC bias across the SQD on the effect of thermally activated tunneling: On the left side of panel (a) - (d) the rate $\Gamma_{(1,0)\to(0,1)}$ is depicted for different values of V_{DC}. Increasing the DC bias transforms the originally V-shaped region of high tunneling rate (yellow) to a more Z-shaped area. The right side shows the according Probability P_R for beeing in the right dot. Here, the same transformation is observed for the zero-detuning line (white), where $P_R \approx 0.5$. The P_R shown here was calculated from $\Gamma_{(1,0)\to(0,1)} = \Gamma_R$ and $\Gamma_{(0,1)\to(1,0)} = \Gamma_L$ by $P_R = \Gamma_R/(\Gamma_R + \Gamma_L)$.

On the right side of Figure 6.5 the according probability P_R for an electron to be on the right dot shows an interesting behavior as well. For low DC bias the probability is almost split into two sides, one with probability one, and the other with probability 0. Only a thin zero-detuning line separates both areas from each other, on which P_R is 0.5. This behavior is precisely what is expected within the classical model of a DQD, where well-defined charge states without the influence of thermally activated tunneling area treated. For increasing DC bias across the charge sensor, however, the situation changes. Here, the Z-shaped featured described above emerges as well, but now mainly the zero-detuning line seems to be affected. As already pointed out in chapter 5, the feature of thermally activated tunneling persist even for very low DC bias across the sensor dot, therefore on can rule out that some kind of back-action triggers the observed tunneling processes. However, the data depicted in Figure 6.5 imply, that at least a high DC bias across the sensor dot can influence the effect of thermally activated tunneling in a double quantum dot.

Additional observations, as depicted in Figure 6.6, further imply a DC bias across the DQD system to have influence on the effect of thermally activated tunneling as well. In this graph, two configurations of DC bias across the DQD are shown, where $V_{DC,DQD} = \pm 125\,\mu\text{V}$, while the DC bias across the SQD was fixed at $V_{DC} = 75\,\mu\text{V}$. In both situations, the originally diamond shaped area of thermally activated tunneling is deformed into a thin line, which is orientated almost perpendicular to the original zero-detuning line of the CSD. Within this thin area, where tunneling events still are detected, one can still identify a substructure. Thin areas, where $P_R = 0$ or $P_R = 1$ respectively, are separated by a very thin transition region where $P_R \approx 0.5$. The most important observation is, that reversing the bias across the DQD seems to reverse the areas where $P_R = 0$ and $P_R = 1$ (compare right side Figure 6.6(a) and (b)). Since P_R is calculated from the measured tunneling rates, the same is true for the tunneling rate $\Gamma_{(1,0)\to(0,1)} = \Gamma_R$ and $\Gamma_{(0,1)\to(1,0)} = \Gamma_L$. Areas with high tunneling rate in (a) (yellow areas), are areas with low tunneling rate in (b) and vice versa. The arms reaching out from the edges of the metastable area on the left side of Figure 6.6 (a), are not part of the metastable area itself. Instead, the events detected here are part of a charge transition line in the CSD, which can be resolved in real-time here due to a small coupling to the corresponding electron reservoir.

The influence of DC bias across SQD and DQD described here, is not fully understood within the extension of the orthodox model of a DQD, presented in chapter 5. This model does not capture a feature, as the one described above. As is pointed out in chapter 5, different explanations are considered. One of these possible explanations is the presence of more than one electron reservoir coupled to each dot of the QD system. In general, a serial DQD is assumed, where every dot is only coupled to one lead. How-

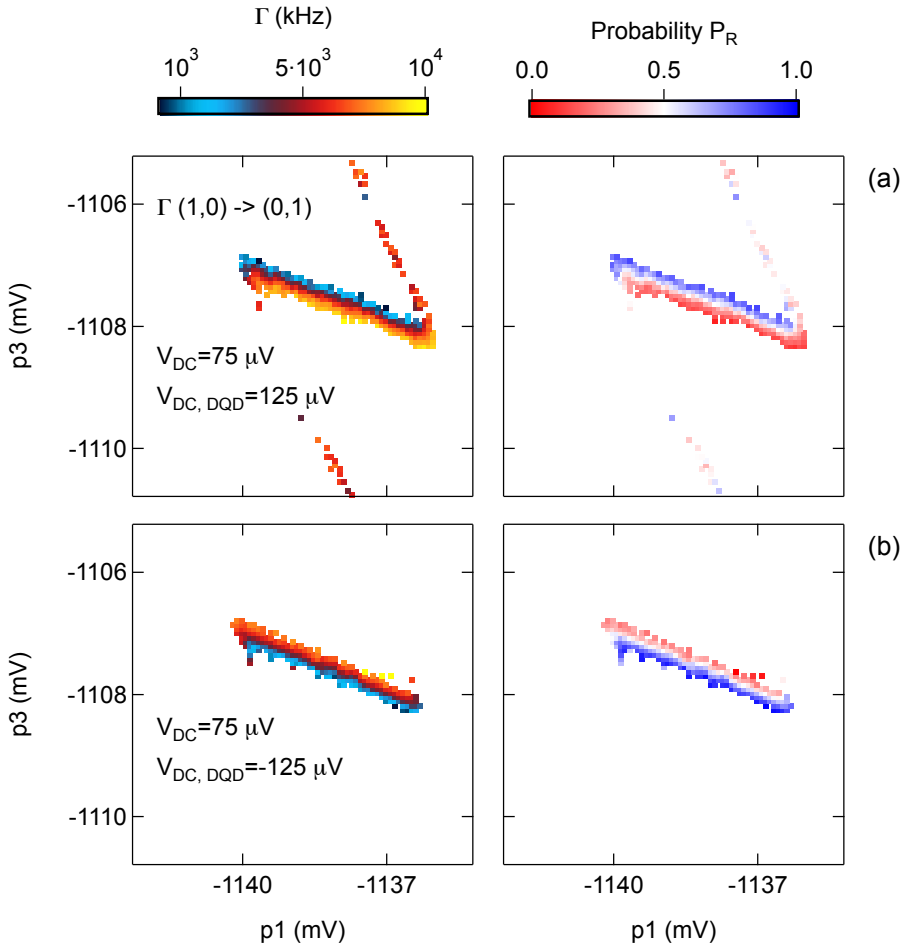

Figure 6.6.: Adding an additional DC bias $V_{DC,DQD}$ across the DQD to a DC bias V_{DC} across the SQD, deforms the originally diamond shaped area of thermally activated tunneling. In (a) $V_{DC,DQD} = +125\,\mu$V, while in (b) the bias across the DQD is reversed, i.e. $V_{DC,DQD} = -125\,\mu$V. Comparing panel (a) and (b) one observes, that the region of high tunneling rates are reversed (yellow areas). Consequently, calculating P_R leads to reversed probabilities as well. However, the slope of the observed feature is still equal to a reservoir slope, i.e. one of the slopes of the charge stability diagram.

ever, if e.g. due to a damaged gate or a very small voltage applied to a gate, the dots are coupled to more than one electron reservoir, the situations changes. If one of the dots is coupled to more than one lead, and those leads have slightly different chemical potentials/Fermi levels, the Fermi functions in each lead are shifted with respect to each other. Hence, the transitions of thermally activated tunneling is expected to show a multi-step shape. This asymmetry could possibly explain the observations made in Figure 6.5 and Figure 6.6. A DC bias across the DQD itself, would obviously effect the source and drain leads of the DQD and hence might influence the asymmetry of the leads. On the other hand it is not completely obvious why in this case the DC bias across the sensor dot would influence this behavior as well, unless the SQD and the DQD share a common electron reservoir. However, from the gate voltages applied to the according gates and the corresponding pinch-off tests, this can almost certainly be ruled out.

Another possible explanations might be a asymmetry induced by screening effects in the leads. If different charge configurations of the DQD system would generate different screening configurations in source and drain, the consequence would be different chemical potential in the leads, inducing the same asymmetry as described above. In case the (1,1) and (0,0) charge configurations would generate different energy shift in the leads, due to screening, an asymmetry at the (0,1) to (1,0) transition is possible.

Whether or not one of the above explanations is correct, cannot be deduced from the available data. Due to the long time it takes to perform such measurements, as they are depicted in Figure 6.5 (and due to technical problems with the dilution refrigerator[2]) a more through analysis of this issue was not possible. Therefore, it would be of great interest to take up the experiment again, and do a more detailed analysis of the influence of the DC bias across the SQD and the DQD on thermally activated tunneling. Not only experiments with the same device would be of interest here. In addition, probing another sample might help to identify if one of the mechanisms discussed above is responsible for the observations. For example, if one of the dots is coupled to more than one lead, because of a small gate defect or a rather small voltage applied to one of the gates, then the situation would very likely be different for another device. In the context of bias dependence, all data shown here, was taken at the (0,0) to (1,1) transition of the CSD. Higher transitions were not investigated, but in case screening effects in the leads cause the observed effect, the situation might be different at higher transitions. In conclusion, further experiments are required to determine the correct mechanism for the observed bias dependence.

[2]A leak in the OVC of the Dewar forced a shut down of the experiment for several months.

Chapter 7

Spin Relaxation in GaAs quantum dots

This chapter treats spin relaxation time measurements on single electron GaAs quantum dots. Spin relaxation is an important physical process, that has been investigated in many different systems [20]. In this work, the focus lies on lateral quantum dots based on AlGaAs heterostructures, because this system has great potential for implementing spin-qubits. The first section of this chapter motivates the present experiment, and the relation to previous works in the field is discussed. The second section introduces the physical mechanisms leading to spin relaxation. Especially the important role of spin-orbit interaction is pointed out there. The experimental realization of spin relaxation time measurements is subject of the third section of this chapter. Finally, in the fourth and last section, the measurement results are discussed, as well as further steps to complete the experiments.

7.1. Overview and Motivation

It is known in quantum mechanics that every experiment is influenced considerably by its environment. Completely isolated systems are theoretical models that are probably impossible to realize in practice. Therefore it is essential, e.g. for quantum information processing, to understand the interaction between a quantum system and its environment [117]. The spin state of electrons in lateral GaAs quantum dots is one system that is of particular interest for quantum information processing [16, 21, 118, 119]. During the last years, numerous experiments on this system have demonstrated the successful manipulation and read-out of electron spin states [20, 23, 24, 26, 120, 121]. In addition, the influence of the environment on spin states of electrons was investigated. Here, especially the hyperfine interaction between nuclear spins and electron spins has to be mentioned, since the dominant decoherence mechanism arises from this interaction [23, 33, 36, 101, 102]. The timescale on which phase information is carried away into the environment - the decoherence time T_2 - was studied intensively [39, 122, 123].

Another important interaction between electrons in a quantum dot and their environment, is the exchange of energy. In the presence of an external magnetic field B, the spin-up and spin-down state of an electron in a quantum dot are no longer degenerate and the energy difference is given by the Zeeman splitting $E_Z = |g|\mu_B B$. Consequently a quantum mechanical two-level system arises. Energy exchange between an electron in the quantum dot and its environment causes spin relaxation (or excitation) processes and brings the system into thermal equilibrium. The timescale on which this process takes place is the spin relaxation time T_1. In case the Zeeman energy E_Z exceeds the thermal energy of the electron by far, i.e. $E_Z \gg k_B T_e$, T_1 can be interpreted as the average time required for an electron in the excited spin state to relax to the ground state. Energy relaxation inevitably destroys coherence, therefore the timescale T_1 on which energy exchange takes place always exceeds the coherence time T_2 of the system. As is demonstrated in the work of Golovach *et al.* [32], the relation $T_2 \leq 2 \cdot T_1$ holds.

The exact physical process which is responsible for the energy exchange between electrons and environment, i.e. the exact spin relaxation mechanism, is treated in a variety of works [32, 124–132]. In general, one has to distinguish two different regimes. First, if the external magnetic field is comparable to the magnetic field fluctuations caused by the ensemble of nuclear spins, i.e. $B \sim B_{nuc}$, there is significant interaction between electron spins and nuclear spins, leading to spin relaxation [33]. The other limit is given by $B \gg B_{nuc}$, where the Zeeman splitting is to large to allow for interaction with the nuclear spins, due to the energy mismatch. Many different relaxation mechanisms have been discussed for the second regime, and many of them involve spin-orbit interaction [32, 125–132]. Spin-orbit interaction is essential, because this interaction has the potential to couple the spin states of electrons to the orbital states of the quantum dot. The orbital states are sensitive to electric fields, hence electrical fluctuations and other changes of those electric fields, provide a mechanism for energy exchange and hence for spin relaxation. In this context, spin relaxation can occur because spin-orbit interaction couples the electron spin to electrical fluctuations [32, 124, 127, 128]. In GaAs quantum dots the coupling to piezoelectric phonons is considered to be the dominant relaxation mechanism for high magnetic fields. For low magnetic fields, other relaxation mechanisms are expected do be of greater importance, e.g. electrical fluctuations induced by gates or ohmic leads [125, 126]. Since different relaxation mechanisms exhibit a different B-field dependence, one can distinguish them experimentally.

Experiments aiming at measuring the spin relaxation rate are challenging for several reasons. In the regime of low magnetic fields, E_Z is small and finally gets comparable to the thermal energy $k_B T_e$. Consequently, one can no longer discriminate between spin-up and spin-down states, hence rendering spin relaxation measurements impos-

sible. The obvious approach is to reduce the electron temperature in the system as much as possible, in order to make spin relaxation measurements at low magnetic field accessible. However, realizing very low electron temperatures is difficult and requires sophisticated filtering techniques, and an experimental setup that is separated from the environment as good as possible. (Completely new approaches are given in [133, 134].)

Another difficulty in measuring spin relaxation times is the strong B-field dependence, which leads to changes over several orders of magnitude. However, if T_1^{-1} varies over several orders of magnitude, the experimental setup has to provide the according range and resolution. It is very challenging to realize a real-time measurement setup which fulfills these requirements. Furthermore, options for filtering are limited, because filtering reduces the rise time of the system (see chapter 3). Consequently, it is difficult to combine both requirements, low electron temperatures and the necessary dynamic range of the real-time setup. Additional difficulties such as electrical noise (discussed in chapter 3) further complicate the situation.

Spin relaxation rates were measured in different experiments before, for single electrons, as well as for the singlet-triplet system and for a wide range of magnetic fields. In these experiments many findings help to further understand the physics of spin relaxation. The motivation for the experiment performed in this work, is to learn more about the role of spin-orbit interaction in GaAs quantum dots. Spin-orbit interaction in GaAs systems is very interesting, but also quite complicated. There are different contributions to the spin-orbit interaction, like the *Rashba-* and *Dresselhaus* term, which arise from the lack of inversion symmetry of the heterostructure and the lack of an inversion symmetry of the zincblende crystal structure of GaAs. In the presence of Rashba and/or Dresselhaus spin-orbit interaction, the spin relaxation time is expected to be anisotropic with respect to the spatial orientation of a in-plane magnetic field [132]. Consequently, the spin relaxation mechanism mediated via the spin-orbit interaction is expected to show a pronounced angle dependence. Investigating the angle dependence of the spin relaxation by rotating the sample with respect to an in-plane magnetic field, is the main motivation of this experiment. In chapter 4 the effect of spin-dependent tunneling is discussed. There it is stressed that spin-orbit interaction might be involved in this effect as well. If this is the case, the effect of spin-dependent tunneling is expected to show a angle dependence as well. Investigating this effect and finding out more about its nature is an additional motivation for the experiments presented here.

7.2. Spin Relaxation in GaAs Quantum Dots

In the previous section, the important role of spin-orbit interaction in the context of spin relaxation is pointed out. Spin-orbit interaction (SOI) is a relativistic effect, which originates from the presence of intrinsic electric fields **E** in the AlGaAs/GaAs heterostructure and the motion of electrons though these fields. In the rest frame of an electron this intrinsic electric fields transform to magnetic fields **B** [135]

$$\mathbf{B} = \frac{1}{m_e^* c^2}\ \mathbf{p} \times \mathbf{E}, \tag{7.1}$$

where **p** is the electron's momentum and m_e^* refers to the effective electron mass. These magnetic fields then interact with the spin of the electron, i.e. the electron's spin orientates with respect to the magnetic field, such that energy is minimized. From Equation 7.1 one realizes immediately the momentum dependence of the internal magnetic field **B**. However, the electron's momentum is also related to its orbital state, hence spin state and orbital state are coupled via their common momentum dependence. The according Hamiltonian is given by [136]:

$$\mathbf{H} = \frac{g\mu_B}{\hbar}\ \mathbf{B} \cdot \mathbf{S}, \tag{7.2}$$

where $\mathbf{S} = \frac{\hbar}{2}\boldsymbol{\sigma}$ is the spin operator with the *Pauli matrices* σ_i, μ_B denotes the *Bohr Magneton* and g the electron g-factor.

There are two different kinds of intrinsic electric fields in the AlGaAs/GaAs heterostructure, which have to be considered here. Semiconductor samples based on GaAs posses bulk inversion asymmetry (BIA) due to the zincblende structure of the underlying GaAs crystal. Consequently, there are crystal axes along which there is a non-vanishing electric field. Therefore, spin-orbit interaction is present along this crystal axis. Spin-orbit interaction originating from bulk inversion asymmetry is also known as *Dresselhaus* contribution. The Dresselahus term of SOI is described by the following Hamiltonian [137, 138]:

$$\mathbf{H}_D = \gamma \left[\sigma_x p_x \left(p_y^2 - p_z^2\right) + \sigma_y p_y \left(p_z^2 - p_x^2\right) + \sigma_z p_z \left(p_x^2 - p_y^2\right)\right] \tag{7.3}$$

In this equation σ_i denote the Pauli matrices, p_i the components of the momentum operator and the factor γ the strength of the Dresselhaus contribution to SOI. Note, that the coordinate system aligned along the main crystal axes of the GaAs system, i.e. the [100], [010] and [001] directions. For a 2DEG confined to the x-y plane, the expectation value for the z-component of momentum vector vanishes, $\langle p_z \rangle = 0$, while

$\langle p_z^2 \rangle \neq 0$ [20]. Hence, Equation 7.3 simplifies to:

$$\mathbf{H}_D^{2DEG} = \beta \left(p_y \sigma_y - p_x \sigma_x \right) + \gamma \left(\sigma_x p_x p_y^2 - \sigma_y p_y p_x^2 \right) \tag{7.4}$$

Due to their momentum dependence, the first term of this equation is called *linear Dresselhaus* term and its strength is given by the factor β (which depends on band structure parameters and the thickness of the electron gas in growth direction [4]), while the second term is referred to as the *cubic Dresselhaus term*. Typically, the linear Dresselhaus term dominates in low density 2DEGs, hence the cubic term is neglected in the following [32].

The second kind of intrinsic electric field originates from structural inversion asymmetry (SIA), a consequence of the asymmetric confinement potential of the system. The contribution to spin-orbit interaction from SIA is the *Rasbha term* [139]. In the coordinate system of the main crystal axes it can be written as:

$$\mathbf{H}_R = \alpha \left(p_x \sigma_y - p_y \sigma_x \right) \tag{7.5}$$

Here, the factor α is known as *Rashba coefficient* and denotes the strength of this contribution to SOI. Combining the Rashba- and linear Dresselhaus terms of SOI gives the spin-orbit Hamiltonian

$$\mathbf{H}_{SOI} = \alpha \left(p_x \sigma_y - p_y \sigma_x \right) + \beta \left(p_y \sigma_y - p_x \sigma_x \right), \tag{7.6}$$

with respect to the main crystal axes of the GaAs heterostructure. Figure 7.1 illustrates the action of both contributions to spin-orbit interaction. Depending on the direction of motion and the size of the coefficients α and β, both terms can add up, subtract or even cancel each other. As a direct consequence, spin relaxation due to SOI is anisotropic [132]. This anisotropy can be studied by rotating the investigated sample with respect to the in-plane magnetic field. Additionally, it is of interest to vary the coefficients α and β in order to minimize the resulting SOI, which leads to enhanced spin relaxation times. Tuning β is difficult since this would require to add strain to the crystal in order to vary the intrinsic electric field originating from the crystal structure. However, in quantum well structures it is possible to vary the Rashba coefficient e.g. by tilting the confinement potential with the help of a back-gate (or a top-gate).

Spin-orbit interaction is of great relevance for spin relaxation, because without SOI the electrons in a quantum dot are not able to exchange energy with the environment. It was already stress that phonons, especially piezoelectric phonons, provide the dominate energy exchange mechanism. However, phonons only couple different orbital sates

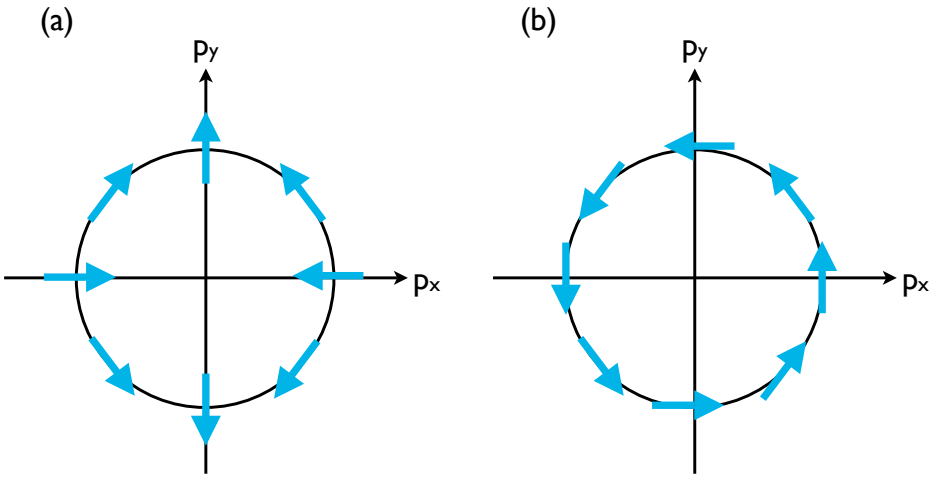

Figure 7.1.: Illustration of spin-orbit coupling: Electrons traveling trough a GaAs crystal with momentum **p** experience an interaction between their spin and the apparent magnetic fields present in the electron's rest frame. (a) Field orientation seen by the electron due to the linear Dresselhaus SOI. (b) Field orientation due to the Rashba contribution to SOI [20].

to each other, but they do not couple different spin states. The role of SOI is to provide the coupling between orbital states and spin states. More precisely, SOI couples the ground spin state to the excited orbital state and vice versa [54, 124]. Only because of this coupling between spin states and orbital stats through SOI, phonons are able to mediate spin relaxation. Let $|g\rangle$ and $\langle e|$ be orbital ground and excited state which are separated in energy by $\hbar\omega_0$. Let further $|\uparrow\rangle$ and $\langle\downarrow|$ denote the spin-up and spin-down states, then one can use perturbation theory to calculate the admixture $E_\pm$ of both kinds of states by

$$E_+ = \frac{\langle e\downarrow|\hat{H}_{SOI}|g\uparrow\rangle}{\hbar\omega_0 + E_Z}, \quad E_- = \frac{\langle e\uparrow|\hat{H}_{SOI}|g\downarrow\rangle}{\hbar\omega_0 - E_Z}, \tag{7.7}$$

where $\hat{H}_{SOI}$ is the spin-orbit Hamiltonian and E_Z the Zeeman energy [20]. The process of relaxation is described by the transition between perturbed state, i.e. from $(|g\downarrow\rangle + E_-|e\uparrow\rangle)$ to $(|g\uparrow\rangle + E_+|e\downarrow\rangle)$. A detailed calculation of the according matrix elements can be found in [54] and [20]. The spin relaxation rate is then calculated to:

$$T_1^{-1} = A\frac{B^5}{\lambda_{SOI}^2(\hbar\omega_0)^4} \tag{7.8}$$

Here, $\hbar\omega_0$ is the energy of the excited orbital state, B the magnetic field, A a parameter depending on the g-factor and phonon specific parameters. $\lambda_{SOI} = \hbar/(m^*(\beta - \alpha))$ denotes the spin-orbit length which gives a length scale for the distance an electron travels in the material until its spin is rotated by an angle of $\phi = 2\,\text{rad}$.

7.3. Spin Relaxation Time Measurements

The sample used for measuring spin relaxation times is the same as was used to investigate thermally activated, metastable charge state switching (see chapter 5). While previously the sample was tuned into the double dot regime, it is now for practical reasons operated as single quantum dot. For the spin relaxation time measurements it is necessary to realize an asymmetric coupling to source an drain, i.e. tunneling is only possible to one lead. Hence, the coupling to the other lead is reduced until tunneling to this electron reservoir can be neglected. This situation is illustrated in Figure 7.4 (a). Here the red arrow indicates to which lead electron tunneling takes place. The same graphic also depicts the orientation of the nanostructure with respect to the crystal axis (green coordinate system) and the direction of the external magnetic field (white arrow). The magnetic field is applied in-plane of the wafer and for all measurements presented here, it points along the direction indicated in Figure 7.4 (a). The misalignment of the in-plane B field is about 2 degrees, which was determined by a *van der Pauw* measurement. Further, the two gates used for applying voltage pulses are highlighted (blue). The *right-hand gate* of the quantum dot (see Figure 7.4) is required to load and unload electrons to the QD, while the other gate defines the plunger gate of the sensor quantum dot. The voltage pulses applied to the SQD's plunger gate are compensating for the capcitive coupling to the *right-hand gate* and thereby stabilize the SQD at the optimal operation point.

Spin relaxation time measurements, are performed by applying a three-step pulsing scheme which is similar to the one described by Amasha *et al.* [54]. The three-step pulsing scheme and its mode of operation are depicted in Figure 7.2. In the first step of the measurement scheme, the QD is completely ionized, i.e. there is no electron remaining on the dot. In this configuration both spin states are above the chemical potential in the electron reservoir. In the second stage of the pulsing scheme, a voltage pulse pulls both spin states below the chemical potential. Both empty states are now available, such that an electron tunnels on the QD. During this load stage, either the spin-up or the spin-down state of the QD gets occupied. An electron tunneling into the ground state will remain there, while an electron in the excited spin state relaxes to the ground state with a rate T_1^{-1}. In the following, the tunneling rates into the spin-up and spin-down state are denoted with Γ_e for the excited - and Γ_g for the ground spin state. In the final stage of the pulsing scheme, the read-out configuration of the system is entered. Here, the excited spin state is positioned above the chemical potential in the leads, while the ground spin-state still lies below the chemical potential. In this configuration only electron in the excited spin state can tunnel off the QD, while tunneling off from the ground state is suppressed exponentially.

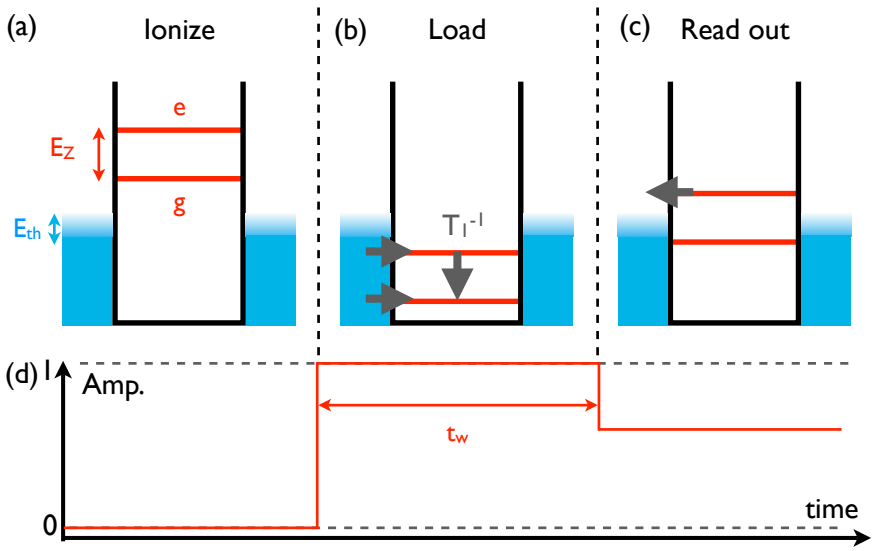

Figure 7.2.: Illustration of the three-step pulsing scheme used for spin relaxation time measurement: (a)-(c) Depict the position of the excited- and the ground spin state with respect to the chemical potential in the leads for all three stages of the pulsing scheme as described in the main text. Gray arrows indicate possibilities for electron tunneling and relaxation (marked with T_1^{-1}). (d) Illustrates the form of the actual voltage pulse applied to realize the measurement scheme. The amplitude of the pulse shown is normalized with zero corresponding to the ionization stage and 1 to the load stage. The length of the load-stage, t_w is varied in the experiment.

The pulse amplitude of all three stages is fixed as well as the length of the ionization and the read-out stage. The parameter that is changed experimentally is the length of the load stage, t_w. In the read-out stage, only electrons still remaining in the excited spin state can tunnel off the QD, and those tunneling events are detected with the nearby charge sensor. The distribution of the detected tunneling events as a function of the wait time t_w is the main result of the measurement and can be used to extract spin relaxation times.

Exemplary data traces are shown in Figure 7.3. In panel (a), three succeeding pulse cycles are depicted. In addition to the actual data (blue), an overlay of the corresponding pulsing scheme is shown in red. The lowest level corresponds to the ionization stage, analogue to the illustration in Figure 7.2. When entering the ionization stage, the electron quickly tunnels off (see Figure 7.3), leaving an empty quantum dot. In the subsequent load stage (the stage with the highest amplitude in the pulsing scheme), an electron tunnels on the QD after a time t_0. In the final read-out stage, the charge sensor detects whether or not there is still an electron present in the excited state, as soon as this electron tunnels off the dot. In Figure 7.3 only in one of the three depicted read-out stages an tunneling event is detected. In the first and third one, there are no events, although an electron entered the QD during the according load stage. There-

fore, one concludes that in these two cases the electron either tunneled into the ground spin state, or relaxed to the ground state before the read-out stage was entered. The situation depicted in panel (b) of Figure 7.3 is similar, but here the detected tunneling event occurs much later in the read-out stage than in data shown in panel (a). As will be discussed in more detail in the following, events like this are very likely not due to tunneling from the excited spin state. Instead, they are caused by electron tunneling from the ground state. Although tunneling off the ground state is suppressed exponentially, there is still a non-zero probability for such events, that depends on the relation between Zeeman energy E_Z and thermal energy $k_B T_e$ and the exact position of the ground state with respect to the chemical potential. Spin relaxation time measurements require sufficient statistics, hence several thousand[1] pulse cycles are performed for every value of the wait time t_w. Analyzing the data requires counting the number of detected relaxation events as a function of t_w. Figure 7.4 (b)-(d) depicts the result of a spin relaxation time measurements at a magnetic field of 4 T. Figure 7.4 (b) shows the number of events, where an electron enters the QD during the load stage of the experiment. Since tunneling on the QD requires an average time that is proportional to Γ_{on}, there are pulse cycles where no electron enters the QD during the load stage. As can be seen from Figure 7.4 (b), the load efficiency (the number of pulse cycles where an electron tunnels on the QD divided by the overall number of performed pulse cycles) is small for short t_w intervals, and approaches 100% for longer intervals. Only in case the charge sensor detects an electron tunneling on the QD during the load stage, the according read-out stage of the pulse cycle is analyzed. The load efficiency is given by the function $N_0(1 - exp(-\Gamma_{on} \cdot (t - t_0)))$, where N_0 denotes the total number of performed pulse cycles and $\Gamma_{on} = \Gamma_e + \Gamma_g$ the total tunneling rate into the dot, Γ_g and Γ_e are tunneling rates into ground state and excited state, respectively [54]. Fitting this function to the data in Figure 7.4 (b) gives $\Gamma_{on} = 292.3 \pm 0.8\,\mathrm{Hz}$.

Analyzing the read-out stages for the pulse cycles, where an electron was successfully loaded onto the QD during the load stage, gives the probability to have an excited spin-state as a function of t_w. These events are distributed according to

$$P_e(t_w) = a + \frac{b}{\Gamma_{on} - R}\left(e^{-Rt_w} - e^{-\Gamma_{on} t_w}\right), \tag{7.9}$$

where $R = T_1^{-1}$ is the spin relaxation rate, $\Gamma_{on} = \Gamma_e + \Gamma_g$ the overall tunneling rate obtained from the load efficiency. A detailed derivation of this formula can be found in [54]. Figure 7.4 (c) depicts the result of a spin relaxation time measurement at a magnetic field of 4 T. In Addition, Equation 7.9 is fitted to the data. Although fitting

[1] Abut 65000 pulse cycles for up to 20 different t_w values are performed within a measurement period of two days.

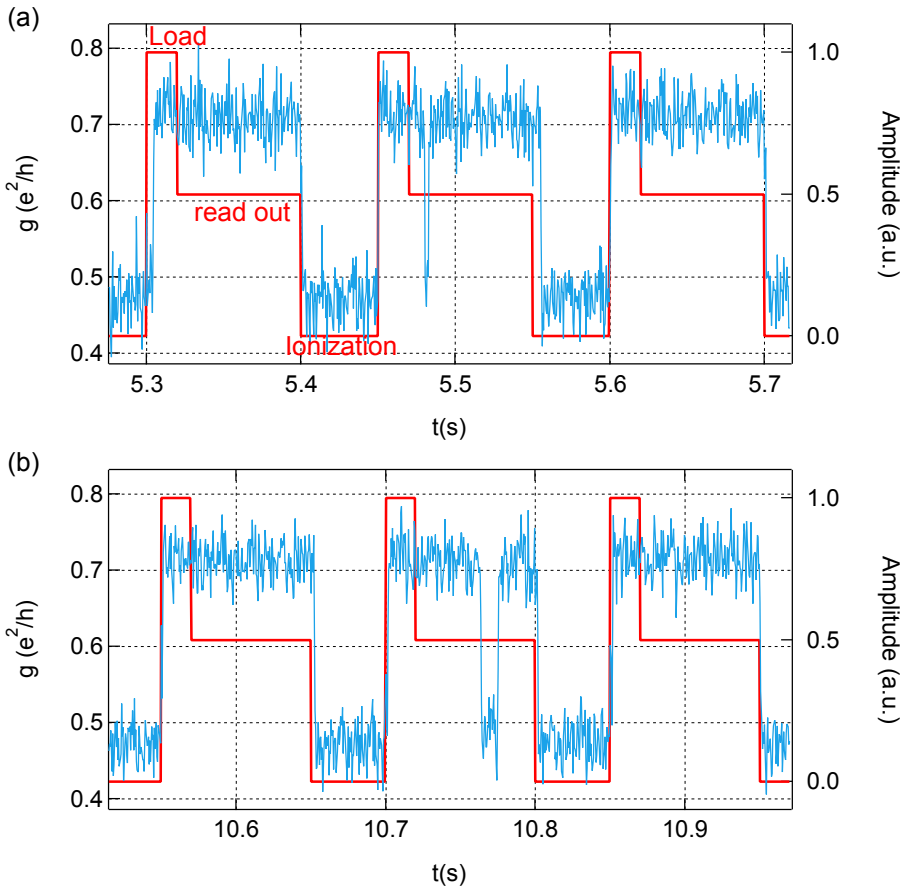

Figure 7.3.: Spin relaxation time measurement: (a) Three successive pulse cycles are depicted (blue data) together with an overlay of the according pulse scheme (red). The lowest level corresponds to the ionization stage, while for the highest level the system is in the load-configuration and the read-out stage lies in-between. For all three pulse cycles the dot is completely emptied during the ionization stage. During the load stage an electron tunnels on the QD, either into the excited or into the ground spin state. Only in the pulse cycle depicted in the center of this panel, the charge sensor detects an electron leaving the QD during the read-out stage. Afterwards another electron tunnels into the ground state of the QD very quickly. (b) Same situation as in (a), but the event is detected close to the end of the read-out stage. Such events can either hint towards a long relaxation time, or towards are background tunneling rate, where electrons in the ground spin state of the QD tunnel into the electron reservoir. This data was taken at $B = 4\,\mathrm{T}$, with 0.5 ms resolution and the background tunneling rate was determined to be $0.115 \pm 0.003\,\mathrm{Hz}$ (see. Figure 7.5).

this function to the data shown in Figure 7.4 (c) is possible, the distribution of detected events does not decrease down to zero for longer t_w intervals. This fact is interpreted as a background tunneling rate, where electrons from the ground spin state are tunneling into the electron reservoir. This interpretation is supported by Figure 7.4 (d), where the same data set as in (c) is analyzed, but only events detected in the first 10 ms of the read-out stage (80 ms total length) are taken into account. Now the number of events due to a background rate is reduced considerably and the agreement between data and fit is much better than for the analysis shown in Figure 7.4 (c). From the fit displayed in Figure 7.4 (d) a spin relaxation time of 1.9 ± 0.1 ms is extracted. This procedure does not alter the peak position (see. Figure 7.4) of the detected tunneling events and is only reducing the level of background events. Figure 7.5 shows the Spin Relaxation time T_1 extracted for different lengths of the evaluated section of the read-out stage. Here one can see that the Spin Relaxation times extracted from fitting Equation 7.9 is almost constant. Only for very short evaluation sections the extracted Spin Relaxation time decreased due to the effects/alterations created by this evaluation procedure on $P_e(t_w)$. Further, for higher evaluation sections converging towards the full length of the read-out stage, the uncertainty of the extracted values increases (see error bars in Figure 7.5). In addition to the T_1 data, Figure 7.5 also depicts the number of background events as a function of the evaluated section of the read-out stage. This data set allows to determine a background tunneling rate Γ_{bg} of 0.115 ± 0.003 Hz. This background tunneling rate is rather small and hence only a small number of background events is detected in the data. However, the number of events originating from electrons tunneling off the excited state is also small, i.e. comparable or smaller than the the number of background events. The small number of such events can be explained by the the short relaxation, compared to the time resolution that could be realized for this measurement and still had a sufficient SNR to successfully evaluate the data. Another possible explanation is the suppressed tunneling rate into the excited spin state, as it was observed in Figure 4.9. However, the visibility at 4 T previously was determined to be $\chi = 0.83$, which makes this explanation less likely, unless χ has change between this measurement and the previous one.

As stressed before, tunneling from the ground spin state to the electron reservoir is assumed to be suppressed exponentially, since in the read-out stage this level is positioned below the chemical potential. The strength of this exponential suppression then depends on how far in energy this level lies below the chemical potential. The illustration of the read-out stage in Figure 7.2 depicts a situation, where excited spin state and ground spin state are positioned such that the chemical potential lies exactly in the center between them. The experimental realization of the read-outs stage is different from this illustration. Due to the high background rate present in the data,

the Zeeman levels where lowered in energy, such that the chemical potential is closer to the excited spin state. This procedure ensures a further suppression of tunneling from the ground spin state. The data depicted in Figure 7.4 (c) and (d) was taken with this optimized positioning of the read-out stage. From various tests and other experiments

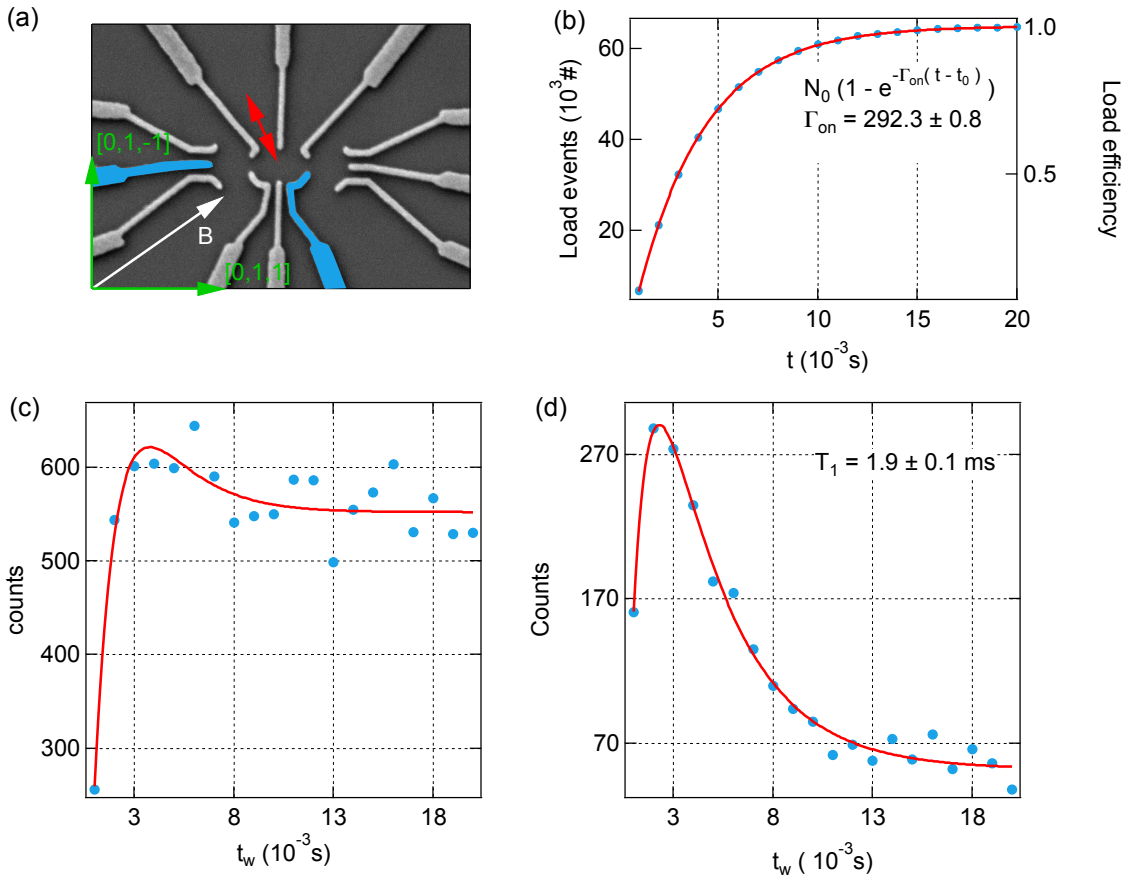

Figure 7.4.: (a) SEM pictured of the device used to perform spin relaxation time measurements in the single dot regime. A red arrow indicates to which lead electron tunneling is possible. Tunneling to the other lead is made negligibly small. Blue marked structures indicate gates that are used for pulsing. The green coordinate system illustrates the orientation of the nanostructure with respect to the crystal axes and a withe arrow indicates the direction of the magnetic field. (b) Number of detected load events as a function of t_w. Right axis shows the same date set, but normalized to the total number of performed pulse cycles (load efficiency). (c) and (d) show the number of tunneling events detected during read-out, as discussed in the main text.

involving the same pulsing technique/setup, it can be ruled out that minor fluctuations of the pulse amplitude lead to a significant offset or shift in the level alignment. From the data depicted in Figure 4.8 one can see, that already at a magnetic field of 3 T it is difficult to resolve the Zeeman splitting. This is very likely due to thermal broadening, i.e. the condition $E_Z \gg k_B T_e$ is no longer fulfilled. Consequently, the background rate observed in the spin relaxation time measurement at 4 T, might be caused by this effect

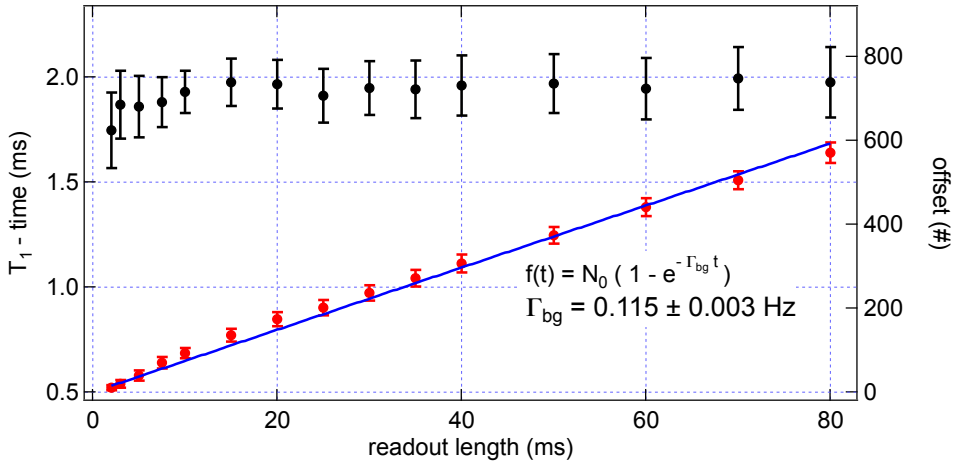

Figure 7.5.: Spin Relaxation time T_1 extracted for different lengths of the evaluated section of the read-out stage. The extracted T_1 is always around 2 ms, independent of the respective evaluations section, since the peak position is not altered by this procedure (see Figure 7.4 (c) and (d)). For long evaluations section the uncertainty of the extracted values increases due to the increased influence of the background. In addition, the number of background tunneling events for the respective length of the evaluated section is displayed as well. From this data one can determine the background tunneling rate Γ_{bg}. Note, that this fit is only possible because the amplitude $N_0 = 65000$ is known, since this is the total number of performed pulse cycles and hence represents the maximum number of detectable events.

as well. Indeed, spin relaxation time measurements at lower magnetic field turned out to be impossible due to a further increased background rate.

Measuring spin relaxation times at higher magnetic fields requires the ability to measure with a higher time resolution than what was used for the data shown in Figure 7.4. Since the theoretical bandwidth of the real-time setup allows for much faster measurements, it is possible to measure T_1 for higher magnetic fields, which is part of ongoing experiments.

7.4. Discussion and Outlook

The data presented in the previous section demonstrates the successful implementation of spin relaxation time measurements on a measurement setup, which in the beginning of this PhD thesis neither was equipped for real-time measurements, nor for pulsing techniques. Figure 7.3 demonstrates the successful implementation of the pulsing scheme required for spin relaxation time measurements. The obtained data can be fully understood and is completely consistent with intended operations on the QD levels. Further, the capacity to analyze the data, including extracting spin relaxation times is demonstrated as well. Figure 7.4 (c) shows the presence of a background tunneling

rate originating from electrons in the ground spins state of the QD. However, the analysis presented in Figure 7.3 (d) demonstrates how a modified evaluation procedure can improve the situation. Hence, spin relaxation time measurements are in principle possible in the regime of magnetic fields below 4 T. With increased measurement periods together with technical improvements[2], the setup definitely has the potential to allow for measurements in this range of magnetic fields.

The data concerning the Zeeman splitting, which are presented in chapter 4, also demonstrate the accessibility of high magnetic fields for spin relaxation time measurements. For high magnetic fields, the background rate due to tunneling from the ground spin state is expected to be of less importance, since here the ground spin state can be positioned further below the chemical potential, which leads to additional suppression of the background rate. In addition, there is the immediate possibility to study the visibility of the Zeeman splitting as a function of the orientation of the sample with respect to the magnetic field. The data presented in chapter 4 already shows a variation of the visibility of the Zeeman splitting as function of B. Consequently, the next step could involve a study of the possible angle dependence, i.e. whether or not the visibility of the Zeeman splitting depends on the orientation of the magnetic field with respect to the crystal axis of the wafer material.

All requirements to study the anisotropy of spin relaxation in GaAs are met as well. In addition it is possible to do this study for a wide range of magnetic fields. In subsequent experiments on the now fully functional real-time setup and with the same sample that was already used in this work, it should be possible to produce first results on the angle dependence of spin relaxation time in the near future.

[2] At the time the first spin relaxation time measurements were performed, the experimental setup was suffering under increased electrical noise (see also discussion in chapter 3). Further, for unclear reason the electron temperature during the spin relaxation time measurements was 130 mK, while before electron temperatures of about 50 mK were reached.

Chapter 8

Summary and Outlook

In this work, real-time charge sensing techniques are used to detect single electron tunneling in GaAs based lateral quantum dots and double quantum dots. Charge sensing is realized with a sensor quantum dot positioned adjacent to the investigated structures. A relative sensitivity η of up to 100% (and more) is reached with such sensor quantum dots. In combination with room temperature electronics, bandwidths between 3 kHz and 11 kHz are obtained. Despite the high sensitivity of the charge sensor, the measurements described in this thesis are not limited by bandwidth, but by the signal-to-noise ratio. All relevant sources of noise that lead to a reduced signal-to-noise ratio are characterized and it turns out, that noise picked up from external sources and the intrinsic amplifier noise are the dominating contributions. One possible future approach to a improved real-time setup, is to optimize the isolation from the environment. Improved shielding for measurement lines and electronic components, as well as improved filtering of power lines can help to reduce noise pick-up. Amplifier noise can be reduced by using a cryogenic amplifier instead of room temperature devices. This requires modifying the electronics in the dilution refrigerator itself, since such a cryogenic amplifier has to be staged closed to the 1K-Pot in order to obtain temperatures below 4 K (the temperature of liquid helium). Thereby it is also possible to improve the bandwidth of the setup further, since the capacitance of the internal wiring and filtering of the refrigerator can be reduced by this procedure as well. Another possible approach is a more complicated modification of the experimental setup, where the sensor dot is part of an impedance matching circuit. This includes the operation of rf-electronics, which might have negative influence on electron temperature. Further, it is unclear if the used refrigerator provides enough space for the required electric components and if those components can be integrated into the existing piezo-rotator, which is an essential part of the current experiment. Without the rotator system it is not possible to investigate the anisotropy of spin-relaxation with respect to the magnetic field.

All experiments performed in this work, require elaborated software tools for data analysis. It is of special interest to have a very reliable and flexible tool for determining tunneling rates from real-time data. The development and mode of operation of such a software tool is described in detail in this work. In addition to the conventional procedure where intermediate steps of the analysis procedure rely on histogramming and fitting data, another method is presented which allows to directly calculate tunneling rates during data analysis. Thereby it is possible to avoid additional uncertainties of the determined tunneling rate arising from binning and fitting. An additional software tool is described, which creates artificial real-time data simulating the telegraph-noise like signal that corresponds to the experimentally obtained signal for resonantly tunneling electrons. Since tunneling rates, signal-to-noise ratio and rise time are defined as input parameters, this software allows for thorough testing of the analysis algorithm. Further, does this software allow to explore the limitation of data analysis arising from signal-to-noise ratio and bandwidth.

An new intrinsic effect is reported in this thesis - thermally activated metastable charge state switching in a double quantum dot. A detailed experimental analysis of the observations, in combination with an extension of the orthodox model of double quantum dots, allows for the complete understanding of nearly all features of this effect. In the area of the charge stability diagram, where metatsable charge state switching is observed, there is an energy level in both quantum dots that lies below the chemical potential in the electron reservoirs. Only because one of those states always lies lower in energy than the other, there is a well-defined ground state of the double dot system, that defines the charge configuration of the system. Since both energy levels are energetically available, tunneling processes are possible, which involve the electron reservoirs. Therefore, metastable charge state switching occurs as a function of time. The pronounced temperature dependence, as well as the dependence of the switching frequency on the tunnel coupling and inter-dot coupling are captured in great detail in this work. This effect is not limited to a certain electron transition and should be observable in any double quantum dot device at any electron transition. It is stressed how this effect is affecting experiments on spin-qubit, since this charge state switching involves electron exchange with the leads, which e.g. inevitably destroys coherence. It is also argued, how the effect of thermally activated charge state switching can be fully controlled by gate tuning, since it strongly depends on the tunneling rates of the double dot system that can all be controlled via the applied gate voltages. Further work on this effect is necessary in order to explain e.g. the bias dependence. Understanding the observations made here is of great interest, in order to find out whether they are part of the intrinsic effect, or if they arise from a subtle defect of the device,

e.g. the formation of a third electron reservoir. It is also imaginable to use the effect of thermally activated charge state switching to study the coupling of a double quantum dot to a bath. In this case the electron reservoirs would play the role of the according bath and the great advantage would be, that the coupling between this bath and the investigated system can be fully controlled via gate tuning. Finally, current research in the field of spin-qubits is more and more focused on investigating systems consisting of three and more quantum dots. Since the far more complicated charge stability diagrams of such systems are more difficult to understand than that of a double dot, it might be of interest to think about thermally activated charge state switching in these system as well. There is no reason to believe that this effect is limited to double quantum dots, but it is not immediately clear how the presence of an analogue effect would affect these multi-dot systems.

The second major experiment presented in this thesis, is the implementation and realization of spin relaxation time measurements on the previously described real-time setup. Due to the expected anistropy of spin-relaxation with respect to the spatial orientation of an in-plane magnetic field, this experiment is performed in a dilution refrigerator, which features a piezo-rotator. This device allows to rotate the sample with respect to the magnetic field applied in-plane of the wafer material. The successful implementation of the three-step pulsing scheme is demonstrated by performing first spin-relaxation time measurements at a magnetic field of 4 T. Analyzing single real-time traces, corresponding to a complete run of the three-step pulse cycle, reveals that in all three stages of the experiment the observations are consistent with the expectations. In other words, ionization, loading and read-out of the QD work properly and the required tunneling events are detected. The software necessary for data analysis was tested by evaluating these first data sets, which include data from several thousand succeeding pulse cycles. Here, it turns out that data analysis works correctly although the presence of a background rate, which correspond to tunneling from the ground state, leads to complications. At a magnetic field of 4 T a spin relaxation time of 1.9 ± 0.1 ms is extracted, which is in agreement with previously reported results from other experiments [27]. Consequently, the immediate next step is to begin with measurements on the anisotropy of spin relaxation and the visibility of the Zeeman splitting by rotating the sample. For spin relaxation time measurements at lower magnetic fields, the issue of tunneling from the ground spin state affects the experiments more severely. For higher magnetic fields shorter spin relaxation times are expected, hence faster real-time measurements are required. Here the limitations due to signal to noise ratio, i.e. due to electric noise, is the dominating limitation. Both issues have to be addressed, if spin relaxation time measurements over a wide range of magnetic fields are to be made, which is part of ongoing work.

Appendix A

Sample Fabrication

All experiments presented in this thesis, were performed with samples that I fabricated in the clean room facilities at the University of Basel. Sample fabrication is a delicate process, which requires constant optimization and control of numerous process parameters. Therefore, it seems appropriate to state those process parameters here in this appendix, although the sample fabrication in general follows the generic fabrication scheme of semiconductor nanostructures [140].

Sample fabrication is subdivided in five major fabrication steps: Defining and etching the mesa, pattering ohmic contacts, optical lithography of parts of the depletion gates (usually referred to as photo-gates), e-beam lithography to write the nanostructure and finally contacting the sample.

Every run of sample fabrication begins with cutting off a piece of wafer. This step is rather trivial, but the orientation of the nanostructure with respect to the crystal axis is of importance for some of the experiments in this thesis. Throughout this thesis, the sample orientation is such that the x-axis is parallel to the double dot structure and points along the [011] direction of the AlGaAs/GaAs crystal. The y-axis is perpendicular to the device axis and points in the $[01\bar{1}]$ direction of the wafer. All samples used for this thesis were fabrication from wafer material, grown by the Gossard group at UCSB (registration number 060926C). This material has nominally a 2DEG density of $n = 2.64 \cdot 10^{-11}\,\mathrm{cm}^{-2}$ and mobility of $\mu = 3.98 \cdot 10^5\,\frac{\mathrm{cm}^2}{\mathrm{Vs}}$, while the density of the delta-doping layer is $n_\delta = 6 \cdot 10^{-11}\,\mathrm{cm}^{-2}$. The first fabrication step defines the mesa on which the nanostructure will be positioned later on. The 2DEG is present only beneath the mesa structure, while anywhere else the 2DEG is removed from the wafer. This is accomplished by a wet-etching process, which etches the unprotected parts of the wafer's surface. Prior to this step, a protective layer of photo-resist in the shape of the mesa is deposited on the material by means of optical lithography. The mixture used to

etch the wafer, always contains the same amount of sulfuric acid, water and hydrogen peroxide. However, the etching rate depends strongly on temperature and is influenced even by small deviations of the H_2SO_4 concentration. Therefore, the etch rate has to be determined, every time a new sample is fabricated. This is done by measuring the surface profile of the etched samples with an alpha-stepper. The unprotected surface of the wafer should be etched away at least down to the depth of the 2DEG.

Parameters: Mesa	
3 solvent clean	tce, acetone, methanol, each 5 min ultrasonic, dry with N_2
Dehydrate	5 min on hotplate at 120 ℃, cool down 2 min
Inspection	optical microscope
Spin photoresist	Ma-N 415, parameters 6000:5:40 $\Rightarrow$ layer $\approx 1.6\,\mu$m
Inspection	optical microscope
Bake	90 sec at 90 ℃
Expose	14 s, hard contact (5 s)
Develop	1 min in maD 332s, rinse in DI H_2O, dry with N_2
Measure profile	α-stepper
Etch Mesa	$H_2O : H_2SO_4 : H_2O_2 = 480 : 2 : 16$, etch 150 nm, DI H_2O, N_2
Inspection	measure profile with α-stepper again
Remove resist	put sample in NMP/(mr-Rem660) at $45 - 50$ ℃, IPA, N_2
Inspection	optical microscope
O_2-Plasma	40 s bei 250 mTorr pressure and 30 W power (16% oxygen)

Table A.1.: Process parameters - mesa

The photo-resist is then removed again and the sample is cleaned, before continuing the sample fabrication. Table A.1 summarizes all relevant process parameters of the mesa-step.

After finishing the mesa, ohmic contacts and the bases of the depletion gates are patterned in a second step (see Figure A.1). Ohmic contacts are required to contact the 2DEG beneath the surface of the mesa, while the bases of the depletion gates are later on needed to define the actual nanostructure. The difference is that ohmic contacts will lie on the mesa, i.e. there will be 2DEG beneath them, while the bases of the depletion gates are placed outside of the mesa. This fabrication step also includes optical lithography in order to deposit a AuGe-eutectic on the positions where ohmic contacts shall result. The advantage of using a AuGe-eutectic is the lower melting point compared to the melting points of its components. The following annealing step produces the electric connection between the surface of the ohmic contacts and the 2DEG.

This process is delicate and not fully understood and some of the resulting chemical- and physical properties are only obtained through empiric recipes. Consequently, prior

Parameters: Ohmic contacts	
3 solvent clean	tce, acetone, methanol, each 5 min sonicator, N_2
Dehydrate	5 min on hotplate at 120 °C, let cool down 2 min
Spin photoresist	Ma-N 415, Parameters 6000:5:40
Inspection	optical microscope
Bake	90 sec at 90 °C
Inspection	optical microscope
Align and Expose	14 s, hard contact (5 s)
Develop	1 min in maD 332s, rinse in DI H_2O, dry with N_2
Inspection	optical microscope
O_2-Plasma	40 s bei 250 mTorr pressure and 30 W (16% oxygen)
HCL-Dip	5 s, rinse with DI H_2O, dry with N_2 (37% HCL)
Evaporate	deposit 204 nm AuGe, 53 nm Pt (cool with LN_2)
Lift off	warm NMP (at least 15 min) at 45 $-$ 50 °C, dry with N_2
Annealing	at 370 °C for 120s, at 450 °C for 60s in Ar:H_2=95:5 gas

Table A.2.: Process parameters - ohmic contacts

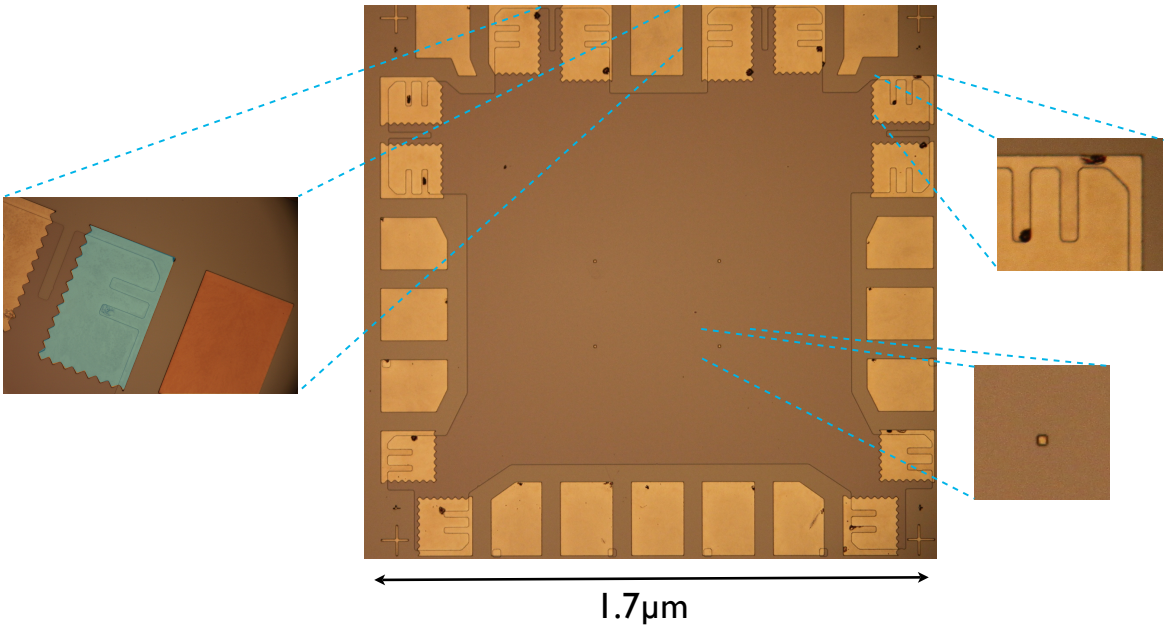

Figure A.1.: Photograph of a sample after mesa and ohmic contacts were patterned. The main photograph in the center depicts the the complete mesa structure (dark brown structure in the background), which is approximately 1.7 μm wide. The golden structures are ohmic contacts and the bases of the yet missing depletion gates. The left zoom-in shows a close up of an ohmic contact (artificially blue shaded) and a base of a depletion gate (artificially red shaded). The upper right zoom-in of an ohmic contact shows dark structures, that emerge after annealing, and are probably caused by the diffusion process. The lower right zoom-in shows one of four markers on the mesa used to position the e-beam structure with respect to ohmic contacts and depletion gates.

to the first run of sample fabrication, an empiric recipe had to be tested and optimized. In this process, I succeeded in reducing the resulting electric resistance of the produced ohmic contacts from a couple of kΩ down to a average of $R \approx 50\,\Omega$ at 4 K. Alongside the ohmic contacts, this process step is also used to define four markers on top of the mesa, which define the corners of a square and are used for alignment during the following electron-beam lithography. Those markers are shown in Figure A.1 together with the ohmic contacts and the aforementioned bases of the depletion gates. An overview of the most relevant process parameters is given in Table A.2.

The nanostructure is the most important part of the sample. Consequently, the e-beam lithography step used to pattern it should be carried out very thoroughly and with the uttermost precision and prudence. The nanostructures of the devices used here, were fabricated in a two-step procedure, that requires the usage of two different write-fields of the SEM. However, only in the bigger write field there are markers present, which allow to orientate on the device and prevent unwanted rotation- and magnification artifacts. During the first step of e-beam lithography, these markers are used to perform the correct write field alignment.

Afterwards, the resulting correction parameters have to be used to manually calculate the correpsonding corrections for the smaller write field. The required transformation factors can be calculated from the default parameters for the two write fields used. The process parameters for e-beam lithography are listed in Table A.3, while Figure A.2 shows a completely processed sample.

Parameters: e-beam lithography	
3 solvent clean	tce, acetone, methanol, each 5 min ultrasonic, N_2
Dehydrate	5 min on hotplate at 120 °C, let cool down 2 min
Spin photoresist	PMMA, Parameters 4000:5:40 ⇒ layer ≈ 120 nm
Inspection	optical microscope
Bake	7 min at 180 °C
Inspection	optical microscope
Align and Expose	REM, use dose from prior dose tests
Develop	85 s in (IPA:MIBK):MEK=100:1.3, stop with IPA, rinse
Inspection	optical microscope
Evaporate	deposit 5 nm Ti, 15 nm Au
Lift off	acetone, clean with IPA and dry with N_2

Table A.3.: Process parameters - ohmic contacts

After a successful e-beam lithography, the nanostructure has to be completed by adding the bigger structures of the depletion gates. Additionally one has to add bond pads at the ends of the depletion gates and on top of the previously defined bases of the depletion gates. Those bond pads also have to be added on top of the ohmic contacts.

At the end of the fabrication process, these bond pads will be used to connect the individual structures of the sample with the contacts on the chip carrier. Those are finally connected to the room temperature measurement electronics. This fabrication step also requires optical lithography, an overview of process parameter can be seen in Table A.4, while the finished structures are subject of Figure A.2.

Parameters: Gates and Leads	
3 solvent clean	acetone and methanol but without aonicator
Dehydrate	5 min on hotplate at 120 °C, let cool down 2 min
Spin photoresist	Ma-N 415, Parameters 6000:5:40
Inspection	optical microscope
Bake	90 sec at 90 °C
Inspection	optical microscope
Align and Expose	14 s, hard contact (5 s)
Develop	1 min in maD 332s, rinse in DI H_2O, dry with N_2
Inspection	optical microscope
O_2-Plasma	40 s bei 250 mTorr pressure and 30 W (16% oxygen)
Evaporate	deposit 5 nm Ti, 100 nm Au
Lift off	warm NMP (at least 15 min) at $45 - 50$ °C, dry with N_2

Table A.4.: Process parameters - gates and leads

Finally, the finished sample has to be glued into a chip carrier. Au-wires of 32 μm diameter are used to connect the bond pads with the pins of the chip carrier. Bonding is a delicate process as well, that depends on various parameters. Therefore, every time a sample is to be bonded, the respective parameters have to be optimized. Table A.5 displays bonding parameters, which represent a starting point for further optimization. Finally, Figure A.3 shows a SEM pictograph of a completely processed sample, which was already glued into a chip carrier and bonded.

Bonds Parameters (Au wires with 32 μm ∅, 90 °C)						
-	**search**	**power**	**time**	**force**	**loop**	2.3-3.5
Bond 1	0.5	3.2	4.7	2.9	**tail**	1.5
Bond 2	0.5	1.9	5.1	3.0	**tear**	3.3

Table A.5.: Process parameters - bonding

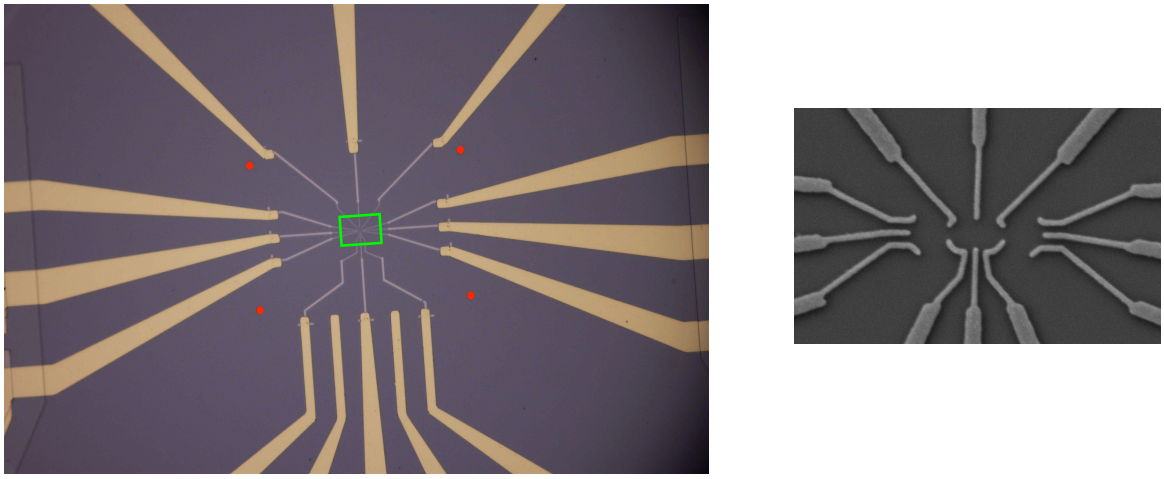

Figure A.2.: Photograph of a sample after finishing photo-gate- and e-beam step. Golden lines on top of the mesa (dark region in the background) are the parts of the depletion gates, that were patterned by optical lithography. Those so called photo-gates converge at the center of the mesa, where the part of the nanostructure lies, that has to be written with e-beam lithography. The red dots indicate the position of the four markers used for orientation. The right SEM picture depicts the central region of the sample, indicated by the green frame in the main graph.

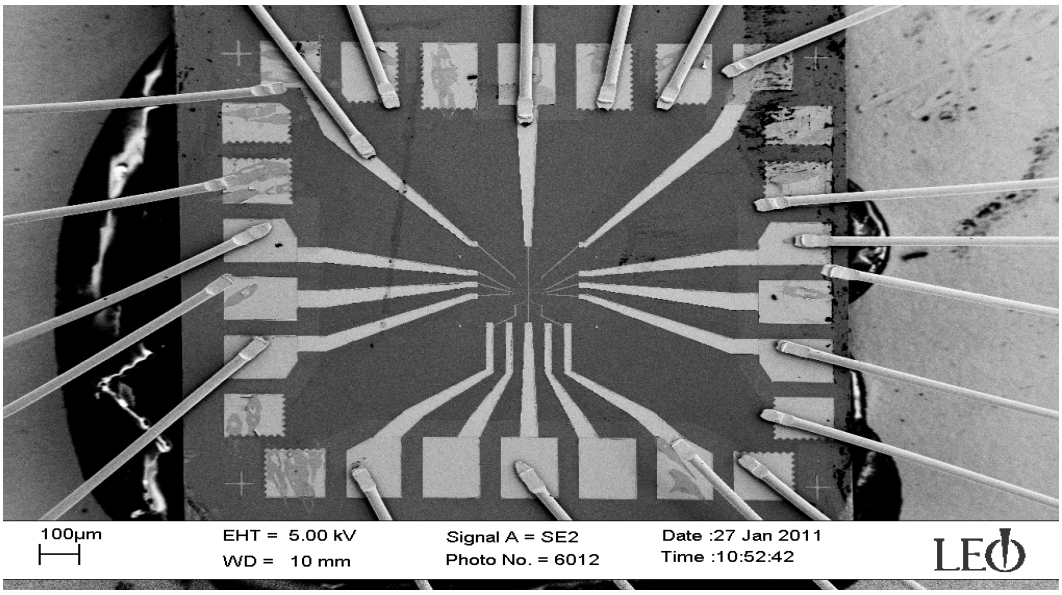

Figure A.3.: SEM pictograph of a finished sample. The hole sample is glued into a chip carrier (dark blob in the background is glue and the gray shaded background is the actual chip carrier). Additionally, one can see bonds connected to the sample bond pads, reaching out for the connectors on the chip carrier. Some of the bonds shown here, have disassociated from the bond pads again.

Appendix B

Experimental Methods

Many experiments would not be possible without certain tools and techniques, which are either developed prior or in parallel to the actual experiment or include standard methods, that are described in literature. Although these tools and techniques often seem trivial, they can still be of great importance, since they are either required to determine important experimental parameters, e.g. lever arms, or help editing and interpreting data. In this appendix some of the most important of these experimental methods are described briefly, alongside an illustration of their functionality, or exemplary data. The first section of this appendix treats the tool used to subtract a background from raw data. This tool was mentioned several times in the main text of this work, but the mode of operations was not explained. Here, the background subtraction tool is explained in detail, since this program is very versatile and simplifies data interpretation considerably by revealing measurement details, which were hardly visible before.

Another important tool, which is essential for the functionality of charge sensing, is the linear feedback mechanism used to compensate for the capcitive coupling between sensor quantum dot and double quantum dot. Without this tool, it is difficult to obtain a stable sensor sensitivity. Hence, the quality of the obtained data depends strongly on the functionality of this feedback mechanism, which is described in the second section of this chapter.

Determining lever arms and electron temperatures is often essential for experiments on (double) quantum dots. Without knowing the lever arm, it is not possible to convert a measured gate voltage into an energy scale and thereby gain additional information about the system, e.g. about the level spacing. Since the electron temperature is not necessarily equal to the temperature of the refrigerator, knowing the actual electron temperature is important, because it is an experimental parameter which typically has considerable influence on the system. The third section of this appendix illustrates the

methods used for extracting lever arms and electron temperature.

Some of the experiments in this thesis required pulsing sequences on a millisecond time scale. The electronic components used here, are described in the fourth section. Here, it is of great importance how to add a fast voltage pulse to a fixed DC signal in order to generate voltage pulses of the required amplitude and pulse shape.

Finally, in the last section of this chapter, electrostatic simulations of different gate voltage configurations are discussed, which were performed in cooperation with Oliver Bärenbold and Dr. Michael Stopa. The simulation of the double dot configuration confirms the assumptions of a DQD system consisting of two very well separated dots with very small inter-dot tunneling. In Addition, both dots are also very well separated from the respective electron reservoir. Both, the small inter-dot tunneling and the weak coupling to source and drain were already deduced from experimental observations. The electrostatic simulations of the single dot configuration may help to obtain more information about the shape of the single quantum dot. Here, it turns out that in the original configuration of gate voltages the QD is asymmetric, which might be connected to the issue of spin-dependent tunneling, as it is discussed in chapter 4.

B.1. Background Subtraction

The software tool used to subtract a background from raw data, is a really simple but extraordinary effective program. In many cases subtracting a background simply means to subtract a line or a plane from one-dimensional or two-dimensional data. The subtracted function is usually either fitted to the data set, or corresponds to a background signal predicted from theory. In case of charge sensing measurements, the background signal is the average conductance at the operation point of the charge sensor. Due to the capacitive coupling between SQD and DQD, both systems interact with each other, which is the reason why charge sensing is possible in the first place. Additional features, like the feedback mechanism described in the following section of this appendix, further complicate the situation by performing operations on the charge sensor, aiming at stabilizing the SQD at a predefined operation point in order to maximize sensitivity. However, in many scans the operation point of the charge sensor is still not perfectly fixed. Instead, its conductance varies and shows e.g. a series of different Coulomb oscillations. The situations is even more difficult in cases where charge sensing sensitivity is not yet optimized and consequently the resulting measurement features are hard to distinguish from other effects and from the background signal. All these problems are more moderate when using the background subtraction tool described here.

In Figure B.1 (a) a set of raw data is depicted, which shows a section of the charge

stability diagram of a double quantum dot. During this scan the operation point of the sensor quantum dot is driven away from the original position on the flank of a Coulomb peak (blue region) into the minimum between two succeeding Coulomb peaks, where the slope is very small and hence the sensitivity is minimal (red region). In the region

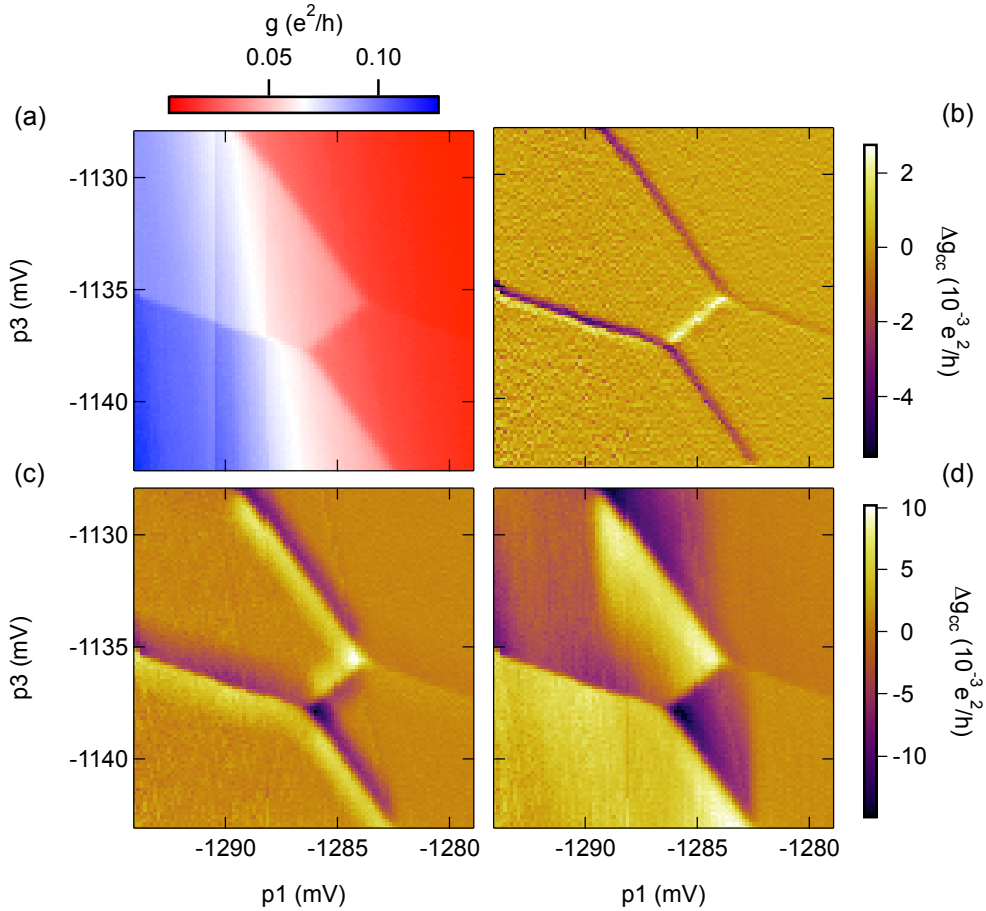

Figure B.1.: (a) Charge sensing measurement showing the (0,0) to (1,1) transition region of the CSD. By varying p1 and p3 the charge sensor is driven away from the original operation point, due to capacitive coupling. Because of the varying sensor sensitivity it is hard to distinguish all transition lines of the CSD. (b) - (d) Same data set as in (a) but after applying the background subtraction tool described in the main text. From (b) to (d), the interval length used for background subtraction increases successively from 5 over 20 to 100 points.

with very low sensitivity it is hard to distinguish electron transition, i.e. the lines in the CSD. The background subtraction tool requires the original data set and an interval length as input parameters. Each two-dimensional data set consists of a number of one-dimensional traces. The background subtraction tool takes each of these traces and for every point of the individual trace the average in a symmetric range around the respective point is calculated. The length of the range in which the average is calculated, is identical to the interval length required as input parameter. Thereby it is possible to influence the number of points which are used for calculating the average.

Finally, the average is subtracted from the respective point and data points edited in this way are stored in a new data set.

While raw data is presented in Figure B.1 (a), different results of this background subtraction procedure are shown in Figure B.1 (b)-(d), where different interval lengths have been chosen. Figure B.1 (b) corresponds to the shortest interval length (5 points). In this graph the effect of varying sensor conductance is completely absent and the electron transitions in this region of the CSD are the only distinct feature.

From Figure B.1 (c) to (d) the interval length is increased from 20 points to 100 points. In Figure B.1 (c) all lines in the CSD can still be distinguished, but those lines appear broader than in (b) and additional brighter and darker features emerge. For even higher interval length this process continues, and it becomes obvious that the processed data converges towards the original data set. In Figure B.1 (d) the features caused by a varying sensor operation point are clearly present again. However, even for this long interval length, the edited data still shows more details of the CSD than the raw data. Obviously, this procedure is quite similar to numerically differentiating the raw data. However, the background subtraction tool described here, has a certain advantage, that leads to a higher flexibility, compared to numerical differentiation. While for numerical differentiation only directly neighboring points are taken into account, the procedure described here, allows for choosing an interval within which all points are considered. This procedure proofs to be especially versatile in cases, where the slope corresponding to a detected tunneling event is rather low. In this cases, numerically differentiating the raw data may not bring any improvement at all. In contrast, by using the subtraction tool, one is still capable of improving the contrast in the data considerably, by choosing a longer evaluation interval.

B.2. Charge Sensor - Linear Feedback Mechanism

The capacitive coupling between charge sensor and (double) quantum dot is the reason why charge sensing is possible. One the other hand it is important to fix the SQD conductance at an operation point, where the sensitivity has a maximum. Performing scans at the (double) quantum dot system by varying gate voltages, drives the charge sensor away from the originally selected operation point and thereby the sensitivity changes. By implementing a feedback mechanism this influence is minimized, such that ideally the sensor conductance is fixed and only tunneling electrons in the (double) quantum dot system induce a change in the sensor signal. Hence, the sensor only reacts to events of interest, while other influences are reduced as far as possible. All experiments described in this thesis rely on a linear feedback mechanism, which regulates the sensor quantum dot according to changes in gate voltage of the investigated

(double) quantum dot system. The number of electrons in the QD/DQD is controlled via gates p1 and p3 (see Figure 2.2) and varying the voltages applied to those two gates influences the SQD in the way described above. The sensor feedback is realized by changing the voltage applied to the SQD plunger gate L2 and it is assumed, that the capacitive coupling between p1 and p3 on one side and L2 on the other side, is described by

$$\begin{aligned} \Delta V_{p1} &= \beta_1 \cdot \Delta V_{L2} \\ \Delta V_{p3} &= \beta_2 \cdot \Delta V_{L2} \ , \end{aligned} \tag{B.1}$$

where β_1 and β_2 are coupling constants, which have to be determined experimentally. In other words, one assumes the gate voltage changes ΔV_{p1}, ΔV_{p3} to act like a linear change in the voltage applied to the plunger gate L2, with β_1 and β_2 as constants of proportionality. Figure B.2 illustrates how those two constants can be determine experimentally. Here, two-dimensional scans are depicted, where the sensor conductance is measured either as a function of L2 and p1, or L2 and p3. In both measurements

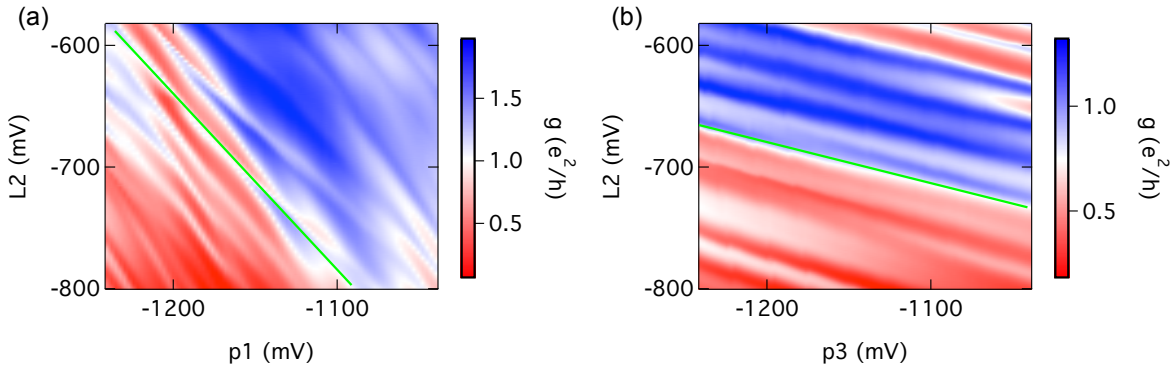

Figure B.2.: Experimental determination of β_1 and β_2: (a) Sensor conductance measured as function of SQD plunger gate L2 and *left hand gate* p1. (b) Same measurement as in (a) but as now as function of the *right hand gate* p3. In both data sets, a green line illustrates the effect of capacitive coupling. From the slopes of those lines, β_1 and β_2 are determined.

one can see a number of parallel lines, which correspond to Coulomb oscillations and occur as a function of L2 and p1, or p3 respectively. By determining the slope of these parallel lines (green lines in Figure B.2), β_1 and β_2 can be determined. After determining β_1 and β_2, the linear feedback mechanism can be activated. Now, for a gate voltage change (ΔV_{p1}, ΔV_{p3}) the necessary corrections for gate L2 are calculated according to Equation B.1.

Of course, Equation B.1 is only an approximation of the capacitive coupling between the respective gates. However, this simple method is very effective, as is demonstrated in Figure B.3. Here, the same measurement is depicted twice, once with sensor feed-

back activated and once without this additional mechanism. In the center of both

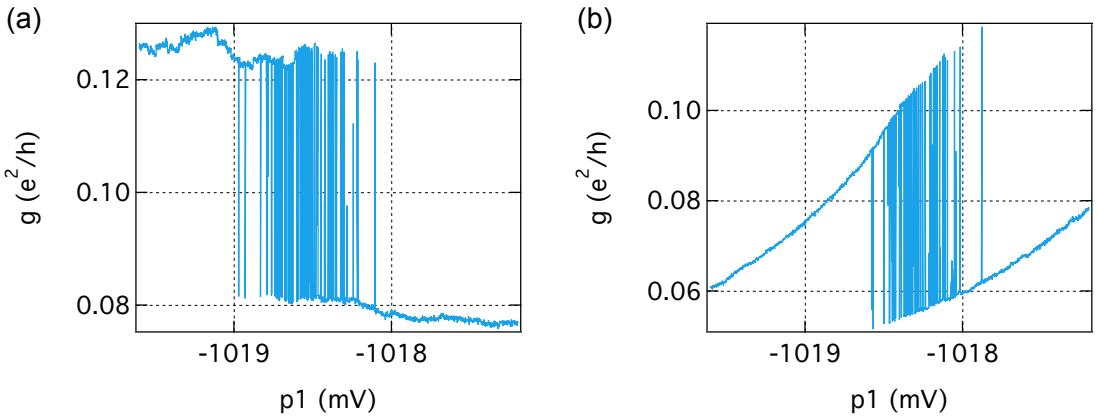

Figure B.3.: Illustration of the sensor feedback mechanism: (a) Sensor conductance measured as function of p1, where an electron transition is resolved in real-time. Here, the sensor conductance runs almost perfectly horizontally, due to the active compensation of the capcitive coupling between SQD and QD/DQD system. (b) Same measurement as in (a), but with deactivated sensor feed back. Now one clearly observes the effect of capcaitive coupling, which manifest as the strong gate voltage dependence observed on both sides of the electron transition.

graphs an electron transition is resolved in real-time. On both sides of the transition, the measured conductance shows a gate voltage dependence in case the sensor feedback is deactivated (Figure B.3) (b). This is not the case when the feedback mechanism is turned on, as depicted in Figure B.3 (a). Here, the sensor conductance runs almost perfectly horizontal, apart from some minor fluctuations.

As was pointed out in chapter 3, this linear feedback mechanism works very good on small scales, i.e. for small changes in gate voltage ΔV_{p1}, ΔV_{p3} of about 10-20 mV. On larger scales the effect of capacitive coupling is not completely compensated, hence changes in the sensor conductance/sensitivity are observed again. Since most experiments take place within a small range of gate voltages corresponding to a configuration of the DQD/QD system around a certain electron transition, e.g. T1-measurements or measurements of thermally activated tunneling, this simple feedback mechanism is sufficient. However, if a improved sensor stability is required, this can be obtained by adding higher terms to Equation B.1.

B.3. Lever Arm - and Temperature Determination

In chapter 2, transport measurements on quantum dots are described in detail. There it is also described how Coulomb diamonds obtained from such transport measurements can be used to determine lever arms, the conversion factors required to convert gate voltage to energy. In chapter 2 and chapter 3 it is pointed out, that transport measure-

ments are not practicable in the limit of very low coupling to the electron reservoirs. However, basically all experiments described in this thesis required low tunneling rates to source and drain and hence do not allow for transport measurements. Of course, one possible approach is to determine the required lever arms in the regime where transport measurements are possible and afterwards tune the system into the regime where the experiments can be performed. As was already pointed out in chapter 2, the lever arms might change for different gate voltage configurations of a device. Consequently, the lever arms determined by this approach can have a high uncertainty, which is transferred to all quantities calculated with this lever arm.

In this section of Appendix B, a different approach to determine lever arms is presented. The basic idea is to apply a DC bias across the quantum dot, just like in case of generic transport measurements. Instead of probing the transport through the QD, charge sensing is used to measure Coulomb diamonds. Of course, charge sensing is only sensitive to changes in the charge configuration of the quantum dot system. Hence, the measured Coulomb diamonds are expected to differ from conventional transport data. An example is depicted in Figure B.4, where the standard deviation[1] of the charge sensing signal is plotted as a function of the applied DC bias and either p1 or p3 (see Figure 2.2). In comparison to Coulomb diamonds obtained from direct transport measurements, where zero conductance is measured within the diamonds due to Coulomb blockade and a non-zero conductance outside, one can only identify the actual border of the diamonds (marked red in Figure B.4). In Addition, one observes excited states in both data sets shown (dashed red lines). The information included in this data sets is enough to determine the lever arm of gates p1 and p3, as described in Figure 2.7. Extracting both lever arms gives

$$\begin{aligned} \alpha_{p3} &= 61.9 \pm 1.5 \, \frac{\mu\text{eV}}{\text{mV}} \\ \alpha_{p1} &= 66.6 \pm 1.5 \, \frac{\mu\text{eV}}{\text{mV}}. \end{aligned} \tag{B.2}$$

Both values differ from the values extracted from direct transport measurements, determined for a gate voltage configuration, where the coupling to source and drain was higher. For α_{p1} the lever arm from Equation B.2 is 10% smaller, while α_{p3} is 12% smaller than the value obtained before.

The data shown in Figure B.4 demonstrates, that charge sensing can be used to measure Coulomb diamonds in the regime of very low tunneling rates to source and drain. Additionally, comparing the results of this method with previously obtained

[1]The method used to determine the standard deviation of the charge sensing signal is explained in chapter 3. Here, the standard deviation is depicted instead the average charge sensing signal, because the borders of the CB diamonds are more distinct.

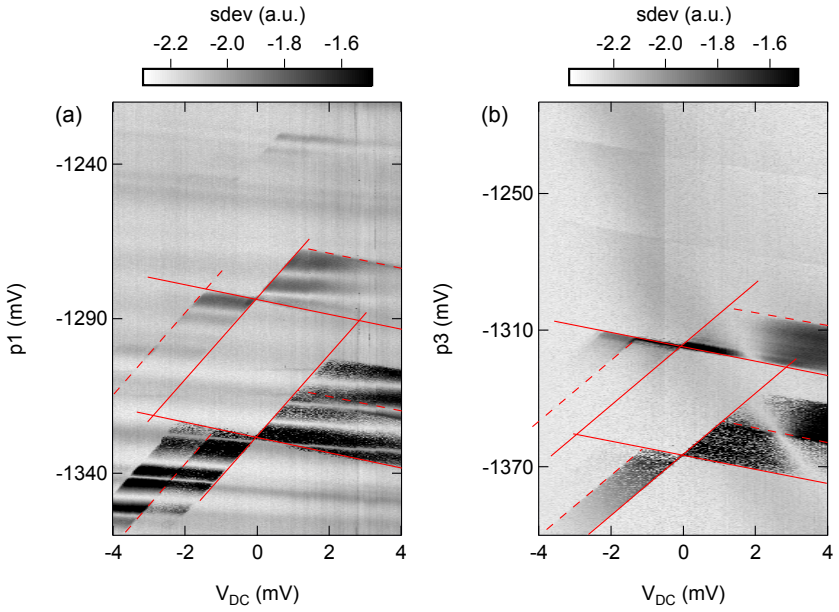

Figure B.4.: CB diamonds obtained from charge sensing measurements. A DC bias is applied across the QD, but since the direct transport signal is to small to be measured due to the very low source-drain coupling, charge sensing is applied. (a) and (b) depict the standard deviation of the signal as function of DC bias and either gate p1 or gate p3. A background is subtracted from both data sets and they are plotted on a logarithmic scale. Red lines are guidelines to the eye, dashed lines mark excited states.

values for α_{p1} and α_{p3}, clarifies the non negligible changes to the lever arms during the process of tuning a device.

Lever arms, like those from Equation B.2, are required to determine the electron temperature from the measured width of an electron transition, which corresponds to a Fermi function (see e.g. Figure 3.7 and Figure 4.2). All electron temperatures in this thesis were obtain by fitting Fermi functions to the respective data set and subsequent conversion of the width of the Fermi function to a temperature with the help of either α_{p1} or α_{p3}. Therefore, it is of great relevance to determine α_{p1} and α_{p3} as precisely as possible.

B.4. Pulsing setup

Some of the experiments described here, especially the T1-measurements, require gate pulsing techniques. They are necessary to load and unload electrons on a time scale of milliseconds or faster. This section illustrates the technical realization of gate pulsing on the experimental setup used for the experiments in this thesis. As was already pointed out in chapter 3, the DC voltages applied to the gate structures forming the quantum dot, is supplied by a LNHR DAC, while a NI USB-6366 DAQ is used as measuring

device. The NI device also provides two output channels capable of providing fast voltage pulses of ±10 V maximum amplitude and update rate of 3.33 Ms/s. The Ni USB DAQ additionally provides a trigger mechanism, where the measurement on the input channel is triggered on the voltage pulse from an output channel. Consequently, it is possible to start measurements almost simultaneously with a pulsing sequence[2], which simplifies data analysis considerably. The gate pulsing is realized in the experiments by adding the voltage pulse, provided by the Ni DAQ, to the DC signal from the LNHR DAC. Both devices have a different output impedance, which has to be considered in the design of the device that adds both signals. Figure B.5 depicts the schematics of the device used to add voltage pulses from the NI USB-DAQ output to the LNHR DC voltage source. In the following, this device is referred to as *pulse box*. Basically, the *pulse box* consists of two voltage dividers, one for the AC side, i.e. the output signal of the NI USB-DAQ, and another for the LNHR DAC output. As illustrated

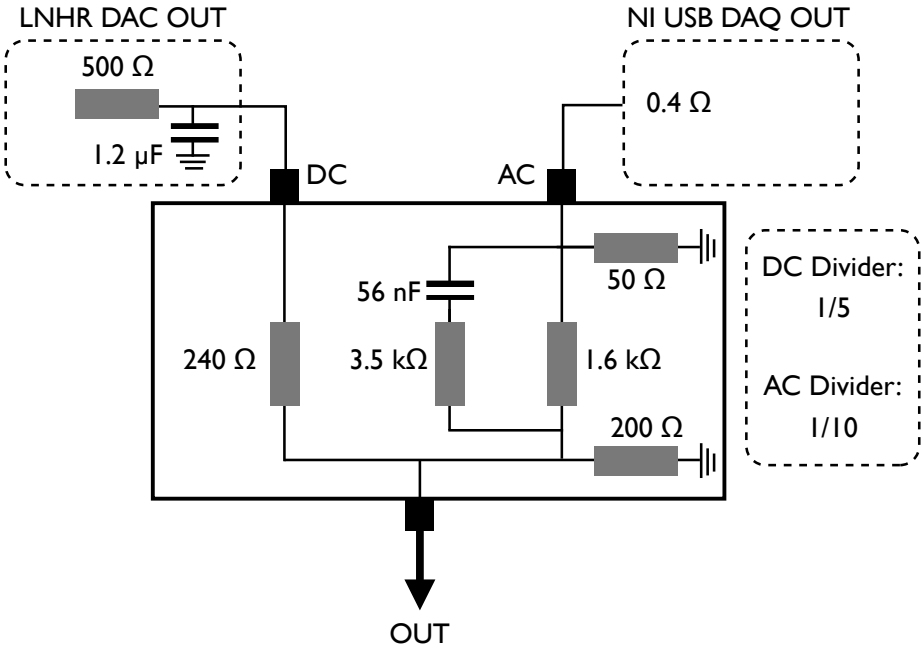

Figure B.5.: Schematic of the *pulse box* used to add an AC pulse sequence, generated by the NI USB-DAQ, to a DC voltage provided by the LNHR DAC. Every gate used for pulsing experiments is connected to the LNHR DAC and the NI USB-DAQ via such a *pulse box*. The design and mode of operation are discussed in detail in the main text.

in Figure B.5, the LNHR DAC has an output impedance of 500 Ω, while the output impedance of the NI USB-DAQ is 0.4 Ω. Hence, impedance matching via the *pulse box* is crucial to avoid reflections and other effects that disturb the pulsing sequence. The voltage dividers in the *pulse box* divide the DC signal by a factor of 5, and the

[2]In the experiments the delay between measurement an pulsing sequence was smaller than 0.5 ms, which in most measurements is less than the spacing between two points.

AC signal by a factor of 10. In addition, there is a RC-circuit integrated into the *pulse box*, which is required to compensate for the RC-circuit at the output channel of the LNHR DAC. The RC-circuit at the LNHR DAC output is given by the $1.2\,\mu$F capacitor to ground, in combination with the $500\,\Omega$ resistor. In order to increase the flexibility of the *pulse box* and to compensate for deviations from the specified values of the individual electric components, a variable resistor is used for the compensation element.

Prior to connecting a *pulse box* to a depletion gate of a sample, the exact division factors are determined, in order to calibrate the amplitude of the resulting signals. Furthermore, the variable resistor of the compensation element is adjusted such that a sequence of square pulses is transmitted with optimal rise time and pulse shape. Experimentally determined rise times for the *pulse box* are in the order of $30 - 60\,$ns, which is more than sufficient for experiments with a millisecond time resolution.

B.5. Device Simulations

Computer simulations can be a powerful tool to obtain more information about experimental results in comparison with theoretical predictions. For GaAs quantum dots, simulating the electrostatic configuration of a device for a certain set of gate voltages is of special interest. The resulting charge density of the system contains useful information about the shape of a QD/DQD, the coupling to electron reservoirs and in case of a DQD the inter-dot coupling. Besides the electrostatic configuration, calculating wave functions and energy spectra is of interest as well. Comparing experimental results of e.g. excited state spectroscopy with theoretical energy spectra from computer simulations can help to characterize the device and e.g. find gate voltage configurations, which lead to a more symmetric QDs. This approach was used by Amasha *et al.*[54], since according to their observations, the visibility of the Zeeman splitting (see chapter 4) is correlated to the QD symmetry [27].

Parallel to the experiments described here, computer simulations were used as additional tool. The SETE[3] code was written and provided by Dr. Michael Stopa[4] [141]. This program uses density functional theory to simulate quantum dots (and quantum wires) based on AlGaAs heterostructures. Two simulations are depicted in Figure B.6, one shows a double dot configuration and the other a single dot configuration. Both graphs are plotted in units of effective Bohr radii on the x- and y-axis, hence the electron density is given by one over effective Bohr radii squared. Figure B.6 (a) is based on the gate voltage configuration of the DQD, which was used throughout the

[3]Further information can be found under http://www.nnin.org/sete

[4]I gratefully would like to thank Dr. Stopa for his help.

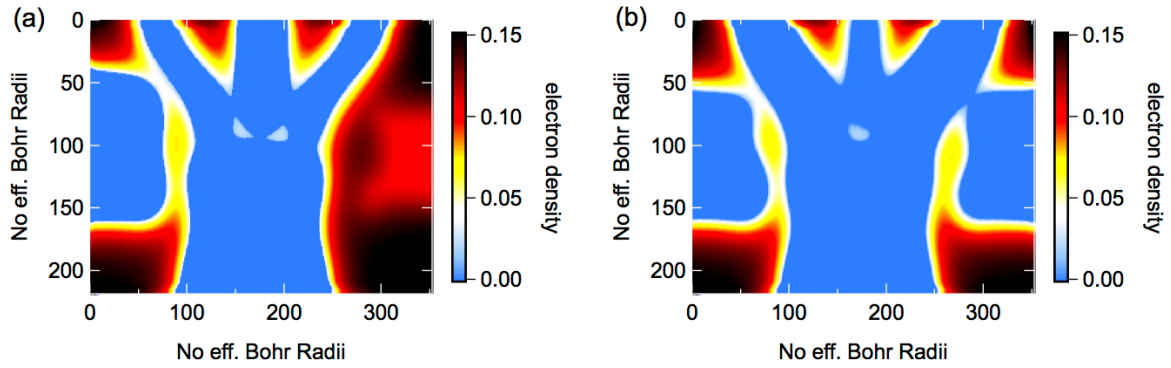

Figure B.6.: Electrostatic simulations of different gate voltage configurations used in the experiments. (a) In the double dot regime, the simulation predicts a system of well separated quantum dots, both with weakly coupled to their respective lead. Hence, the results of this simulation supports the experimental observation described in chapter 5. (b) Simulation of the same device, but now tuned to the single dot regime. Here, the simulation estimates an electron density which corresponds to an elliptic quantum dot, which is rotated with respect to the symmetry axis of the gate layout. This simulation can be used as starting point to find gate voltage configurations leading to a more symmetric QD, which is relevant for the effect of spin-dependent tunneling into the QD.

experiments on thermally activated charge state switching. There, experimental observations implied a very weak inter-dot coupling as well as weak coupling to source an drain. The simulation depicted in Figure B.6 (a) agrees with these experimental observations. Based on the sheet electron density, the wafer profile and the gate layout and voltages as input parameters, the simulation predicts an electrostatic configuration where two very well separated quantum dots are present in the system. Both dots are only very weakly coupled to one electron reservoir. Additionally, the simulation includes a sensor quantum dot (see left SQD in Figure B.6 (a)) which is quite close to the double dot system and which is coupled rather strong to source and drain. Since in the experiment the sensor QD was in the tunnel broadened regime, the simulation confirms these experimental result as well, and thereby underlines the good agreement between simulation and experiment.

Figure B.6 (b) depicts a simulation of the same device as in (a), but now tuned to the single dot regime. Again, wafer profile, electron density, gate layout and gate voltages were used as input parameters for the simulation. The gate voltage configuration used here, i.e. the single dot configuration, is used throughout the spin-relaxation time measurements and related experiments. Here, the symmetry of the QD is of special interest, because of the connection to the Zeeman visibility (see chapter 4 and [54],[27]). The resulting QD shows an elliptic shape and is rotated with respect to the symmetry axis of the nanostructure. With the help of additional simulations it is possible to determine gate voltage configurations, which lead to a symmetric dot that is not

rotated with respect to the device symmetry axis (not shown). Whether or not this the gate voltage configuration has influence on the visibility of the Zeeman splitting is the subject of ongoing experiments.

Bibliography

[1] N. W. Ashcroft and N. D. Mermin. *Solid State Physics* (Thomson Learning, 1976).

[2] R. Gross and N. A. Marx. *Festkörperphysik* (Oldenbourg Verlag, 2012).

[3] J. H. Davis. *The Physics of Low-Dimensional Semiconductors* (Cambridge University Press, 1998).

[4] T. Ihn. *Semiconductor Nanostructures* (Oxford University Press, 2010).

[5] M. A. Reed, J. N. Randall, R. J. Aggarwal, R. J. Matyi, T. M. Moore, and A. E. Wetsel. *Observation of discrete electronic states in a zero-dimensional semiconductor nanostructure.* Phys. Rev. Lett. **60**, 535 (1988).

[6] M. A. Kastner. *The single-electron transistor.* Rev. Mod. Phys. **64**, 849 (1992).

[7] R. C. Ashoori. *Electrons in Artificial Atoms.* Nature **379**, 413 (1996).

[8] L. P. Kouwenhoven, D. G. Austing, and S. Tarucha. *Few-Electron Quantum Dots.* Rep. Prog. Phys. **64**, 701 (2001).

[9] G. W. Bryant. *Resonant tunneling in zero-dimensional nanostructures.* Phys. Rev. B **39**, 3145 (1989).

[10] L. P. Kouwenhoven, C. M. Marcus, P. L. McEuen, S. Tarucha, R. Westervelt, and N. Wingreen. *Mesoscopic Electron Transport.* NATO ASI Series E **345**, 105 (1997).

[11] C. B. Murray, D. J. Norris, and M. G. Bawendi. Journal of the American Chemical Society **115**, 8706 (1993).

[12] M. J. Biercuk, S. Garaj, N. Mason, J. M. Chow, and C. M. Marcus. *Gate-Defined Quantum Dots on Carbon Nanotubes.* Nano Letters **5**, 1267 (2005).

[13] C. Fasth, A. Fuhrer, M. T. Björk, and L. Samuelson. *Tunable Double Quantum Dots in InAs Nanowires Defined by Local Gate Electrodes.* Nano Letters **5**, 1487 (2005).

[14] F. A. Zwanenburg, A. S. Dzurak, A. Morello, M. Y. Simmons, L. C. L. Hollenberg, G. Klimeck, S. Rogge, S. N. Coppersmith, and M. A. Eriksson. *Silicon quantum electronics.* Rev. Mod. Phys. **85**, 961 (2013).

[15] S. Das Sarma, S. Adam, E. H. Hwang, and E. Rossi. *Electronic transport in two-dimensional graphene.* Rev. Mod. Phys. **83**, 407 (2011).

[16] D. Loss and D. P. DiVincenzo. *Quantum Computation with Quantum Dots.* Phys. Rev. A **57**, 120 (1998).

[17] Y. Makhlin, G. Schön, and A. Shnirman. *Quantum-state engineering with Josephson-junction devices.* Rev. Mod. Phys. **73**, 357 (2001).

[18] F. Jelezko, T. Gaebel, I. Popa, M. Domhan, A. Gruber, and J. Wrachtrup. *Observation of Coherent Oscillation of a Single Nuclear Spin and Realization of a Two-Qubit Conditional Quantum Gate.* Phys. Rev. Lett. **93**, 130501 (2004).

[19] P. Kok, W. J. Munro, K. Nemoto, T. C. Ralph, J. P. Dowling, and G. J. Milburn. *Linear optical quantum computing with photonic qubits.* Rev. Mod. Phys. **79**, 135 (2007).

[20] R. Hanson, L. P. Kouwenhoven, J. R. Petta, S. Tarucha, and L. M. K. Vandersypen. *Spins in Few-Electron Quantum Dots.* Rev. Mod. Phys. **792**, 1217 (2007).

[21] V. Cerletti, W. A. Coish, O. Gywat, and D. Loss. *Recipes for spin-based quantum computing.* Nanotechnology **16**, R27 (2005).

[22] J. Levy. *Universal Quantum Computation with Spin-1/2 Pairs and Heisenberg Exchange.* Phys. Rev. Lett. **89**, 147902 (2002).

[23] J. Petta, A. Johnson, J. Taylor, E. Laird, A. Yacoby, M. D. Lukin, C. M. Marcus, M. P. Hanson, and A. Gossard. *Coherent manipulation of coupled electron spins in semiconductor quantum dots.* Science **309**, 2180 (2005).

[24] J. M. Elzerman, R. Hanson, L. H. W. van Beveren, B. Witkamp, L. M. K. Vandersypen, and L. P. Kouwenhov. *Single-shot read-out of an individual electron spin in a quantum dot.* Nature **430**, 431 (2004).

[25] H.-A. Engel, V. N. Golovach, D. Loss, L. M. K. Vandersypen, J. M. Elzerman, R. Hanson, and L. P. Kouwenhoven. *Measurement Efficiency and n-Shot Readout of Spin Qubits.* Phys. Rev. Lett. **93**, 106804 (2004).

[26] R. Hanson, L. H. W. van Beveren, I. T. Vink, J. M. Elzerman, W. J. M. Naber, F. H. L. Koppens, L. P. Kouwenhoven, and L. M. K. Vandersypen. *Single-Shot Readout of Electron Spin States in a Quantum Dot Using Spin-Dependent Tunnel Rates.* Phys. Rev. Lett. **94**, 196802 (2005).

[27] S. Amasha, K. MacLean, I. Radu, D. M. Zumbuhl, M. P. Kastner, M. A.and Hanson, and A. C. Gossard. *Measurements of the spin relaxation rate at low magnetic fields in a quantum dot.* arXiv:cond-mat/0607110 (2006).

[28] S. Amasha, K. MacLean, I. P. Radu, D. M. Zumbühl, M. A. Kastner, M. P. Hanson, and A. C. Gossard. *Electrical Control of Spin Relaxation in a Quantum Dot.* Phys. Rev. Lett. **100**, 046803 (2008).

[29] R. Hanson, B. Witkamp, L. M. K. Vandersypen, L. H. W. van Beveren, J. M. Elzerman, and L. P. Kouwenhoven. *Zeeman Energy and Spin Relaxation in a One-Electron Quantum Dot.* Phys. Rev. Lett. **91**, 196802 (2003).

[30] T. Meunier, I. T. Vink, L. H. W. van Beveren, K.-J. Tielrooij, R. Hanson, F. H. L. Koppens, H. P. Tranitz, W. Wegscheider, L. P. Kouwenhoven, and L. M. K. Vandersypen. *Experimental Signature of Phonon-Mediated Spin Relaxation in a Two-Electron Quantum Dot.* Phys. Rev. Lett. **98**, 126601 (2007).

[31] S. Sasaki, T. Fujisawa, T. Hayashi, and Y. Hirayama. *Electrical Pump-and-Probe Study of Spin Singlet-Triplet Relaxation in a Quantum Dot.* Phys. Rev. Lett. **95**, 056803 (2005).

[32] V. N. Golovach, A. Khaetskii, and D. Loss. *Phonon-Induced Decay of the Electron Spin in Quantum Dots.* Phys. Rev. Lett. **93**, 016601 (2004).

[33] A. C. J. Johnson, J. R. Petta, J. M. Taylor, A. Yacoby, M. D. Lukin, C. M. Marcus, M. P. Hanson, and A. C. Gossard. *Triplet–singlet spin relaxation via nuclei in a double quantum dot.* Nature **435**, 925 (2005).

[34] J. R. Petta, A. C. Johnson, A. Yacoby, C. M. Marcus, M. P. Hanson, and A. C. Gossard. *Pulsed-gate measurements of the singlet-triplet relaxation time in a two-electron double quantum dot.* Phys. Rev. B **72**, 161301 (2005).

[35] K. Ono and S. Tarucha. *Nuclear-Spin-Induced Oscillatory Current in Spin-Blockaded Quantum Dots.* Phys. Rev. Lett. **92**, 256803 (2004).

[36] F. H. L. Koppens, J. A. Folk, J. M. Elzerman, R. Hanson, L. H. Willems van Beveren, I. T. Vink, H. P. Tranitz, W. Wegscheider, L. P. Kouwenhoven, and V. L. M. K. *Control and Detection of Singlet-Triplet Mixing in a Random Nuclear Field.* Science **309**, 1346 (2005).

[37] S. Foletti, H. Bluhm, D. Mahalu, V. Umansky, and A. Yacoby. *Universal quantum control of two-electron spin quantum bits using dynamic nuclear polarization.* Nat. Phys. **5**, 903 (2009).

[38] F. H. L. Koppens, K. C. Nowack, and L. M. K. Vandersypen. *Spin Echo of a Single Electron Spin in a Quantum Dot.* Phys. Rev. Lett. **100**, 236802 (2008).

[39] H. Bluhm, S. Foletti, I. Neder, M. Rudner, D. Mahalu, V. Umansky, and A. Yacoby. *Dephasing time of GaAs electron-spin qubits coupled to a nuclear bath exceeding 200 μs.* Nat. Phys. **7**, 109 (2010).

[40] O. E. Dial, M. D. Shulman, S. P. Harvey, H. Bluhm, V. Umansky, and A. Yacoby. *Charge Noise Spectroscopy Using Coherent Exchange Oscillations in a Singlet-Triplet Qubit.* Phys. Rev. Lett. **110**, 146804 (2013).

[41] V. Kornich, C. Kloeffel, and D. Loss. *Phonon-Mediated Decay of Singlet-Triplet Qubits in Double Quantum Dots.* arxiv:1311.2197 (2013).

[42] A. V. Kuhlmann, J. Houel, A. Ludwig, L. Greuter, D. Reuter, A. D. Wieck, M. Poggio, and R. J. Warburton. *Charge noise and spin noise in a semiconductor quantum device.* Nature Physics **9**, 570 (2013).

[43] M. Field, C. G. Smith, M. Pepper, D. A. Ritchie, J. E. F. Frost, G. A. C. Jones, and D. G. Hasko. *Measurements of Coulomb blockade with a noninvasive voltage probe.* Phys. Rev. Lett. **70**, 1311 (1993).

[44] R. C. Ashoori, H. L. Stormer, J. S. Weiner, L. N. Pfeiffer, S. J. Pearton, K. W. Baldwin, and K. W. West. *Single-electron capacitance spectroscopy of discrete quantum levels.* Phys. Rev. Lett. **68**, 3088 (1992).

[45] B. J. van Wees, H. van Houten, C. W. J. Beenakker, J. G. Williamson, L. P. Kouwenhoven, D. van der Marel, and C. T. Foxon. *Quantized conductance of point contacts in a two-dimensional electron gas.* Phys. Rev. Lett. **60**, 848 (1988).

[46] D. A. Wharam, T. J. Thornton, R. Newbury, M. Pepper, H. Ahmed, J. E. F. Frost, D. G. Hasko, D. C. Peacock, D. A. Ritchie, and G. A. C. Jones. *One-dimensional transport and the quantisation of the ballistic resistance.* Journal of Physics C: Solid State Physics **21**, L209 (1988).

[47] C. Barthel, D. J. Reilly, C. M. Marcus, M. P. Hanson, and A. C. Gossard. *Rapid Single-Shot Measurement of a Singlet-Triplet Qubit.* Phys. Rev. Lett. **103**, 160503 (2009).

[48] W. G. van der Wiel, S. D. Franceschi, J. M. Elzerman, T. Fujisawa, S. Tarucha, and L. P. Kouwenhoven. *Electron transport through double quantum dots.* Rev. Mod. Phys. **75**, 1 (2003).

[49] I. Vurgaftman, J. R. Meyer, and L. R. Ram-Mohan. *Band parameters for III–V compound semiconductors and their alloys.* Journal of Applied Physics **89**, 5815 (2001).

[50] J. D. Jackson. *Classical Electrodynamics* (John Wiley ans Sons, 1998).

[51] T. Brandes, W. Häusler, K. Jauregui, B. Kramer, and D. Weinmann. *Coulomb Interaction and Transport in Tunnel Junctions and Quantum Dots.* Physica B **189**, 16 (1993).

[52] C. W. J. Beenakker. *Theory of Coulomb-blockade oscillations in the conductance of a quantum dot.* Phys. Rev. B **44**, 1646 (1990).

[53] E. B. Foxman, P. L. McEuen, U. Meirav, N. S. Wingreen, Y. Meir, P. A. Belk, N. R. Belk, M. A. Kastner, and S. J. Wind. *Effects of quantum levels on transport through a Coulomb island.* Phys. Rev. B **47**, 10020 (1993).

[54] S. Amasha. *Electron Tunneling and Spin Relaxation in a Lateral Quantum Dot.* Ph.D. thesis, Massachusetts Institute of Technology (2008).

[55] O. Klein, C. de C. Chamon, D. Tang, D. M. Abusch-Magder, U. Meirav, X. G. Wen, M. A. Kastner, and S. J. Wind. *Exchange Effects in an Artificial Atom at High Magnetic Fields.* Phys. Rev. Lett. **74**, 785 (1995).

[56] P. L. McEuen, E. B. Foxman, U. Meirav, M. A. Kastner, Y. Meir, N. S. Wingreen, and S. J. Wind. *Transport spectroscopy of a Coulomb island in the quantum Hall regime.* Phys. Rev. Lett. **66**, 1926 (1991).

[57] R. C. Ashoori, H. L. Stormer, J. S. Weiner, L. N. Pfeiffer, K. W. Baldwin, and K. W. West. *N-electron ground state energies of a quantum dot in magnetic field.* Phys. Rev. Lett. **71**, 613 (1993).

[58] P. L. McEuen, E. B. Foxman, J. Kinaret, U. Meirav, M. A. Kastner, N. S. Wingreen, and S. J. Wind. *Self-consistent addition spectrum of a Coulomb island in the quantum Hall regime.* Phys. Rev. B **45**, 11419 (1992).

[59] M. Ciorga, A. S. Sachrajda, P. Hawrylak, C. Gould, P. Zawadzki, S. Jullian, Y. Feng, and Z. Wasilewski. *Addition spectrum of a lateral dot from Coulomb and spin-blockade spectroscopy.* Phys. Rev. B **61**, R16315 (2000).

[60] C. Weisbuch and C. Hermann. *Optical detection of conduction-electron spin resonance in GaAs.* Phys. Rev. B **15**, 816 (1977).

[61] C. Hermann and C. Weisbuch. *kp perturbation theory in III-V compounds and alloys: a reexamination.* Phys. Rev. B **15**, 823 (1977).

[62] H. Haken and H. C. Wolf. *Atom- und Quantenphysik* (Springer Verlag, 2004).

[63] M. Pioro-Ladriere, J. H. Davies, A. R. Long, A. S. Sachrajda, L. Gaudreau, P. Zawadzki, J. Lapointe, J. Gupta, Z. Wasilewski, and S. Studenikin. *Origin of switching noise in GaAs/AlGaAs lateral gated devices.* Phys. Rev. B **72**, 115331 (2005).

[64] A. Kogan, S. Amasha, D. Goldhaber-Gordon, G. Granger, M. A. Kastner, and H. Shtrikman. *Measurements of Kondo and Spin Splitting in Single-Electron Transistors.* Phys. Rev. Lett. **93**, 166602 (2004).

[65] D. V. Averin and Y. V. Nazarov. *Virtual electron diffusion during quantum tunneling of the electric charge.* Phys. Rev. Lett. **65**, 2446 (1990).

[66] S. De Franceschi, S. Sasaki, J. M. Elzerman, W. G. van der Wiel, S. Tarucha, and L. P. Kouwenhoven. *Electron Cotunneling in a Semiconductor Quantum Dot.* Phys. Rev. Lett. **86**, 878 (2001).

[67] I. M. Ruzin, V. Chandrasekhar, E. I. Levin, and L. I. Glazman. *Stochastic Coulomb blockade in a double-dot system.* Phys. Rev. B **45**, 13469 (1992).

[68] C. Cohen-Tannoudji, B. Diu, and F. Laloe. *Quantum Mechanics* (John Wiley and Sons, 1977).

[69] K. Ono, D. G. Austing, Y. Tokura, and S. Tarucha. *Current Rectification by Pauli Exclusion in a Weakly Coupled Double Quantum Dot System.* Science **297**, 1313 (2002).

[70] A. C. Johnson, J. R. Petta, C. M. Marcus, M. P. Hanson, and A. C. Gossard. *Singlet-triplet spin blockade and charge sensing in a few-electron double quantum dot.* Phys. Rev. B **72**, 165308 (2005).

[71] R. J. Schoelkopf, P. Wahlgren, A. A. Kozhevnikov, P. Delsing, and D. E. Prober. *The Radio-Frequency Single-Electron Transistor (RF-SET): A Fast and Ultrasensitive Electrometer.* Science **280**, 1238 (1998).

[72] W. Lu, Z. Ji, L. Pfeiffer, K. W. West, and A. J. Rimberg. *Real-time detection of electron tunnelling in a quantum dot.* Nature **423**, 422 (2003).

[73] R. Schleser, T. Ihn, E. Ruh, K. Ensslin, M. Tews, D. Pfannkuche, D. C. Driscoll, and A. C. Gossard. *Cotunneling-Mediated Transport through Excited States in the Coulomb-Blockade Regime.* Phys. Rev. Lett. **94**, 206805 (2005).

[74] K. MacLean, S. Amasha, I. P. Radu, D. M. Zumbuhl, M. A. Kastner, M. P. Hanson, and A. C. Gossard. *Energy-Dependent Tunneling in a Quantum Dot.* Phys. Rev. Lett. **98**, 036802 (2007).

[75] T. Ihn, S. Gustavsson, U. Gasser, B. Küng, T. Müller, R. Schleser, M. Sigrist, I. Shorubalko, R. Leturcq, and K. Ensslin. *Quantum dots investigated with charge detection techniques.* Solid State Communications **149**, 1419 (2009).

[76] D. Sprinzak, Y. Ji, M. Heiblum, D. Mahalu, and H. Shtrikman. *Charge Distribution in a Kondo-Correlated Quantum Dot.* Phys. Rev. Lett. **88**, 176805 (2002).

[77] E. Buks, R. Schuster, M. Heiblum, D. Mahalu, and V. Umansky. *Dephasing in electron interference by a which-path detector.* Nature **391**, 871 (1998).

[78] C. Smith, S. Gardelis, J. Cooper, D. Ritchie, E. Linfield, Y. Jin, and H. Launois. *Detection of electron scattering in an isolated double quantum dot system.* Physica E: Low-dimensional Systems and Nanostructures **12**, 830 (2002).

[79] J. M. Elzerman, R. Hanson, J. S. Greidanus, L. H. Willems van Beveren, S. De Franceschi, L. M. K. Vandersypen, S. Tarucha, and L. P. Kouwenhoven. *Few-electron quantum dot circuit with integrated charge read out.* Phys. Rev. B **67**, 161308 (2003).

[80] J. R. Petta, A. C. Johnson, C. M. Marcus, M. P. Hanson, and A. C. Gossard. *Manipulation of a Single Charge in a Double Quantum Dot.* Phys. Rev. Lett. **93**, 186802 (2004).

[81] S. A. Gurvitz. *Measurements with a noninvasive detector and dephasing mechanism.* Phys. Rev. B **56**, 15215 (1997).

[82] M. Büttiker and A. M. Martin. *Charge relaxation and dephasing in Coulomb-coupled conductors.* Phys. Rev. B **61**, 2737 (2000).

[83] A. Silva and S. Levit. *Effects of entanglement in controlled dephasing.* Phys. Rev. B **63**, 201309 (2001).

[84] A. N. Korotkov. *Selective quantum evolution of a qubit state due to continuous measurement.* Phys. Rev. B **63**, 115403 (2001).

[85] H.-S. Goan and G. J. Milburn. *Dynamics of a mesoscopic charge quantum bit under continuous quantum measurement.* Phys. Rev. B **64**, 235307 (2001).

[86] A. A. Clerk, S. M. Girvin, and A. D. Stone. *Quantum-limited measurement and information in mesoscopic detectors.* Phys. Rev. B **67**, 165324 (2003).

[87] D. S. Duncan, C. Livermore, R. M. Westervelt, K. D. Maranowski, and A. C. Gossard. *Direct measurement of the destruction of charge quantization in a single-electron box.* Applied Physics Letters **74**, 1045 (1999).

[88] C. Barthel, M. Kjaergaard, J. Medford, M. Stopa, C. M. Marcus, M. P. Hanson, and A. C. Gossard. *Fast sensing of double-dot charge arrangement and spin state with a radio-frequency sensor quantum dot.* Phys. Rev. B **81**, 161308 (2010).

[89] L. M. K. Vandersypen, J. M. Elzerman, R. N. Schouten, L. H. Willems van Beveren, R. Hanson, and L. P. Kouwenhoven. *Real-time detection of single-electron tunneling using a quantum point contact.* Applied Physics Letters **85**, 4394 (2004).

[90] I. T. Vink, T. Nooitgedagt, R. N. Schouten, L. M. K. Vandersypen, and W. Wegscheider. *Cryogenic amplifier for fast real-time detection of single-electron tunneling.* Applied Physics Letters **91** (2007).

[91] D. J. Reilly, C. M. Marcus, M. P. Hanson, and A. C. Gossard. *Fast single-charge sensing with a rf quantum point contact.* Applied Physics Letters **91** (2007).

[92] C. P. Scheller, S. Heizmann, K. Bedner, D. Giss, M. Meschke, J. Pekola, and D. M. Zumbuhl. *Miniature Microwave Filters for Thermalization below 10 mK.* In preparation.

[93] J. B. Johnson. *Thermal Agitation of Electricity in Conductors.* Phys. Rev. **32**, 97 (1928).

[94] H. Nyquist. *Thermal Agitation of Electric Charge in Conductors.* Phys. Rev. **32**, 110 (1928).

[95] P. Horowitz and W. Hill. *The Art of Electronics* (Cambridge University Press, 1989).

[96] Y. Meir and A. Golub. *Shot Noise through a Quantum Dot in the Kondo Regime.* Phys. Rev. Lett. **88**, 116802 (2002).

[97] M. Buttiker. *Scattering theory of thermal and excess noise in open conductors.* Phys. Rev. Lett. **65**, 2901 (1990).

[98] S. M. Cronenwett, T. H. Oosterkamp, and L. P. Kouwenhoven. *A Tunable Kondo Effect in Quantum Dots.* Sience **281**, 540 (1998).

[99] L. Kouwenhoven and L. Glazman. *Revival of the Kondo effect.* arXiv:cond-mat/0104100 (2001).

[100] D. Goldhaber-Gordon, H. Shtrikman, D. Mahalu, D. Abusch-Magder, U. Meirav, and M. A. Kastner. *Kondo effect in a single-electron transistor.* Nature **391**, 156 (1998).

[101] A. V. Khaetskii, D. Loss, and L. Glazman. *Electron Spin Decoherence in Quantum Dots due to Interaction with Nuclei.* Phys. Rev. Lett. **88**, 186802 (2002).

[102] I. A. Merkulov, A. L. Efros, and M. Rosen. *Electron spin relaxation by nuclei in semiconductor quantum dots.* Phys. Rev. B **65**, 205309 (2002).

[103] W. Nolting. *Grundkurs theoretische Physik. Bd.6 : Statistische Physik* (Springer Verlag, 2004).

[104] K. Hitachi, M. Yamamoto, and S. Tarucha. *Spin selective spectroscopy of a quantum dot using tunnel-coupled quantum wires as spin filters.* Phys. Rev. B **74**, 161301 (2006).

[105] D. Rohrlich, O. Zarchin, M. Heiblum, D. Mahalu, and V. Umansky. *Controlled Dephasing of a Quantum Dot: From Coherent to Sequential Tunneling.* Phys. Rev. Lett. **98**, 096803 (2007).

[106] I. Hapke-Wurst, U. Zeitler, H. Frahm, A. G. M. Jansen, R. J. Haug, and K. Pierz. *Magnetic-field-induced singularities in spin-dependent tunneling through InAs quantum dots.* Phys. Rev. B **62**, 12621 (2000).

[107] E. E. Vdovin, Y. N. Khanin, O. Makarovsky, Y. V. Dubrovskii, A. Patanè, L. Eaves, M. Henini, C. J. Mellor, K. A. Benedict, and R. Airey. *Magnetoanisotropy of electron-correlation-enhanced tunneling through a quantum dot.* Phys. Rev. B **75**, 115315 (2007).

[108] S. Amasha, K. MacLean, I. P. Radu, D. M. Zumbühl, M. A. Kastner, M. P. Hanson, and A. C. Gossard. *Spin-dependent tunneling of single electrons into an empty quantum dot.* Phys. Rev. B **78**, 041306 (2008).

[109] P. Stano and P. Jacquod. *Spin-dependent tunneling into an empty lateral quantum dot.* Phys. Rev. B **82**, 125309 (2010).

[110] K. C. Nowack, F. H. L. Koppens, Y. V. Nazarov, and L. M. K. Vandersypen. *Coherent Control of a Single Electron Spin with Electric Fields.* Science **318**, 1430 (2007).

[111] C. Barthel, M. Kjærgaard, J. Medford, M. Stopa, C. M. Marcus, M. P. Hanson, and A. C. Gossard. *Fast sensing of double-dot charge arrangement and spin state with a radio-frequency sensor quantum dot.* Phys. Rev. B **81**, 161308 (2010).

[112] T. Fujisawa, T. H. Oosterkamp, W. G. van der Wiel, B. W. Broer, R. Aguado, S. Tarucha, and L. P. Kouwenhoven. *Spontaneous Emission Spectrum in Double Quantum Dot Devices.* Science **282**, 932 (1998).

[113] D. Harbusch, D. Taubert, H. P. Tranitz, W. Wegscheider, and S. Ludwig. *Phonon-Mediated versus Coulombic Backaction in Quantum Dot Circuits.* Phys. Rev. Lett. **104**, 196801 (2010).

[114] D. Taubert, M. Pioro-Ladrière, D. Schröer, D. Harbusch, A. Sachrajda, and S. Ludwig. *Telegraph Noise in Coupled Quantum Dot Circuits Induced by a Quantum Point Contact.* Phys. Rev. Lett. **100**, 176805 (2008).

[115] P. Roulleau, S. Baer, T. Choi, F. Molitor, J. Güttinger, T. Müller, S. Dröscher, K. Ensslin, and T. Ihn. *Coherent electron–phonon coupling in tailored quantum systems.* Nat. Comm. **2**, 1241 (2010).

[116] M. D. Shulman, O. E. Dial, S. P. Harvey, H. Bluhm, V. Umansky, and A. Yacoby. *Demonstration of Entanglement of Electrostatically Coupled Singlet-Triplet Qubits.* Science **336**, 202 (2012).

[117] M. Schlosshauer. *Decoherence and The Quantum-To-Classical Transition* (Springer, 2007).

[118] S. A. Wolf, D. D. Awschalom, R. A. Buhrman, J. M. Daughton, S. von Molnár, M. L. Roukes, A. Y. Chtchelkanova, and D. M. Treger. *Spintronics: A Spin-Based Electronics Vision for the Future.* Science **294**, 1488 (2001).

[119] I. Zutic, J. Fabian, and S. Das Sarma. *Spintronics: Fundamentals and applications.* Rev. Mod. Phys. **76**, 323 (2004).

[120] F. H. L. Koppens, C. Buizert, K. J. Tielrooij, I. T. Vink, K. C. Nowack, T. Meunier, L. P. Kouwenhoven, and L. M. K. Vandersypen. *Driven coherent oscillations of a single electron spin in a quantum dot.* Nature **442**, 766 (2006).

[121] L. M. K. Vandersypen and I. L. Chuang. *NMR techniques for quantum control and computation.* Rev. Mod. Phys. **76**, 1037 (2005).

[122] D. J. Reilly, J. M. Taylor, E. A. Laird, J. R. Petta, C. M. Marcus, M. P. Hanson, and A. C. Gossard. *Measurement of Temporal Correlations of the Overhauser Field in a Double Quantum Dot.* Phys. Rev. Lett. **101**, 236803 (2008).

[123] J. Medford, L. Cywiński, C. Barthel, C. M. Marcus, M. P. Hanson, and A. C. Gossard. *Scaling of Dynamical Decoupling for Spin Qubits.* Phys. Rev. Lett. **108**, 086802 (2012).

[124] A. V. Khaetskii and Y. V. Nazarov. *Spin-flip transitions between Zeeman sublevels in semiconductor quantum dots.* Phys. Rev. B **64**, 125316 (2001).

[125] F. Marquardt and V. A. Abalmassov. *Spin relaxation in a quantum dot due to Nyquist noise.* Phys. Rev. B **71**, 165325 (2005).

[126] P. San-Jose, G. Zarand, A. Shnirman, and G. Schön. *Geometrical Spin Dephasing in Quantum Dots.* Phys. Rev. Lett. **97**, 076803 (2006).

[127] V. I. Fal'ko, B. L. Altshuler, and O. Tsyplyatyev. *Anisotropy of Spin Splitting and Spin Relaxation in Lateral Quantum Dots.* Phys. Rev. Lett. **95**, 076603 (2005).

[128] P. Stano and J. Fabian. *Orbital and spin relaxation in single and coupled quantum dots.* Phys. Rev. B **74**, 045320 (2006).

[129] M. Borhani, V. N. Golovach, and D. Loss. *Spin decay in a quantum dot coupled to a quantum point contact.* Phys. Rev. B **73**, 155311 (2006).

[130] S. I. Erlingsson and Y. V. Nazarov. *Hyperfine-mediated transitions between a Zeeman split doublet in GaAs quantum dots: The role of the internal field.* Phys. Rev. B **66**, 155327 (2002).

[131] C. Calero, E. M. Chudnovsky, and D. A. Garanin. *Field Dependence of the Electron Spin Relaxation in Quantum Dots.* Phys. Rev. Lett. **95**, 166603 (2005).

[132] O. Olendski and T. V. Shahbazyan. *Theory of anisotropic spin relaxation in quantum dots.* Phys. Rev. B **75**, 041306 (2007).

[133] A. C. Clark, K. K. Schwarzwälder, T. Bandi, D. Maradan, and D. M. Zumbühl. *Method for cooling nanostructures to microkelvin temperatures.* Review of Scientific Instruments **81**, 103904 (2010).

[134] D. Maradan, L. Casparis, T.-M. Liu, D. E. F. Biesinger, C. P. Scheller, D. M. Zumbühl, J. Zimmerman, and A. C. Gossard. *GaAs Quantum Dot Thermometry Using Direct Transport and Charge Sensing.* Review of Scientific Instruments (2013).

[135] D. J. Griffiths. *Introduction to Electrodynamics* (Pearson, 2012).

[136] E. Rebhan. *Theoretische Physik* (Springer Verlag, 2008).

[137] G. Dresselhaus. *Spin-Orbit Coupling Effects in Zinc Blende Structures.* Phys. Rev. **100**, 580 (1955).

[138] F. G. Pikus and G. E. Pikus. *Conduction-band spin splitting and negative magnetoresistance in A_3B_5 heterostructures.* Phys. Rev. B **51**, 16928 (1995).

[139] Y. A. Bychkov and E. I. Rashba. *Oscillatory effects and the magnetic susceptibility of carriers in inversion layers.* Journal of Physics C: Solid State Physics **17**, 6039 (1984).

[140] A. G. Baca and C. I. H. Ashby. *Fabrication of GaAs Devices* (2005).

[141] M. Stopa. *Quantum dot self-consistent electronic structure and the Coulomb blockade.* Phys. Rev. B **54**, 13767 (1996).

List of Figures

2.1. Heterostructure 8
2.2. SEM picture of the device 9
2.3. Energy scales of a quantum dot 14
2.4. Transport Measurement Setup 16
2.5. Coulomb Oscillations - schematic 17
2.6. Coulomb Oscillations - measurement 18
2.7. Coulomb Diamonds - schematic 19
2.8. Coulomb Diamonds - measurement 20
2.9. Zeeman splitting - schematic 22
2.10. Zeeman splitting - pulsing 23
2.11. Double Quantum dot - schematic 25
2.12. Charge stability diagram - schematic 27
2.13. Charge stability diagram - schematic II 29
2.14. Charge stability diagram - transport data 30
2.15. Charge stability diagram - charge sensing data 30

3.1. QPC - schematic 34
3.2. QPC - charge sensing data 35
3.3. QD charge sensing - schematic 36
3.4. QD charge sensing - data 38
3.5. QD charge sensing - data2 38
3.6. Real-time setup 40
3.7. Real-time Data - Example 41
3.8. Noise Spectrum 43

4.1. Real-Time Tunneling - data 53
4.2. Tunneling - Histograms and Pon distribution 54
4.3. Tunneling - Evaluation Algorithm 58

4.4. Noise Generator . . . 60
4.5. Dot - feed back mechanism . . . 63
4.6. Sensor - feed back mechanism . . . 65
4.7. Load Intervals - Data . . . 68
4.8. Zeeman Splitting - Data . . . 69
4.9. Zeeman Visibility - Data . . . 70
4.10. g-factor - Data . . . 71

5.1. Device and Charge-Stability-Diagram . . . 75
5.2. Metastable Charge State Switching . . . 76
5.3. Real-Time Data and Temperature Dependence . . . 78
5.4. Four-Level System and Histograms . . . 79
5.5. Extension of the Orthodox Model . . . 81

6.1. Noise Diamond - Influence of Coupling to Source and Drain . . . 84
6.2. Noise Diamond at different Transitions Simultaneously . . . 87
6.3. Noise Diamond at (1,1) to (0,2) transition . . . 88
6.4. Noise Diamond - Temperature Dependence . . . 89
6.5. Noise Diamond - Bias Dependence . . . 91
6.6. Noise Diamond - Bias Dependence II . . . 93

7.1. Spine-Orbit Interaction - Schematic . . . 100
7.2. Spine Relaxation Time Measurement - Schematic . . . 102
7.3. Spine Relaxation Time Measurement - Data I . . . 104
7.4. Spine Relaxation Time Measurement - Data II . . . 106
7.5. Spine Relaxation Time Measurement - Data III . . . 107

A.1. Mesa and ohmic contacts . . . 115
A.2. Depletion Gates and SEM pictograph . . . 118
A.3. Bonded Sample . . . 118

B.1. Background Subtraction Tool . . . 121
B.2. Feedback Mechanism - Coupling Constants . . . 123
B.3. Charge Sensor - Feedback Mechanism . . . 124
B.4. CB Diamonds - Charge Sensing . . . 126
B.5. Pulse Box - Schematics . . . 127
B.6. Electrostatic Simulations . . . 129

Acknowledgment

I would like to thank Prof. Dr. Dominik Zumbühl for giving me the opportunity to do research in his group. The accumulation of physical knowledge and technical know-how in his group were of great benefit for me during my time as a PhD student.

This work was only possible due to the collaboration with other group members and external scientist. I would like to thank Christian Scheller for a very close collaboration. Together we wrote numerous software tolls, analyzed huge amounts of real-time data and struggled to understand the *noise diamond*, which turned out to be an intrinsic effect in double quantum dots. I also would like to thank Prof. Dr. Bernd Braunecker for the collaboration on the effect of metastable charge state switching. Without his expertise in theoretical physics and his great ideas, which led to a model describing our observations, this work would not have been possible.

With Florian Dettwiler, Lucas Casparis and Dario Maradan I had plenty of helpful and interesting discussion about physics as well as technical issues of our experiments - thank you very much! Additionally, I would like to thank all current and former members of the Zumbühl group, Dorothee Hug, Myrsini Lafkioti, Pirmin Weigele, Mario Palma, Oliver Bärenbold, Larissa Conrad, Tai-Min Liu, Dominikus Kölbl, Mirko Rehmann, Serge Wächter, Simon Zihlmann, Leon Camenzind, Kai Schwarzwälder, Martin Brühlmann, Charulata Barge, Tony Clark and Sarah Heizmann for the very pleasant and friendly working atmosphere.

The Physics Department of the University of Basel is operating an electronics workshop as well as a mechanics workshop. Without the support and outstanding work done there, many experiments would be impossible. Consequently, I would like to thank Michael Steinacher, Werner Erni, Sheeba Madathilparambil and Sascha Linder from the electronics workshop. Further, I am very thankful for the support of Patrick Stöcklin, Dominik Sifrig, Sascha Martin and Nicolas Stöckli form the mechanics workshop.

I am also very grateful for the help of Barbara Kammermann and Astrid Kalt, whose work as secretaries is essential for the functionality of the department. Their help in

administrative problems was always a great relief.

Finally, I would like to thank my family for supporting me throughout all those years and encouraging me during periods of frustration.

Curriculum Vitae and Publications

Daniel Erich Fridolin Biesinger

1995 - 2004	Zweites Städtisches Gymnasium, Rottenburg am Neckar
2004 - 2010	Studies at the Eberhard-Karls Universität Tübingen
Jan. 2010	Diploma in physics
2010 - 2014	PhD at University of Basel

I owe my education to the following lecturers:

M. Weitz, T. Gutsche, S. Teufel, A. Fässler, J. Jochum, H. Müther, N Schopohl, H. Clement, D. Kölle, R Kleiner, C. Zimmerman, E. Plies, D. A. Wharam, D. M. Zumbühl

Publications

Daniel E. F. Biesinger, Christian P. Scheller, Bernd Braunecker, J. Zimmerman, A.C. Gossard, and Dominik M. Zumbühl, *Thermally Activated Charge Fluctuations in a Few Electron GaAs Double Quantum Dot.* In preparation for publication.

D. Maradan, L. Casparis, T.-M. Liu, D. E. F. Biesinger, C. P. Scheller, D. M. Zumbühl, J. Zimmerman, and A. C. Gossard, *GaAs Quantum Dot Thermometry Using Direct Transport and Charge Sensing*, Journal of Low Temperature Physics **175**, 784 (April 2014)